ISBN 978-82-326-4598-5 (printed ver.)
ISBN 978-82-326-4599-2 (electronic ver.)
ISSN 1503-8181

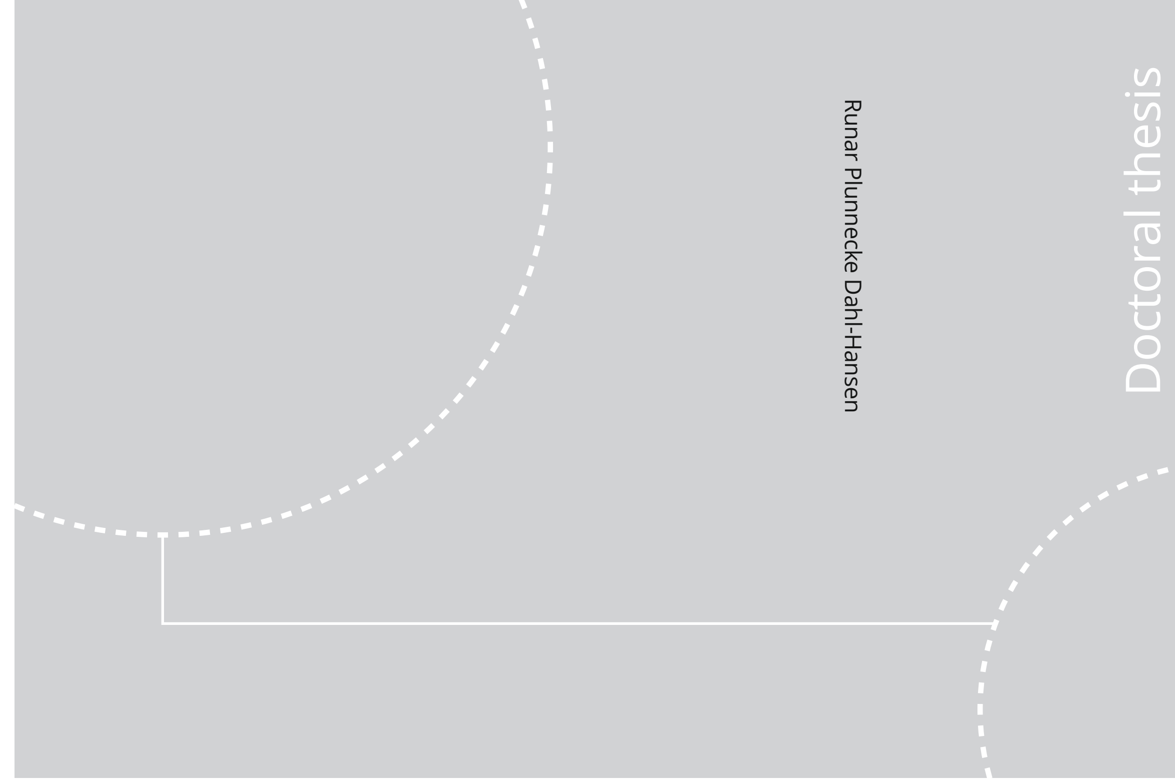

Doctoral theses at NTNU, 2020:125

NTNU
Norwegian University of Science and Technology
Thesis for the Degree of
Philosophiae Doctor
Faculty of Information Technology and Electrical
Engineering
Department of Electronic Systems

Doctoral theses at NTNU, 2020:125

Runar Plunnecke Dahl-Hansen

Reliability of Piezoelectric Microelectromechanical Systems in Humid Conditions

Runar Plunnecke Dahl-Hansen

Reliability of Piezoelectric Microelectromechanical Systems in Humid Conditions

Thesis for the Degree of Philosophiae Doctor

Trondheim, April 2020

Norwegian University of Science and Technology
Faculty of Information Technology and Electrical Engineering
Department of Electronic Systems

Norwegian University of
Science and Technology

NTNU
Norwegian University of Science and Technology

Thesis for the Degree of Philosophiae Doctor

Faculty of Information Technology and Electrical Engineering
Department of Electronic Systems

© Runar Plunnecke Dahl-Hansen

ISBN 978-82-326-4598-5 (printed ver.
ISBN 978-82-326-4599-2 (electronic ver.
ISSN 1503-8181

Doctoral theses at NTNU, 2020:125

Printed by NTNU Grafisk senter

Summary

Since its discovery, silicon-based microelectromechanical systems (MEMS) have had a significant impact on the technological development of sensors and actuators. Using piezoelectric materials deposited as thin-films on a substrate has enabled the mass production of miniaturized devices with high sensitivity and low power consumption. Piezoelectric MEMS (piezoMEMS), therefore, holds the promise of revolutionizing the sensor and actuator technology and is anticipated to dominate the future MEMS market.

Ferroelectric thin-films have high dielectric and piezoelectric compliances, which makes them attractive for piezoMEMS. Lead zirconate titanate (PZT) is an essential ferroelectric material for numerous thin-film piezoMEMS applications. Including inkjet-printers, ultrasound transducers, energy harvesters, autofocus lenses, gas-detectors, and ferroelectric random-access memories.

A key technological and scientific challenge for sustaining the development of thin-film piezoMEMS is improving their reliability and lifetime in realistic and harsh operating conditions. Elevated temperatures, high humidity levels, mechanical shocks, and stresses are all lifetime-limiting stressors that devices must endure in real-life, not encountered in a lab-scale environment. For the widespread adaption of thin-film piezoMEMS in sensor and actuator technology, it is necessary to mitigate the impact of such stressors. Understanding which physical and chemical degradation mechanisms imposed by the operating ambient affects device performance is, therefore, essential on both a microscopic and macroscopic scale.

The ambient humidity has proved to be one stress-factor that severely degrades the lifetime and reliability of piezoMEMS. However, humidity-related effects are complex and diverse, and different degradation-mechanisms can dominate, depending on the type of piezoMEMS-device. The goal of this thesis is to establish the critical stress-factors governing humidity-related degradation of thin-film, PZT-based piezoMEMS structures, and devices. Both test-structures and factual piezoMEMS devices were studied to bridge the gap between applied and fundamental research on reliability. Four manuscripts the main findings of this work.

A thin-film piezoelectric micro-mirror developed at SINTEF MiNaLab was chosen as a model thin-film piezoMEMS device for studying the effects of humidity from a device perspective. $\mathrm{LaNiO_3}$/Pt/Ti/$\mathrm{SiO_2}$ deposited on Si-substrates was chosen as a template functional stack for depositing 1 or 2 µm PZT thin-films by either pulsed laser deposition (PLD) or chemical solution deposition (CSD). Two PZT-compositions were studied; undoped $\mathrm{PbZr_{0.52}Ti_{0.48}O_3}$ and Ba-doped "hard" $\mathrm{Pb_{1-x}Ba_xZr_{0.40}Ti_{0.60}O_3}$. The electrodes, deposited by magnetron-sputtering, was varied depending on the type of study being conducted. Based on initial test-results from temperature-humidity-bias tests of micro-mirrors, simple test-structures, including pads, cantilevers, and diaphragms, were designed and fabricated to study the various aspects related to humidity-induced degradation in detail. Thin-film deposition and structuring were done in the cleanroom facilities at SINTEF MiNaLab and Penn State University's. Characterization of the reliability and lifetime of devices and test-structures were done in close collaboration with the Trolier-McKinstry group at Penn State University and SINTEF Industry.

Optical, scanning electron microscopy, atomic force microscopy and X-ray diffraction were used for microstructural characterization.

Various test set-ups, dedicated for studying the reliability and lifetime of piezoMEMS devices and test-structures, were developed to address the effects of humidity. The template set-up was specifically designed to be retrofittable to the different characterization-equipment available at the relevant lab-facilities. This set-up had a Raspberry Pi based platform for controlling the ambient humidity and temperatures, and consisted of a compact, 3D-printable environmental-chamber with viewports for studying the samples *in-situ* during the experiments. A high-temperature polyimide test-circuit with an integrated substrate heater was designed, making it possible to conduct electromechanical, ferroelectric, dielectric, leakage, and time-dependent measurements, simultaneously on multiple samples under controlled operating conditions.

As a first test case, temperature-humidity-bias tests were conducted on micro-mirrors with 1 µm $Pb_{0.9}Ba_{0.1}Zr_{0.40}Ti_{0.60}O_3$ deposited by PLD. 250 nm Au and a 10 nm Ti with 10 wt. % W adhesion-layer to PZT was used as the top electrode system. Unipolar actuation of 20 V_{PP} offset around 10 V_{DC}, corresponding to the device's maximum intended operating voltage, were carried out at substrate-temperatures from 25 to $175^{o}C$. The ambient humidity was kept constant at 22 g/m^3, corresponding to 95 % relative humidity (RH) at 25 ^{o}C. Initial characterization of the pristine devices showed characteristics, consistent with general ferroelectric theory. During the time-dependent measurements, however, device failure from water-induced degradation preceded that of time-dependent dielectric breakdown at all temperatures. In general, such degradation was manifested as local evaporation of the stack-material, forming craters along the edges and on the surface of the used electrodes. Increasing the temperature decreased the number of craters and increased the median time-to-failure, which correlated well with the Brunauer-Emmet Teller theory for water-adsorption on gold-surfaces. Consequently, humidity-degradation was significantly more aggressive at room-temperature than at elevated temperatures. Despite this, humidity-induced device-failure was encountered also at elevated, even as the ambient approached 15 % RH. In comparison, no device-failure within the experimental timeframe was detected at 25°C and 35 % RH. Based on the findings, it was proposed that humidity-induced degradation stems from the electrolysis of water.

To study the coupling between water-electrolysis and degradation, a comparative study of Pt and Au-based circular top electrode-pads with a diameter of 400 µm on top of 2 µm undoped $PbZr_{0.52}Ti_{0.48}O_3$ thin-films deposited by CSD, was conducted. It was shown that humidity-related degradation couples directly to the stack's electrochemical activity towards the electrolysis of water. As a result of the evolved hydrogen and oxygen gas at the top and bottom electrodes, electrochemical compression lead to cracking and delamination of the piezoelectric layer and top electrodes. Consequently, electrothermal breakdown-events occurring through the newly formed cracks, resulted in time-dependent breakdown, significantly sooner in humid compared to dry conditions. Exemplified for 40 V_{DC}, the median time-to-failure for Au was here three orders of magnitude of time larger than for Pt, at room-temperature in 95 % RH. The results were not consistent with a degradation of the electrical properties of the electrode/PZT interface properties, as commonly encountered in dry conditions. Furthermore, the post-failure craters were considerably larger in humid than in dry conditions, suggesting that additional contributions to leakage, presumably from protonic currents, are involved during breakdown. Based on the findings, a degradation-model for thin-film piezoMEMS in humid conditions degradation was proposed.

By studying how surface-currents and the electrode size affected humidity-induced degradation, it was shown that the presence of surface-water is essential for degradation. When the operating ambient exceeds about 50 % relative humidity, protonic surface currents from the anode to the cathode dominate the measured leakage and drives degradation. Since irreversible degradation, including microcracking and electrode-delamination, cannot be removed by drying up the surface, the

pristine state of humidity-degraded devices can only be partly recovered by flushing with dry N_2 or post-degradation annealing. Increasing the radius of the electrode from 50 to 1000 µm decreased the median time-to-failure by two orders of magnitude, presumably due to the increase in the exposed electrochemically active areas. Accordingly, the median time-to-failure displayed an electrode area-dependence rather than a circumference-dependence.

Lastly, the use of atomic-layer deposited Al_2O_3 humidity barrier-layers for improving device reliability, was studied. The dynamic behavior and lifetime of bare and encapsulated micro-mirrors with the initial stack of 1 µm $Pb_{0.9}Ba_{0.1}Zr_{0.40}Ti_{0.60}O_3$ deposited by PLD, were studied. A two orders of magnitude of time increase in the median time-to-failure, in 95 % relative humidity was demonstrated, yet at the cost of decreased piezoelectric and ferroelectric properties, presumably related to the additional encapsulation-step. The encapsulated devices failed by the same mechanisms as for the bare devices due to breaches in the barrier-layer at localized points of the device. The breaches were found to stem from a combination of defects in the barrier-layer, cracks in the PZT-film induced from wire-bonding or sputtered particles from processing, and electrode-delamination. Electrothermal breakdown-events on the membrane decreased the reliability due to distortions in the dynamical behavior of the micro-mirrors during operations, and the electrode-routings were identified as critical flaws.

From the above findings, some mitigation-strategies for reducing the impact of humidity, are proposed:

(i) Decreasing the overall electrochemical activity of the stack will reduce the amount of water-electrolysis, and thereby the degradation-rate.

(ii) Since, within the framework of water-electrolysis, protons generated on the anode-side move towards the cathode-side of the stack, the bottom electrode should be chosen as the positrode. This, to reduce the area of the electrochemically active materials being exposed to the ambient during operation, thereby reducing the proton-transport through the piezoelectric layer.

(iii) The electrochemical activity can be reduced by impeding the proton mobility in PZT and along exposed surfaces, e.g. by reducing the physisorption of water-molecules on the exposed surfaces.

(iv) Reducing the number of electrode-defects, such as grain-grooves, sputtered particles, cracks or pinholes will reduce the diffusion of protons and hydrogen through the electrode. This can be done by e.g. increasing the electrode thickness when possible.

(v) Since the electrolysis of water is essentially a DC-phenomena involving the transport of protons in the form of hydronium or hydroxide-ions, the electrochemical activity will further be reduced by using high-frequency (>100 Hz) bipolar actuation, when such operation is relevant (e.g. for FRAM-applications).

(vi) It is imperative to encapsulate piezoMEMS-devices. Therefore, improved electromechanical durability, improved coverage over complex structured surfaces, and reduced water-vapor transmission rate of the humidity barrier-layer will reduce the impact of water. Multi-layered coatings deposited by atomic layer deposition show promising results in this regard.

Preface

This dissertation is submitted in partial fulfillment of the requirements for the degree of Philosophiae Doctor (Ph.D.) at the Norwegian University of Science and Technology (NTNU). One semester of the Ph.D. was carried out in the Susan Trolier-McKinstry group at Penn State University under Susan Trolier-McKinstry as a host supervisor. The main part of this work was carried out at SINTEF MiNaLab with Prof. Thomas Tybell and Sr. Researcher Frode Tyholdt as thesis supervisors.

Acknowledgements

The three years of my Ph.D. has been filled with good memories, exciting experiences, frustration and personal development, both on a scientific and personal level. I have gotten to know many brilliant people and I wish to express my sincere gratitude to all those who have made these years possible. It has been a tough but exciting journey with many challenging and interesting scientific and social experiences which has made me grow on many levels. I am very grateful for that I have been given this opportunity and I look forward to many more exciting years to come. And, of course, I am happy that it's is finally over[1]!

First, I would like to thank my main supervisors, Thomas Tybell and Frode Tyholdt who have been incredibly patient and helpful during my times of struggling with experiments, manuscripts and trying to understand what the hell I am doing and what is going on. They are among the rare people who displays consistency and excellency on both a professional and personal level. I am grateful both for our scientific discussions as well as the outside-of-work get-togethers we have had over these years. I look forward to future years of collaboration!

The work in this thesis would not have been possible without the help and support of the guys at SINTEF MiNaLab, from everything piezoMEMS-related to cheer-ups and social activities. Of these I would like to acknowledge Hallvard Angelskår for helping me with MATLAB and engineering-related issues, Jo Gjessing for sharing all his know-how with LabView and showing me the ways of the optics lab, Christopher Andrew Dirdal for the good scientific discussion, help with mathematical derivations and squash-sessions, Lars-Geir Whidst-Tvedt for helping me with designing and fabricating test structures, Andreas Vogl for his valuable inputs on micromechanics (and social-skills) and Jon Vedum for help and advice on experimental setups and circuit design. I would like to give a special thanks to Paul Wittendorp without whom most of this work would not have been possible. Thanks for assisting and teaching me the equipment in the lab, for helping me with the many critical steps necessary to navigate the confusing jungle of fabricating piezoMEMS, for all the squash-sessions, morning-coffees and social activities! Also, I could not have been without the help of several people from the Thin-film and Membrane-Science group in the department of Sustainable Energy Technology at SINTEF. Thanks to Yngve Larring, Jonathan Polfus and Einar Vøllestad for valuable and interesting scientific discussions on surface-protonics, electrolysis, and ionics and to Marit Stange for help with SEM and thin-film depositions.

Much of my personal development and scientific progress was gained during my stay in the Susan Trolier-McKinstry group at Penn State University, Pennsylvania, USA. I would like to give a special

[1] …to be correctly misunderstood…

thanks to my host supervisor Susan Trolier-McKinstry for accepting me into the group and sharing her valuable knowledge and advice during my stay. She is truly a legend within the field of piezoMEMS, and I am privileged to have gotten to meet and collaborate with her and her group. Many people have assisted me during my stay at Penn State in which I am also very grateful. I wish to give a special thanks to Kathleen Coleman, Wanlin Zhu, Betul Akkopru-Akgun, Lyndsey Denis and Jeff Long from whom I gained much valuable scientific help and advice.

The support from my wife, Line Magnussen, have also been very important for me to get through my Ph.D. Within my work she has helped me with listening to and shaping presentations, reviewing and significantly improving my terrible writing and first-draft manuscripts, structure my work, broadening my perspectives and guiding/motivating me when things are tough. I highly value her ability to pull me out of work to climbing, hiking, do gymnastics or simply going downtown to enjoy some good food or a nice cup of coffee. My sanity, motivation and quality at work would not have been the same without you!

I would also like to thank my collaborators in the Oxide Electronics Group at IES in Trondheim: Kristoffer Kjærnes, Torstein Bolstad, Magnus Moreau, Ambjørn Dahle Bang, Fredrik Kjemperud Olsen, Einar Digernes, Sam Slöetjes, Ingrid Hallsteinsen, Anders Strømberg, Erik Folven and Jostein Grepstad. I am proud to be allowed to wear the groups emblem in the form of a bowtie every time I'm out to defend the honour of this extraordinary group.

Lastly, I would thank my close friends and family for their advice, interest in my work and playtime outside of work. It is important for someone like me to be reminded that no matter how determined you are to make something happen, it is wise to stop and think once in a while. There is a life outside of science and work after all.

Runar Plünnecke Dahl-Hansen
SINTEF MiNaLab, Oslo, Norway
November 2019

Contents

Summary ... i
Preface ... v
Acknowledgements ... v
Contents ... vii
1 Introduction ... 1
References ... 5
2 PZT in thin-film piezoMEMS-devices ... 7
2.1 Piezoelectrics and ferroelectrics ... 7
2.1.1 What is piezoelectricity? ... 7
2.1.2 Piezoelectric response in thin-films ... 8
2.1.3 Ferroelectric perovskites ... 9
2.1.4 Ferroelectric switching ... 11
2.1.5 Contributions to the piezoelectric response ... 11
2.1.6 Film thickness and microstructure ... 12
2.2 Lead zirconate titanate ... 13
2.2.1 Structure-property relations ... 13
2.2.2 Defect structure ... 14
2.3 Integrating PZT thin-films in piezoMEMS ... 15
2.3.1 Properties of the PZT-electrode system ... 15
(i) Rectifying contact ... 15
(ii) Chemical compatibility ... 16
(iii) Microstructure ... 16
(iv) Adhesion ... 16
(v) Polarization fatigue ... 16
(vi) Electrode interface ... 17
2.3.2 Mechanical stresses in thin-films ... 17
2.4 Advances in piezoMEMS reliability ... 18
2.4.1 Ambient humidity ... 18
2.4.2 Mechanical limitations ... 19
2.4.4 DC electrical field reliability ... 21

2.4.5 Aging and polarization fatigue ... 22
2.5 Summary ... 23
References ... 25
3 Design, fabrication and characterization of piezoMEMS ... 31
3.1 PiezoMEMS structures and devices ... 31
3.1.1 Fabrication of thin-film piezoMEMS ... 31
(i) Oxidation ... 31
(ii) Film deposition ... 32
(iii) Patterning ... 32
(iv) Backside etching and dicing ... 32
3.1.2 Micromirror geometry ... 33
3.2 Experimental setup and test-structure design ... 33
3.2.1 Experimental setup ... 34
3.2.2 Design of PZT-based test-structures ... 35
3.3 Thin-film and device characterization ... 36
3.3.1 Texture and microstructure ... 36
3.3.2 Polarization, permittivity and dielectric loss ... 37
3.3.3 Piezoelectric properties ... 38
3.3.4 Residual film stress ... 39
3.3.5 Electromechanical response ... 40
3.3.6 Electrode interfaces ... 40
3.3.7 Lifetime measurements ... 41
(i) Statistical analysis ... 42
(ii) Voltage acceleration ... 42
(iii) Humidity-acceleration ... 43
References ... 45
4 Author's contribution ... 49
(I) Performance and reliability of PZT-based piezoelectric micro-mirrors operated in realistic environments ... 51
(II) Electrochemically Driven Degradation of Ferroelectric Thin-Films in Humid Ambient ... 57
(III) Links between resistance-degradation and recovery of PZT operated in humid conditions ... 93
(IV) On the effects of water-induced degradation on thin-film piezoelectric microelectromechanical systems ... 117
5 Conclusions and outlook ... 145
5.1 Conclusions ... 145
5.2 Outlook and future work ... 147

Chapter 1

Introduction

Sensors and actuators are devices that enable embedded electronics to interact with their physical surroundings. While a sensor converts a physical input, such as light, pressure, motion, or heat, to an electrical signal, an actuator converts an electrical signal some physical output[1]. Today sensor -and actuator applications span from mass-produced consumer-electronics to custom-made electronic equipment.

Microelectromechanical systems (MEMS) can convert mechanical energy to electrical energy and vice versa. This is known as electromechanical transduction and is essential for enabling sensor and actuator technologies. Since its invention in the mid-1970s MEMS-technology has demonstrated tremendous success, and currently represents a $55 B market with an estimated growth of more than 8 % over the next five years[2]. Essential for the success of MEMS-technology is its compatibility with existing CMOS-materials and fabrication technologies. This allows for both monolithic and heterogeneous integration of a wide variety of mechanical and electrical devices on a single silicon substrate. The compatibility with mature manufacturing technologies has spurred a rapid increase in research and development and production volume. Over the years, this has resulted in MEMS-based devices becoming ever cheaper, smaller, more responsive, and energy-efficient. Today, MEMS-technology appear in applications ranging from pressure sensors, microphones, optical devices, energy harvesters, radiofrequency switches, gyroscopes, accelerometers, inkjet printers, resonators, and ultrasound devices[3].

Electromechanical transduction mechanisms used for MEMS include piezoelectric, electrostatic[4–7], and thermal[8,9]. The piezoelectric effect has attributes that surpass the other transduction mechanisms with regards to scalability, low power consumption, high blocking pressures, and high electromechanical coupling over a wide range of temperatures and frequencies. Piezoelectricity, meaning "electricity from pressure", is derived from the Greek words "piezein", that is translated to squeeze or press, and "electron" which means amber – an ancient source of electrical charge. When mechanically stressed, piezoelectric materials develop an electric potential across the crystal, through what is known as the direct piezoelectric effect. Conversely, piezoelectric materials develop a mechanical strain when an electric field is applied. This is known as the converse piezoelectric effect. The direct and converse effects thus allow for electromechanical transduction in piezoelectric materials. While the direct effect is used for sensors-applications, the converse effect is used for actuator-applications. As opposed to conventional transistor-based technology, piezoelectric MEMS (piezoMEMS) technology is not subject to significant limitations in critical dimensions and is, therefore, considered an integral part of the so-called "More than Moore" technologies. In fact, as illustrated in Figure 1.1., business companies, such as Yole Development, anticipates that piezoMEMS technology will revolutionize the MEMS-industry with its continued expansion into both existing and novel application-areas[10].

The use of thin-films deposited onto a silicon substrate, offers an efficient route for making miniaturized, cheap, and precise piezoMEMS devices. After "sandwiching" the piezoelectric layer

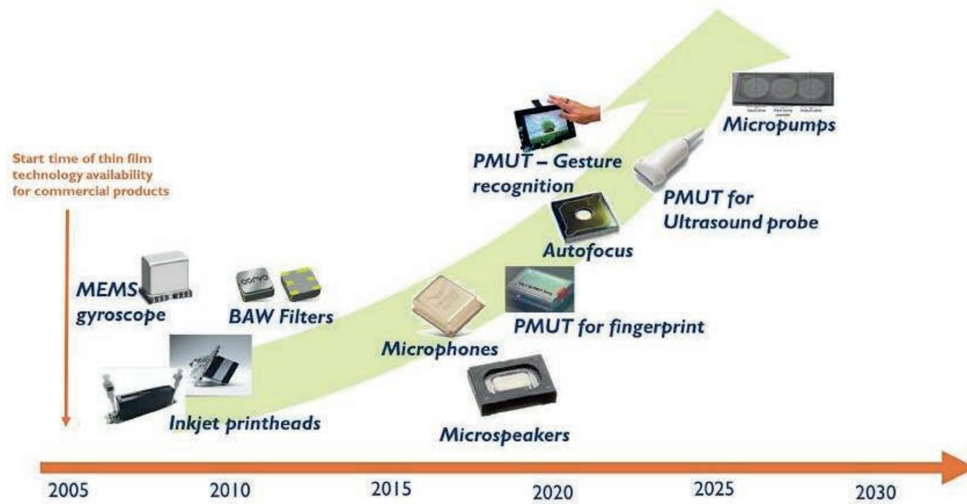

Figure 1.1*:* Using thin-film technology enables a significant growth for piezoMEMS-devices and holds the promise of revolutionizing the MEMS-technology. Copied from [10].

between two electrodes, the functional stack is patterned into the final MEMS structure. In this way, thousands of reliable, low-power, and low-cost devices can be fabricated simultaneously on a single silicon wafer[11,12]. Lead zirconate titanate (PZT), is a piezoelectric material with particularly large dielectric and piezoelectric compliances and is, therefore, technologically important for piezoMEMS-applications[13–15]. Currently, PZT thin-films are already being adopted in a large variety of piezoMEMS-applications, including ink-jet printers[16], energy harvesters[17–21], ultrasound transducers[12,22–25], optical devices[26–32] and micromotors[33,34]. Maintaining this technological development necessitates a continued improvement in the reliability and lifetime of piezoMEMS-devices. As their application-areas keeps on expanding, piezoMEMS-devices must sustain reliable long-term operation in realistic and harsh conditions. In real-life applications, devices are subjected to additional stress-factors imposed by the operating ambient, which are not encountered in a lab-scale environment. This includes high ambient humidity[35–37], elevated temperatures[38,39] and applied mechanical shocks or stresses[40–42]. If these stress-factors are not considered, it can significantly limit the reliability, lifetime and potential applications of thin-film PZT-based piezoMEMS-devices. Of the various ambient stressors, the impact of several essential lifetime-limiting factors, such as high electrical fields, high operating frequencies, and elevated temperatures, have been thoroughly investigated and are well understood[43,44]. These stressors are commonly used for assessing device reliability and extrapolate device lifetimes from accelerated testing[45–48]. The understanding of the effects of mechanical stresses on piezoMEMS-devices has recently received considerable attention, in order to improve the mechanical limitations of piezoMEMS[49–54]. Degradation and failure encountered when devices are operated in humid conditions, on the other hand, lack understanding[45,49,55]. This is, despite that humidity is considered among the most severe ambient stress factors and has been shown to cause device failure decades earlier than in dry conditions[56–61].

Norwegian companies, including Tunable[57], Polewall[24], and PoLight[58], develop and fabricate PZT-based sensors and actuators for applications within gas detection, communication-technology and optics. To expand their application into new markets, an essential objective is to establish the critical factors governing degradation of PZT-based thin-film piezoMEMS in humid conditions. This thesis is a collaboration between NTNU, SINTEF, and the Norwegian industry to gain a rigorous understanding of the degradation imposed by the ambient humidity.

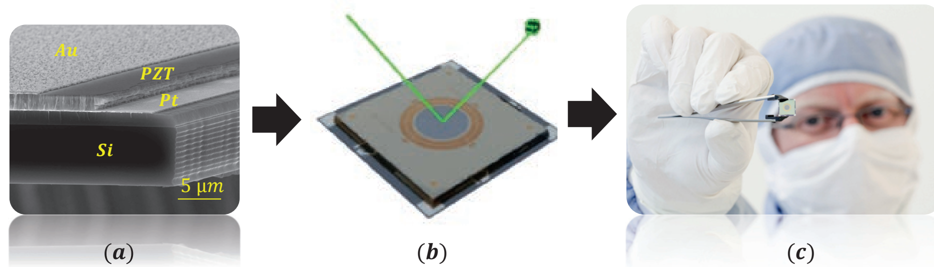

Figure 1.2: Example of a piezoMEMS device developed by Tunable. The functional stack generally consists of a piezoelectric layer sandwiched between two electrodes as illustrated in (a). The thin-films are from 10 nm to 2 µm in thickness and deposited on a structured silicon substrate. Illustrated device in (b)-(c) is an 8x8 mm^2 micromirror which has applications within optical communication and gas detection. Adapted from [62].

Figure 1.2 shows a PZT-based microdevice, a thin-film piezoelectric micro-mirror developed by Tunable, which is chosen as a model device for studying humidity-related effects on piezoMEMS. To simulate real-life operation, dedicated test-setups for conducting experiments under controlled ambient conditions were developed. To elaborate on humidity-related mechanisms, piezoelectric test-structures were designed, and these were used to study the resistive, dielectric, piezoelectric, and ferroelectric properties in dry, humid, and wet conditions. Finally, micro-mirrors encapsulated with humidity barrier-layers, were used to examine the effect of degradation on the dynamical behavior of devices and explore the feasibility of using thin-film encapsulation to mitigate humidity-related effects.

The thesis is structured as follows: Chapter 2 presents the fundamentals of piezoelectricity, with a special reference to polar materials that are both piezoelectric and ferroelectric. The structure-property relations of PZT, concerning physical and chemical properties that affect film performance and integration into piezoMEMS devices, are discussed. Recent progress within the reliability and lifetime of thin-film piezoMEMS-devices, is then presented. Chapter 3 presents the experimental methods used in this thesis. General aspects related to the fabrication of the micro-mirrors and test-structures, the development of the used experimental setups, and the characterization techniques used in this study, are discussed. The results and findings are presented in four manuscripts: In manuscript (I), the effects of humidity and temperature on the degradation of piezoelectric micro-mirrors are studied. In manuscript (II)-(III), the mechanisms driving degradation in humid conditions are investigated in detail. In manuscript (IV), the impact of degradation on the dynamic behavior of piezoelectric micromirrors and how the use of thin-film encapsulation can mitigate humidity-related degradation, are investigated. The thesis ends with general conclusions and perspectives for future work within the reliability of thin-film piezoMEMS.

References

[1] T. L. Friedman, *Thank you for being late: An optimists guide to thriving in the age of acceleration*; 2016.

[2] M. K. Mishra, V. Dubey, P. M. Mishra, I. Khan, *J. Eng. Res. Reports* **2019**, *4*, 1.

[3] R. Bogue, Recent developments in MEMS sensors: A review of applications, markets and technologies. *Sens. Rev.* **2013**, *33*, 300–304.

[4] W. Noell, T. Overstolz, R. Stanley, N. F. de Rooij, In *MEMS, MOEMS, and Micromachining II*; Ürey, H.; El-Fatatry, A., Eds.; International Society for Optics and Photonics, 2006; Vol. 6186, p. 61860H.

[5] V. Milanović, G. A. Matus, D. T. McCormick, *IEEE J. Sel. Top. Quantum Electron.* **2004**, *10*, 462.

[6] I. W. Jung, U. Krishnamoorthy, O. Solgaard, *J. Microelectromechanical Syst.* **2006**, *15*, 563.

[7] H. Ra, W. Piyawattanametha, Y. Taguchi, D. Lee, M. J. Mandella, O. Solgaard, *J. Microelectromechanical Syst.* **2007**, *16*, 969.

[8] S. T. Todd, A. Jain, H. Qu, H. Xie, *J. Opt. A Pure Appl. Opt.* **2006**, *8*, S352.

[9] K. Jia, S. Pal, H. Xie, *J. Microelectromechanical Syst.* **2009**, *18*, 1004.

[10] Yole Développement, **2019**.

[11] S. Tadigadapa, K. Mateti, *Meas. Sci. Technol.* **2009**, *20*, 1.

[12] Y. Qiu, J. V Gigliotti, M. Wallace, F. Griggio, C. E. M. Demore, S. Cochran, S. Trolier-McKinstry, Piezoelectric micromachined ultrasound transducer (PMUT) arrays for integrated sensing, actuation and imaging. *Sensors (Switzerland)* **2015**, *15*, 8020–8041.

[13] S. Trolier-McKinstry, S. Zhang, A. J. Bell, X. Tan, *Annu. Rev. Mater. Res.* **2018**, *48*, 191.

[14] P. Muralt, S. Trolier-McKinstry, *J. Electroceramics,* **2004**, *12*, 7.

[15] C.-B. Eom, S. Trolier-McKinstry, *MRS Bull.* **2012**, *37*, 1007.

[16] E. Fujii, R. Takayama, K. Nomura, A. Murata, T. Hirasawa, A. Tomozawa, S. Fujii, T. Kamada, H. Torii, In *IEEE International Symposium on Applications of Ferroelectrics*; 2007; Vol. 54, pp. 703–706.

[17] R. Caliò, U. B. Rongala, D. Camboni, M. Milazzo, C. Stefanini, G. de Petris, C. M. Oddo, Piezoelectric energy harvesting solutions. *Sensors (Switzerland)* **2014**, *14*, 4755–4790.

[18] M. D. Nguyen, E. Houwman, M. Dekkers, D. Schlom, G. Rijnders, *APL Mater.* **2017**, *5*, 0.

[19] H. Elahi, M. Eugeni, P. Gaudenzi, *Energies* **2018**, *11*, 1850.

[20] M. El-hami, P. Glynne-Jones, N. M. White, M. Hill, S. Beeby, E. James, A. D. Brown, J. N. Ross, *Sensors Actuators, A Phys.* **2001**, *92*, 335.

[21] Q. Shi, T. Wang, C. Lee, *Sci. Rep.* **2016**, *6*, 24946.

[22] H. S. Choi, J. L. Ding, A. Bandyopadhyay, M. J. Anderson, S. Bose, *J. Micromechanics Microengineering* **2008**, *18*, 025037.

[23] A. Feeney, L. Kang, G. Rowlands, L. Zhou, S. Dixon, *IEEE Sens. J.* **2019**, 1.

[24] Y. Kusano, Q. Wang, G. L. Luo, Y. Lu, R. Q. Rudy, R. G. Polcawich, D. A. Horsley, *J. Microelectromechanical Syst.* **2018**, *27*, 296.

[25] J. Munir, Q. Ain, H. J. Lee, Reliability issue related to dielectric charging in capacitive micromachined ultrasonic transducers: A review. *Microelectron. Reliab.* **2019**, *92*, 155–167.

[26] V. Cotroneo, W. N. Davis, P. B. Reid, D. A. Schwartz, S. Trolier-McKinstry, R. H. T. Wilke, In *Optics for EUV, X-Ray, and Gamma-Ray Astronomy V*; O'Dell, S. L.; Pareschi, G., Eds.; International Society for Optics and Photonics, 2011; Vol. 8147, p. 81471R.

[27] C. L. Hom, P. D. Dean, S. R. Winzer, In *Smart Structures and Materials 2000: Smart Structures and Integrated Systems*; Wereley, N. M., Ed.; International Society for Optics and Photonics, 2003; Vol. 3985, p. 394.

[28] R. A. Windhorst, R. A. Cameron, R. J. Brissenden, M. S. Elvis, G. Fabbiano, P. Gorenstein, P. B. Reid, D. A. Schwartz, M. W. Bautz, E. Figueroa-Feliciano, R. Petre, N. E. White, W. W. Zhang, Generation-X: An X-ray observatory designed to observe first light objects. *New Astron. Rev.* **2006**, *50*, 121–126.

[29] T. Bakke, A. Vogl, O. Zero, F. Tyholdt, I. R. Johansen, D. Wang, *J. Micromechanics*

Microengineering **2010**, *20*, 1.
[30] Polewall Home - Polewall.
[31] J. F. Ihlefeld, B. M. Foley, D. A. Scrymgeour, J. R. Michael, B. B. McKenzie, D. L. Medlin, M. Wallace, S. Trolier-Mckinstry, P. E. Hopkins, *Nano Lett.* **2015**, *15*, 1791.
[32] C. Dagdeviren, Y. Shi, P. Joe, R. Ghaffari, G. Balooch, K. Usgaonkar, O. Gur, P. L. Tran, J. R. Crosby, M. Meyer, Y. Su, R. C. Webb, A. S. Tedesco, M. J. Slepian, Y. Huang, J. A. Rogers, *Nat. Mater.* **2015**, *14*, 728.
[33] A. E. Islam, *IEEE Trans. Device Mater. Reliab.* **2016**, *16*, 647.
[34] G. Esteves, C. M. Fancher, M. Wallace, R. Johnson-Wilke, R. H. T. Wilke, S. Trolier-McKinstry, R. G. Polcawich, J. L. Jones, *Mater. Des.* **2016**, *111*, 429.
[35] R. P. Dahl-Hansen, T. Tybell, F. Tyholdt, In *2018 IEEE ISAF-FMA-AMF-AMEC-PFM Joint Conference, IFAAP 2018*; IEEE, 2018; pp. 1–4.
[36] J. Wang, C. Salm, E. Houwman, M. Nguyen, J. Schmitz, *Proc. 2016 IEEE Int. Integr. Reliab. Work. IIRW 2016* **2017**, *0*, 65.
[37] M. B. Starr, X. Wang, *Nano Energy* **2014**, *14*, 296.
[38] E. Vereshchagina, E. Poppe, K. Schjolberg-Henriksen, M. Wohrmann, S. Moe, In *2018 7th Electronic System-Integration Technology Conference, ESTC 2018 - Proceedings*; IEEE, 2018; pp. 1–9.
[39] B. Kaeswurm, F. H. Schader, K. G. Webber, *Ceram. Int.* **2018**, *44*, 2358.
[40] H. Nazeer, M. D. Nguyen, G. Rijnders, L. Abelmann, Sardan Sukas, *Microelectron. Eng.* **2016**, *161*, 56.
[41] F. H. Schader, M. Morozov, E. T. Wefring, T. Grande, K. G. Webber, *J. Appl. Phys.* **2015**, *117*.
[42] J.-W. Lee, C.-S. Park, M. Kim, H.-E. Kim, *J. Am. Ceram. Soc.* **2007**, *90*, 1077.
[43] P. Rafiee, G. Khatibi, M. Zehetbauer, *Microelectron. Int.* **2017**, *34*, 9.
[44] A. Arab, Q. Feng, *Int. J. Adv. Manuf. Technol.* **2014**, *74*, 1679.
[45] L. M. Garten, M. Hagiwara, S. W. Ko, S. Trolier-McKinstry, *Appl. Phys. Lett.* **2017**, *111*, 122903.
[46] S. W. Ko, W. Zhu, C. Fragkiadakis, T. Borman, K. Wang, P. Mardilovich, S. Trolier-McKinstry, *J. Am. Ceram. Soc.* **2019**, *102*, 1211.
[47] W. Zhu, B. Akkopru-Akgun, S. Trolier-McKinstry, *Appl. Phys. Lett.* **2017**, *111*.
[48] R. Q. Rudy, L. M. Sanchez, M. Tellers, R. G. Polcawich, In *2015 Transducers - 2015 18th International Conference on Solid-State Sensors, Actuators and Microsystems*; IEEE, 2015; pp. 1315–1317.
[49] K. Coleman, J. Walker, T. Beechem, S. Trolier-McKinstry, *J. Appl. Phys.* **2019**, *126*, 034101.
[50] M. Deluca, R. Bermejo, M. Pletz, M. Wießner, P. Supancic, R. Danzer, *J. Eur. Ceram. Soc.* **2012**, *32*, 4371.
[51] F. H. Schader, D. Isaia, M. Weber, E. Aulbach, K. G. Webber, *J. Mater. Sci.* **2018**, *53*, 3296.
[52] A. Ayrikyan, O. Prach, N. H. Khansur, S. Keller, S. Yasui, M. Itoh, O. Sakata, K. Durst, K. G. Webber, *Acta Mater.* **2018**, *148*, 432.
[53] M. Deluca, R. Bermejo, H. Grünbichler, V. Presser, R. Danzer, K. G. Nickel, *Scr. Mater.* **2010**, *63*, 343.
[54] K. Coleman, R. Bermejo, D. Leguillon, S. Trolier-McKinstry, *Acta Mater.* **2019**.
[55] D. Monteiro Diniz Reis, S. Rzepka, K. Hiller, *Microelectron. Reliab.* **2018**, *88–90*, 835.
[56] J. D. Baniecki, J. S. Cross, M. Tsukada, J. Watanabe, *Appl. Phys. Lett.* **2002**, *81*, 3837.
[57] Y. Saito, T. Nakamura, K. Nada, H. Sano, In *Japanese Journal of Applied Physics*; 2018; Vol. 57, p. 11UC04.
[58] L. W. Li, X. Sun, J. X. Li, L. J. Qiao, Y. J. Su, W. Y. Chu, *Appl. Surf. Sci.* **2009**, *255*, 7841.
[59] I. P. Lipscomb, P. M. Weaver, J. Swingler, J. W. McBride, *Sensors Actuators, A Phys.* **2009**, *151*, 179.
[60] P. Bintachitt, P. Suaprasert, P. Aungkavattana, *Integr. Ferroelectr.* **2016**, *175*, 44.
[61] D. Zheng, J. Swingler, P. Weaver, *Sensors Actuators A Phys.* **2010**, *158*, 106.

Chapter 2

PZT in thin-film piezoMEMS-devices

Lead zirconate titanate (PZT) is utilized for a variety of piezoMEMS-devices. This chapter reviews the concepts of piezoelectricity with a focus on polar materials and PZT. First, the general theory of piezoelectricity in thin-films is reviewed. Piezoelectricity in ferroelectric perovskite oxides with a specific reference to the structure-property relations of PZT is then presented. Factors concerning the integration of PZT thin-films into piezoMEMS are also discussed. Finally, an overview of the present status and challenges with regards to piezoMEMS reliability is presented.

2.1 Piezoelectrics and ferroelectrics

This section reviews the fundamentals of piezoelectricity with a specific reference to polar materials that are both ferroelectric and piezoelectric. The goal is to give the reader a basic understanding of the underlying mechanisms that enable piezoelectricity in materials with the perovskite structure. First, an introduction to the general principles of piezoelectricity is given. Then the constraints from the thin-film boundary-conditions on the piezoelectric response are discussed. Lastly, the general theory of ferroelectric perovskite oxides, important for piezoMEMS applications, is presented.

2.1.1 What is piezoelectricity?

Electromechanical transduction, the ability to convert between electrical and mechanical energy, is essential for any micromechanical system[1]. The piezoelectric effect is attractive for piezoMEMS-devices since it offers a reliable, robust, and scalable transduction method[2]. Piezoelectricity stems from the macroscopic effect of atomic and ionic displacement within the material and is manifested through the direct and converse piezoelectric effect. The direct effect describes the developed polarization when the material is mechanically stressed. The induced polarization, ΔP_i, couples linearly to the applied stress (σ_{jk}) and strain, (x_{jk}), and is expressed as:

$$\Delta P_i = d_{ijk}\sigma_{jk} \; \left[\frac{C}{m^2}\right] \quad (2.1)$$

$$\Delta P_i = e_{ijk}x_{ijk} \; \left[\frac{C}{m^2}\right] \quad (2.2)$$

Here $i, j, k = 1,2,3$ denotes the direction of the applied field and generated stress according to the Einstein notation. The piezoelectric charge-coefficient, d_{ijk}, with units of $\left[\frac{m}{V}\right]$, describes the induced charge in response to an applied stress. The piezoelectric stress-coefficient e_{ijk}, with units of $\left[\frac{C}{m^2}\right]$, describes the generated stress in response to an applied electric field.

The converse effect is the development of a mechanical strain in response to an applied electric field, E_k[3,4]:

$$\Delta x_{ij} = d_{ijk}E_k \quad (2.3)$$

$$\Delta\sigma_{ij} = -e_{ijk}E_k \; [Pa] \quad (2.4)$$

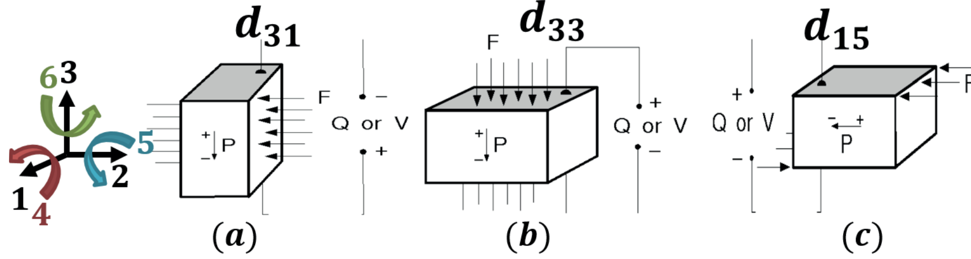

Figure 2.1: Relations between the applied forces and measured field for characterizing piezoelectric materials according to Einstein notation. d_{31} describes the in-plane, and d_{33} the out-of-plane deformation in response to an applied field perpendicular to the piezoelectric slab as shown in (a) and (b). d_{15} describes the generated shear-forces in response to an in-plane field, as shown in (c).

The amount of the input energy converted to mechanical energy is described in terms of the electromechanical coupling factor, k_{ij}, and relates to the charge-coefficient by:

$$k_{ij} = \frac{d_{ijk}}{\sqrt{s_{ijkl}\varepsilon_{ij}}} \tag{2.5}$$

where s_{ijkl} is the elastic compliance and ε_{ij} the permittivity. k_{ij} is always < 1 since electromechanical transduction is never perfect.

To reduce the complexity of describing material-properties in their tensorial form, it is convenient to abbreviate pairs of interchangeable indices, ij, to a single index, when working with symmetric tensors. The directions are then written as $11 \rightarrow 1, 22 \rightarrow 2, 33 \rightarrow 3, 23 \text{ or } 32 \rightarrow 4, 13 \text{ or } 31 \rightarrow 5, 12 \text{ or } 21 \rightarrow 6$. This is known as Voigt notation, and is valid for PZT, and used throughout the rest of this thesis. As illustrated in Figure 2.1, the in-plane, (a), out-of-plane, (b), and shear charge-coefficients in Voigt notation then reads: d_{31}, d_{33} and d_{15}, respectively.

2.1.2 Piezoelectric response in thin-films

Thin-film piezoMEMS are composite structures with the piezoelectric-layer sandwiched between the top and bottom electrodes as shown schematically in Figure 2.2, (a). The thin-film is clamped to the substrate, and the electromechanical transduction is enabled by the generation of an in-plane stress when a field is applied. This is illustrated in Figure 2.2, (b). Since the in-plane contraction of the piezoelectric film is restricted by the substrate-clamping, the film is tensile stressed along both in-plane directions: $\sigma_1 = \sigma_2$. In response, the substrate becomes compressively stressed in-plane. Since the substrate prohibits the film from expanding or contracting freely in the plane, both the in-plane strains, x_1 and x_2, are equal, and zero. In total this can be written as:

$$x_1 = x_2 = (s_{11}^E + s_{12}^E)\sigma_{12} + s_{13}^E\sigma_3 = 0 \tag{2.6}$$

Here, the elastic compliances at constant electric fields, s_{ij}^E, with units of $\left[\frac{m}{N}\right]$, are the inverse stiffness and a measure of flexibility. Out-of-plane, on the other hand, the film is not clamped and free to move. The out-of-plane strain, x_3, is, therefore, nonzero and can be written as:

$$x_3 = 2s_{12}^E\sigma_{12} + s_{11}^E\sigma_3 \tag{2.7}$$

Since clamping to the substrate limits the in-plane deformation, the piezoelectric coefficients of thin-films will always be smaller compared to its bulk counterpart. This is accounted for by effective piezocoefficients, $d_{33,f}$ and $e_{31,f}$, and can be expressed by combining (2.1) and (2.2) with (2.6) and (2.7):

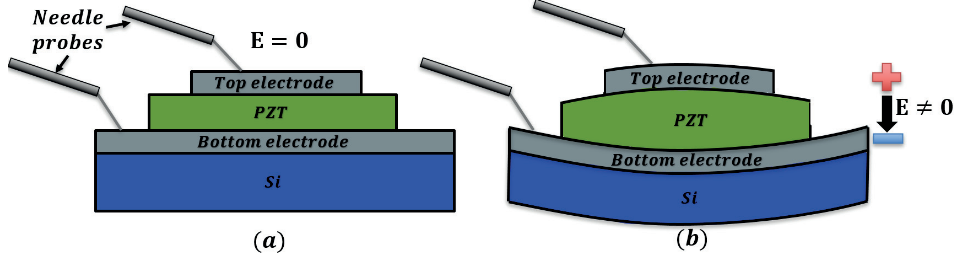

Figure 2.2: Schematic of the actuation of a typical thin-film piezoelectric stack. The piezoelectric thin-film is typically sandwiched between two electrodes as shown in (*a*). When a transverse field is applied, the substrate clamping enables in-plane electromechanical transduction.

$$e_{31,f} = \frac{d_{31}}{(s_{11}^E + s_{12}^E)} \left[\frac{C}{m^2}\right] \tag{2.8}$$

$$d_{33,f} = d_{33} - \frac{2s_{13}^E}{(s_{11}^E + s_{12}^E)} d_{31} \left[\frac{pm}{V}\right] \tag{2.9}$$

Both effective piezoelectric coefficients can be measured; $d_{33,f}$ by the displacement of a piezoelectric structure upon application of a field, and $e_{31,f}$ by measuring the generated charge of a mechanically stressed structure. Since the magnitude of $d_{33,f}$ often depends on the measurement geometry, $e_{31,f}$ is considered a more generalized parameter for describing the piezoelectric properties of the thin-film. Thin-films fabricated in this work, have typical piezocoefficients of $d_{33,f} \sim 90 - 130 \frac{pm}{V}$ and $e_{31,f} \sim 12 - 14 \frac{C}{m^2}$.

2.1.3 Ferroelectric perovskites

Piezoelectricity is a material-property limited to dielectrics belonging to 20 of the 21 non-centrosymmetric crystal classes (except for class 432). 10 of these classes have a polar axis, can develop a spontaneous polarization, and are pyroelectric. Ferroelectricity arise if the spontaneous polarization can be reoriented between two or more stable states by the application of an electric field and is an experimentally defined property. All ferroelectrics are also pyroelectric, piezoelectric and dielectric[5].

In general, all dielectrics, whether centrosymmetric or not, will elastically deform when subjected to an external electric field. This is a property known as electrostriction, and piezoelectric materials is a subset of electrostrictive materials, that they develop surface-charges when mechanically stressed. Piezoelectricity in ferroelectrics couples both to electrostriction and the spontaneous polarization, P_S, and the charge-coefficient is given by[6,7]:

$$d = 2QP_S\varepsilon \tag{2.10}$$

where Q is the electrostrictive coefficient with units of $\left[\frac{m^4}{C^2}\right]$ and $\varepsilon = \varepsilon_0\varepsilon_r$ the electrical permittivity (unitless), a measure of the materials polarizability. Some of the largest piezoelectric responses are found in ferroelectric perovskite oxides with the ABO_3-structure, where A and B are both cations, and O oxygen. Perovskite multicomponent structures are therefore particularly interesting for applications, and well-known ferroelectric perovskites including $BaTiO_3$[8], $LiNbO_3$[9] , $BiFeO_3$[10] and $Pb(Zr,Ti)O_3$[4].

All ferroelectric perovskites undergo a phase transition from a high-temperature non-polar to a low-temperature, ferroelectric polar phase when cooled down through the Curie-temperature, T_C. Above T_C the permittivity, ε, follows the Curie-Weiss law:

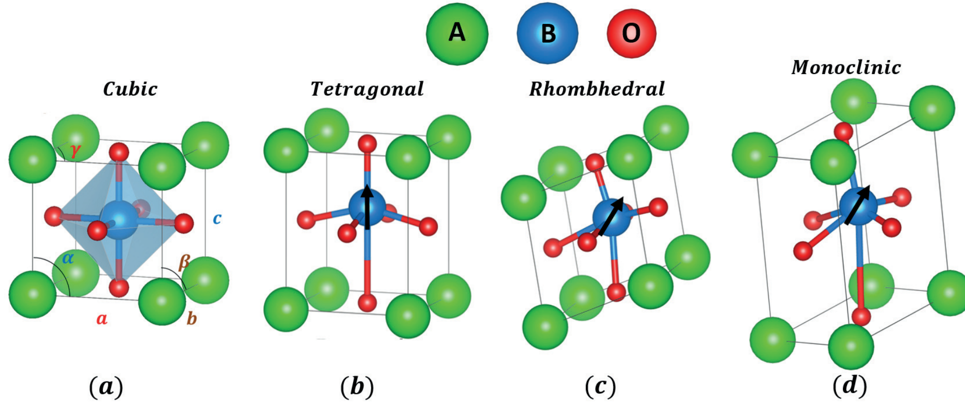

Figure 2.3: Schematic of the perovskite ABO_3-structure in the high-temperature paraelectric cubic phase, (a), and three common low-temperature polar phases: tetragonal, (b), rhombohedral, (c), and monoclinic, (d). The black arrows indicate the polar axes along which the spontaneous polarization may form. For PZT, Pb takes the A-site and Zr/Ti the B-sites in the BO_6-octahedra.

$$\frac{\varepsilon}{\varepsilon_0} = \frac{C}{T - T_C} \tag{2.11}$$

Here ε_0 is the vacuum permittivity, and C the Curie-constant. Above T_C, the phase is centrosymmetric cubic and paraelectric, and no polar axes exist. This is illustrated in Figure 2.3 (a), where the sides, a, b, c and angles α, β, γ of the cuboid are indicated. In the cubic phase, $\alpha = \beta = \gamma = 90^o, a = b = c$. In many instances, perovskites adapt a non-centrosymmetric, distorted ferroelectric phase below T_C. In general, the ferroelectric distortion in perovskites is due to a displacement of the B-cation relative to the A-cation and O in the crystal lattice. A hybridization between the oxygen 2p orbitals and the d-orbitals of the B-cation, stabilizes the off-centred displacement relative to the lattice, and induces a spontaneous polarization along one of the polar axes[11]. Three common ferroelectric phases are shown schematically in Figure 2.3 (b)-(d): tetragonal ($\alpha = \beta = \gamma = 90^o, a = b \neq c$), rhombohedral ($\alpha = \beta = \gamma \neq 90^o, a = b = c$) and monoclinic ($\alpha = \gamma = 90^o \neq \beta, a \neq b \neq c$). The black arrow indicates the spontaneous polarization along one of the polar axes. In the tetragonal phase, the spontaneous polarization can develop along any of the (100), (-100), (010), (0-10), (001) and (00-1) directions. The rhombohedral phase has four polar axes, and the spontaneous polarization can develop along any of the (111), (-111), (1-11), (11-1), (-1-11), (11-1), (-11-1), and (-1-1-1) directions.

In ferroelectric perovskites, the structural changes associated with the phase transition creates regions within the material where the spontaneous polarization is approximately aligned. Such regions are called ferroelectric domains and forms to minimize the electrostatic and elastic energy of the structure when cooled through the paraelectric-ferroelectric phase transition. Domains are separated by domain-walls and the direction of the polarization in two neighboring domains determines the domain-wall angle. A 180° domain-wall arise if the polarization in the neighboring domains are oppositely oriented, and a 90° domain-wall if the two polarizations are perpendicularly oriented. Only 90° or 180° domain-walls exists in the tetragonal phase, while in the rhombohedral phase 180°, 71° or 109° domain-walls exist[5,12]. A spontaneous polarization in ferroelectrics is also associated with a spontaneous strain. Regions with uniform spontaneous strain are called ferroelastic domains. Both the ferroelectric and ferroeleastic domain pattern affect the piezoelectric and dielectric properties of piezoelectric thin-films.

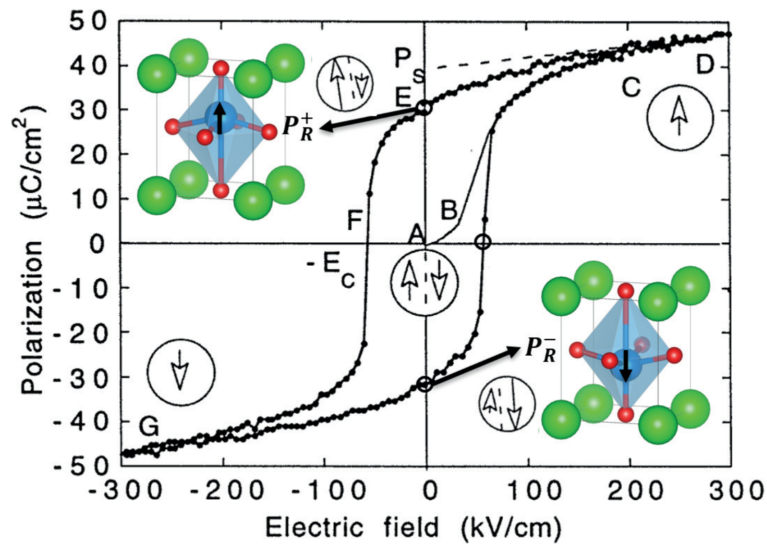

Figure 2.4: Ferroelectric hysteresis curve. For small fields, A-B, the polarization develops linearly with the field. The switching of ferroelectric domains at higher fields causes the polarization to increase, nonlinearly, B-C, until all domains are approximately aligned with the field, C-D. Upon removal of the field, a remnant polarization, P_R, remains due to the off-centred displacement of the B-cation relative to the lattice, D-E. The insets exemplify the remnant polarization states for a tetragonal ferroelectric. The process can be reversed by reversing the field, E-F-G, giving rise to the ferroelectric hysteresis. Adapted from[5].

2.1.4 Ferroelectric switching

Polarization reversal distinguishes ferroelectrics from other dielectrics. The process of switching the polarization in a ferroelectric, by applying an electric field, result in a polarization-field (P-E) hysteresis loop as shown in Figure 2.4. The polarized state is exemplified for a tetragonal perovskite in the insets, and the domain-pattern indicated by the circle and arrows. When a field is applied from an initially unpolarized state (point A), the polarization starts to reorient with the field. The B-cation displace relative to the unit cell, and in small fields, the polarization develops linearly with the applied field (segment AB). As the field increases, domains begin to re-orient, and the polarization switches nonlinearly with the applied field (segment BC). At higher fields, domains, move, nucleate and grow until approximately all domains are reoriented with the field (segment CD). The polarization saturates. Upon removing the applied field, the B-cation resides in an off-centered position relative to the unit cell, and some domain-alignment remains, as indicated by the segment DE. Altogether, this induces a nonzero remnant polarization, $\mathrm{P_R}$, at zero field. Reversing the field reverses the polarization (segment EF), which the coercive field, $\pm\mathrm{E}_C$, is the field needed to zero out the polarization, as indicated by the curve's positive and negative intersect with the x-axis. The depicted polarization-process can be reversed by reversing the electric field (segment FG), giving rise to a ferroelectric hysteresis.

2.1.5 Contributions to the piezoelectric response

Strain and electric polarization are coupled in polycrystalline ferroelectric perovskites, and three important contributions influence their overall piezoelectric response[13]. First, the crystal unit-cell change dimensions as the B-cation displace relative to the crystal lattice, when a field is applied. The

averaged crystallographic contribution within the ferroelectric/ferroelastic domains is known as the intrinsic response. Second, domain-walls can move when a pressure or an electric field is applied on the ferroelectric. This leads to a dynamic contribution from the domain-wall motion to the electromechanical properties of the ferroelectric, known as the extrinsic response. Only the motion of non-180° domain-walls can develop a strain and contribute to the piezoelectric effect. In polycrystalline PZT, extrinsic contributions can account for more than 50 % of the piezoelectric response[14–16]. Both the intrinsic and extrinsic responses occur within crystallites, and can be affected by various defects, including dislocations, chemical defects and grain-boundaries. Third; as polycrystals consists of multiple crystallites with different crystallographic orientations, applying an external electric or mechanical field, causes the various crystallites and grains to electrically and mechanically interact with each other. This modifies the macroscopic response, affecting both the intrinsic as well as the extrinsic contributions to the piezoelectric response[15,17].

Most piezoMEMS devices based on ferroelectric materials are actuated using unipolar fields. Aligning the ferroelectric domains in the direction of the applied field, enhances and stabilizes the built-in piezoelectric properties of ferroelectric thin-films. This is done through a process known as poling, in which an electric field in the order of 3-5 times the coercive field, is applied to the sample at elevated temperatures for an extended period.

2.1.6 Film thickness and microstructure

Ferroelectricity arise due to long-ranged dipolar interactions and depends on the thin-film's thickness as well as its microstructure, i.e. the arrangement of phases and defects on the microscopic level, including crystallographic orientation (texture), phase -and grain-distribution. First, the physical properties change as the film thickness decreases. Three important factors altering the thin-film's electromechanical properties compared to bulk, are the pinning of domain walls in surface inhomogeneities, the presence of interface dielectric-layers and differing mechanical boundary-conditions. Important effects of these factors include a considerably increase in the coercive field, decreased remnant polarization (tilted hysteresis) and a reduced the domain-wall mobility in thin-films compared to bulk[5,18].

A high density of mobile non-180° domain walls are generally desired to increase the extrinsic piezoelectric response[19–22]. Indeed, the film's domain structure as well as inter-grain interactions are sensitive to the microstructure[5]. Grain boundaries, internal and external surfaces, defective crystallographic planes, and interfaces all act as pinning sites for the motion of non-180° domain-walls [15,23]. Furthermore, the grain-size strongly influences the domain-structure as well as the domain-wall mobility. For PZT, films with grain-sizes in the submicron range, facilitates fewer mobile 90° domain-walls, compared to films with grain-sizes in the 1-10 µm range. As a result, the piezoelectric the piezoelectric as well as the dielectric response decrease with decreasing grain-size. Consequently, grain-size optimization of the film is thus important for tuning the piezoelectric response of thin-films[24,25]. For the films used in this work, the grain-sizes ranged from 150 to 500 nm.

The film texture directly influences the polarization-dynamics and the film's piezoelectric response[14,17,26–30]. In crystalline films, the highest piezoelectric response appears in predominantly (001)-orientated films[4]. In polycrystalline films, containing multiple differently oriented grains, the piezoelectric response is averaged over all grains. The interactions between differently oriented grains in polycrystals, is a complex correlated process, and the optimal mix of orientations in polycrystalline films can depend on the processing conditions[17]. The polycrystalline films used in this work, displayed the largest piezoelectric response around a 90% (001) and 10% (110)-orientation.

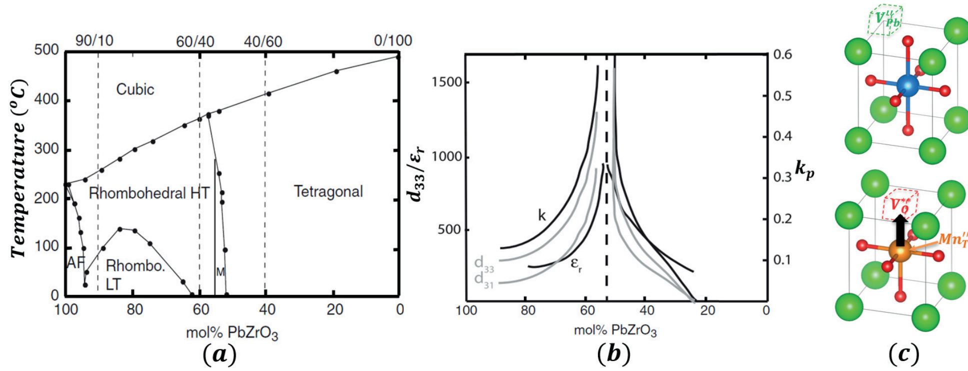

Figure 2.5: Phases, (a), and dielectric/piezoelectric properties, (b), as a function of compositional variations of PZT[5]. Ti-rich compounds are tetragonal and Zr-rich compounds rhombohedral and separated by a monoclinic phase as shown in (a). Compositions close to the MPB, indicated by the dotted line, show significantly enhanced piezoelectric and dielectric properties. (c) and (d) shows the two most encountered point defects in PZT; lead vacancies, V_{Pb}'', and oxygen vacancies, V_O^{**}. Upon acceptor-doping, such as Mn_{Ti}'', stabilized defect dipoles between the acceptor dopant and V_O^{**} creates a "hard" ferroelectric. Most thin-films used for piezoMEMS are polycrystalline and adapts a columnar structure. SEM-images side -and top view of a ~2 µm PLD-deposited PZT thin-film from this work is shown in (e) and (f).

2.2 Lead zirconate titanate

Ferroelectric $PbZr_xTi_{1-x}O_3$, hereafter PZT, has considerably higher dielectric and piezoelectric properties compared to other piezoelectrics, such as AlScN or ZnO [4,31]. PZT is, therefore, a technologically important material for thin-film piezoMEMS applications[1,2,32–38]. The piezoelectric and ferroelectric properties of PZT depend on its composition, structural phases, microstructure, and defect structure[14]. Here, the structure-property relations of PZT are discussed.

2.2.1 Structure-property relations

PZT is a solid solution between rhombohedral anti-ferroelectric $PbZrO_3$ and tetragonal ferroelectric $PbTiO_3$. Pb occupies the corner A-site, while Zr/Ti are randomly distributed over B-sites in BO_6-octahedral positions (see Figure 2.3 (b)). T_C of PZT is around 380^oC and depends on the composition[39]. As illustrated in Figure 2.5 (a), various ferroelectric phases exist depending the Zr/Ti-ratio. Ti-rich compounds are tetragonal and Zr-rich compounds are rhombohedral. A monoclinic phase exists between the tetragonal and rhombohedral phase. The compositional region where the tetragonal phase transforms into the monoclinic and rhombohedral phase is called the morphotropic phase boundary (MPB). For PZT, the MPB is located around $x = 52$ mol % $PbZrO_3$, that is, $PbZr_{0.52}Ti_{0.48}O_3$. For compositions close to the MPB, the ferroelectric and ferroelastic domains can more easily reorient with the applied field compared to compositions far away from the MPB. This results in a significant enhancement of the dielectric, piezoelectric, and ferroelectric compliances, and coupling coefficient as shown in Figure 2.5 (b), making MPB-compositions particularly interesting for piezoMEMS applications[4,15]. For this work, compositions based on rhombohedral/monoclinic $Pb(Zr_{0.52}Ti_{0.48})O_3$, and tetragonal $Pb(Zr_{0.40}Ti_{0.60})O_3$ are used.

2.2.2 Defect structure

Point-defects in PZT influences its properties. The most common point-defects are negatively charged lead vacancies, V_{Pb}'', and positively charged oxygen vacancies, V_O^{**}, as illustrated in Figure 2.5 (c)[40]. The Kröger-Vink notation is used.

Undoped PZT is acceptor-dominated, and the PZT-properties can be tailored for practical applications by chemical doping[41]. Acceptor-doping is done using lower-valence elements, such as A-site distributed K^+, (K_{Pb}') or B-site distributed Mn^{2+} (Mn_{Ti}'')[42,43]. Acceptor dopants are charge compensated by V_O^{**}, creating defect dipole complexes such as $(M_{Ti}'' - V_O^{**})^x$ or $(Mn_{Ti}' - V_O^{**})'$, which stabilize the ferroelectric domain structure. The short-ranged motion of V_O^{**} in the BO_6-octahedra network allows for a reorientation and alignment of these defect dipole complexes by an electric field [44–47]. Furthermore, V_O^{**} is known to immobilize domain wall motion, thus acceptor-doping lowers $e_{31,f}$ compared to undoped PZT[48]. Altogether, this results in relatively high coercive fields and high remnant polarization, characteristic for what is known as "hard" PZT[49–51]. Generally, acceptor-doped PZT has a high concentration of V_O^{**}, and displays high Quality-factors, high transition temperatures, low compliances and reduced permittivity and dielectric loss, which is beneficial for resonator -and ferroelectric RAM-applications[52].

Donor doping is done using higher-valence elements, such as La^{3+} on A-sites, La_{Pb}^{*}, or Nb^{5+} on B-sites, Nb_{Ti}^{*}. Donor-dopants are compensated by electrons and V_{Pb}'' and overall reduces the V_O^{**} -and hole concentration, internal stress, space-charge accumulation at domain walls and the movement of V_O^{**} around the oxygen octahedra[42]. Altogether, donor-doping increases the domain wall mobility, and thereby the piezoelectric response of PZT. Donor-doped PZT is "soft", displaying a hysteresis curve characterized by low coercive fields and low remnant polarization. In contrast to hard PZT, soft PZT is characterized by a high permittivity and dielectric loss, large $e_{31,f}$, and low T_C, quality-factor, coercive fields and conductivity compared to undoped PZT. This makes soft PZT highly attractive for low-frequency piezoMEMS-applications [35]. In this work, undoped $PbZr_{0.52}Ti_{0.48}O_3$ and Ba-doped, $Pb_{0.9}Ba_{0.1}Zr_{0.40}Ti_{0.60}O_3$, are investigated. Isovalent doping with Barium has a softening effect yet reduces the dielectric loss, T_C and crystallization-temperature of PZT[53,54].

The PZT defect structure, and in particular V_O^{**}, is important for reliability. Since PZT is a mixed ionic conductor the motion of electrons, holes and mobile ions, all influences the charge transport and electrical properties of PZT[55]. Upon prolonged exposure to high electrical fields, V_O^{**} migrates across the film and accumulate near the cathode-region[56]. The net positive interface charge creates a charge gradient which is compensated by injected electrons from the cathode. As a result, interfacial space-charge layers grow, and creates additional domain-wall pinning sites. This immobilizes the domain-wall motion, and, since more than 50 % of the piezoelectric response stem from domain-wall interactions, considerably suppresses the piezoelectric response[5]. Additionally, charge-injection degrades the electrical resistance with time, eventually leading to time-dependent dielectric breakdown[57,58]. In particular, electrons injected into the unfilled d states of Ti^{4+}near the conduction-band, contributes considerably to degradation[59]. Also, the loss of PbO, typically occurring during film-processing, can increase the V_{Pb}'' concentration near the electrode-interfaces, creating trapping-centres for holes close to the valence band of PZT[60].

Furthermore, PZT facilitates protonic defects in the form of protonic interstitials [48,61] and hydrated V_O^{**}[40,62–65]. The proton defect-concentration is controlled by the number of V_O^{**} and the number of interstitials PZT can accommodate and influences the piezoelectric and dielectric properties of PZT[66]. This is further discussed in Manuscript (II)-(III).

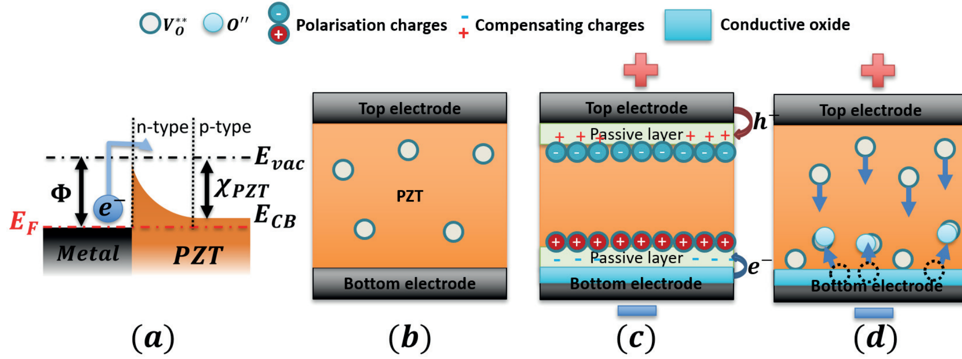

Figure 2.6: Schematic of electrode-induced processes. A Schottky-barrier at the electrode-PZT junction is required to obtain a rectifying contact, (a). The barrier height, Φ, prevents charge-injection and depends on the difference between the metal work-function and PZT affinity. Despite being a p-type semiconductor, the interface is n-type and requires the metal to have a larger work function than PZT to form a rectifying contact. A pristine PZT-stack is shown schematically in (b). When applying an electric field, electrons, holes and mobile ions will change the electrical properties of PZT over time. The movement and accumulation of V_O^{**} near the cathode region, causes interfacial charge-injection, domain-wall pinning and the formation of space-charge layers, which degrades the overall properties of PZT (c). For practical applications the effect of migrating V_O^{**} is compensated for, by using oxide electrodes, (d).

2.3 Integrating PZT thin-films in piezoMEMS

Thin-film piezoMEMS devices utilize the in-plane contraction of the clamped film for electromechanical transduction. Since the active electrode area is large compared to its thickness, large mechanical displacements can be achieved at relatively low driving voltages[67]. Embedding piezoelectric thin-films in devices is a complicated process, since thin-films differ from bulk with respect to the applied field and the mechanically clamped boundary-conditions. This section reviews material requirements and aspects related to the fabrication process that must be considered for integrating PZT in thin-film piezoMEMS. Control of the interface properties via PZT-deposition is briefly discussed.

2.3.1 Properties of the PZT-electrode system

PZT is usually integrated into sensors and actuators as an electrode-piezoelectric-electrode thin-film stack, as illustrated in Figure 2.6 $(a)-(d)$. In this work, the template stack consists of PZT/$LaNiO_3$(10nm)/Pt(100nm) Ti(10nm)/SiO_2/Si, where the thickness of the PZT layer and the choice of top electrode materials is varied. The electrodes are critical components of the device and determines much of the device performance. Generally, the electrode should; (i) ensure a low-leakage rectifying contact with PZT, (ii) be chemically compatible with all materials in the piezoelectric stack, (iii) promote the desired film microstructure, (iv) adhere PZT to the substrate and (v) contribute to a reliable long-term device operation. This will be discussed in the following.

(i) Rectifying contact

PZT is a p-type semiconductor with a bandgap of 3-4 eV[68]. However, an n-type layer is present at the electrode interface so that a rectifying contact is obtained only when the electrode metal has a work-function larger than that of PZT[48]. Generally, a rectifying contact is characterized by a Schottky-barrier at the metal-semiconductor interface, preventing charge-injection from the electrode metal into PZT. This is schematically illustrated for a metal-PZT contact in equilibrium in Figure 2.6 (a). Upon contact,

the valence and conduction bands (E_{CB}) of PZT will bend to keep the vacuum-level continuous across the interface and align the fermi-levels. As a rule of thumb, the Schottky barrier height to an n-type semiconductor, Φ_B, depends on the difference between the metal work-function, Φ_M, and the PZT electron affinity, χ_{PZT} (~$3.5\ \mathrm{eV}$); $\Phi_B - \chi_{PZT}$. An important electrode-requirement is, therefore ,to use metals with a work function substantially larger than χ_{PZT} to reduce the leakage across the interface[69]. Metals such as Pt, Au, or Ti with work functions of around 5.3, 5.1, and 4.35 eV, respectively, are good candidates and therefore commonly utilized[70–72]. For these metals, the theoretically predicted Schottky-barrier heights forming upon contact are $\Phi_{B,Pt} = 1.45, \Phi_{B,Au} = 1.39$ and $\Phi_{\mathrm{B,Ti}} = 1.16$ eV[73]. However, various interface-effects related to the fabrication-process and defect chemistry, can significantly alter the barrier height compared to theory, such that the actual barrier-height of the stack must be measured[74,75]. In the current work, Pt, Pt with 10 nm Ti adhesion-layer, $\mathrm{LaNiO_3}$ and Au with a Ti (10 wt% W) adhesion-layer are chosen as electrode-systems.

(ii) Chemical compatibility

PZT cannot be directly integrated with Si due to interfacial reactions and interdiffusion at elevated processing temperatures. The bottom electrode must, therefore, provide the chemical interdiffusion-barrier between the substrate and PZT. The electrode must, therefore, be an excellent electrical conductor, and integrate well with the substrate to act as a seed-layer for the PZT growth. Pt is well-matched with PZT, shows good temperature stability, few interface reactions, and can be grown directly onto $\mathrm{SiO_2}$ to form smooth and well-oriented films[72,76].

(iii) Microstructure

In contrast to bulk PZT, the crystallographic orientation of thin-films is controlled directly by the substrate upon which the film is deposited[77]. Thin-films are grown either by physical or chemical deposition methods directly on the electrode. An atomically flat and well-oriented electrode is a prerequisite for achieving the desired grain-size and film texture. The kinetics of growth can be manipulated either by tuning the deposition-parameters, such as temperature or deposition pressure, or by adapting a seed-layer, which promotes the desired film orientation[78]. The seed-layer is deposited either as an additional buffer-layer or integrated directly with the bottom electrode[79,80]. Common seed-layers are Ti and $\mathrm{TiO_2}$ promoting a (111)-orientated film[81,82] or PbO and $\mathrm{PbTiO_3}$ promoting a (001)-orientated film[27,83]. For the seed-layer being directly integrated into the electrode, (111)-oriented Pt and (001)-oriented $\mathrm{SrRuO_3}$ or $\mathrm{LaNiO_3}$ are good choices, which all promote a (001)-oriented PZT-growth[84–86]. For this work, 10 nm (001)-oriented $\mathrm{LaNiO_3}$ is used as combined bottom electrode and seed.

(iv) Substrate adhesion

PZT- based thin-film structures cannot be integrated with Si without adequate film-substrate adhesion. Post-deposition annealing at elevated temperature in and $\mathrm{O_2}$-atmosphere, can improve the adhesion-strength, though often at the cost of hillocking[72,76,78]. Interfacial adhesion-layer between the electrode and the Si substrate, are also commonly used for improving adhesion. Both approaches have here been pursued. Both annealing and Ti-adhesion was used for improving the adhesion to Pt. Ti and $\mathrm{TiO_2}$ adhesion-layers was used for adhesin to the Si substrate.

(v) Polarization fatigue

Long-term degradation-mechanisms imposed by chemical defects, diffusing or drifting in applied electric fields, can be mitigated by engineering the electrode-interface. Issues related to $\mathrm{V_O^{**}}$, as discussed in 2.2.2, are considerably reduced by depositing a conductive oxide layer between the electrode and PZT. Upon contacting, however, passive-layers with suppressed piezoelectric and dielectric properties will form at the electrode-PZT interface, as illustrated in Figure 2.6 (c). If not

considered, these layers will grow, quickly degraded the functional properties of PZT. Oxide electrodes have been shown to mitigate V_O^{**}-related issues by the supply of additional oxygen, (Figure 2.6 (d)). Commonly used oxide electrodes include $SrRuO_3$ [51,80], IrO_2[87] and $LaNiO_3$[79,88] and significantly increases time-to-failure[68,87]. The devices made in this work are designed for positive unipolar actuation, thus $(001) - \text{oriented } LaNiO_3$ is only deposited on the bottom electrode.

(vi) Electrode interface

Stoichiometric films with little compositional gradients are desired for maximizing the dielectric breakdown strength. Loss of volatile elements, lead in particular, can severely degrade the Schottky-barrier, and PZT properties, resulting in reduced breakdown-strength, leakage and early stage-failure[75]. The interface quality in this study is ensured in the fabrication-process by using oxygen-containing atmospheres during the annealing steps and lead-excess in the PLD-targets and solutions for chemical deposition.

2.3.2 Mechanical stresses in thin-films

In many instances, excessive mechanical stress may limit domain wall mobility, suppress the film's dielectric and piezoelectric properties, and decrease reliability. There are three main components of stress in polycrystalline PZT films; residual stress, σ_R, applied stress, σ_A, and piezoelectric stress, σ_P. The total film stress is the sum of the three components:

$$\sigma_{tot} = \sigma_R + \sigma_A + \sigma_P \; [MPa] \tag{2.12}$$

For polycrystalline films, one major stress-contribution stems from σ_R which is comprised of intrinsic, σ_i, and thermal, σ_T, stresses[2,15,89,90]. The intrinsic stress is influenced by the various deposition parameters (pressure, power, target-substrate distance etc.)[91]. Thermal stress evolves upon cooling from the deposition temperature due to a mismatch between the thermal expansion of the film and substrate. σ_T calculated using the difference in deposition and application temperature, ΔT [15,90]:

$$\sigma_T = E_f(\alpha_f - \alpha_S)\Delta T \tag{2.13}$$

Here α_f and α_S are the thermal expansion coefficients of the film and substrate and E_f the Young's Moduli of the film. If $\alpha_S > \alpha_f$ the film will have a compressive thermal stress ($\sigma_T < 0$) and if $\alpha_S < \alpha_f$ the thermal stress is tensile ($\sigma_T > 0$) after cooling from the deposition temperature. Cooling down through T_C, is associated with structural changes from the non-polar to the polar phase, causing ferroelastic domains to form due to the relative difference in unit cell dimensions. This affects the domain-state of PZT. $\sigma_R < 0$ results in a preference towards out-of-plane c-domains, and $\sigma_R > 0$ in a preference towards in-plane a-domains[28,87,92]. PZT grown on Si substrates, with $\alpha_S < \alpha_f$, has a tensile residual stress, promoting a higher a-to-c-domain ratio compared to for examples Ni or MgO-substrates where $\alpha_S > \alpha_f$. For the latter, a higher c-to-a domain ratio is promoted[93]. In general c-domains have large out-of-plane polarization and a lower out-of-plane permittivity, beneficial e.g. for FERAM-applications[36,38,80,94,95]. In comparison a-domains have a lower out-of-plane polarization and larger out-of-plane permittivity, beneficial for e.g. energy-harvesting applications[96,97].

Since PZT is a brittle ceramic, PZT thin-films can only withstand a total critical stress, typically in the range of $\sigma_C \approx 550\,MPa$, before cracking[98]. Since σ_P is the applicable stress, increased operating range, and reliability of piezoMEMS-devices can be achieved by minimizing the total stress of the device stack. Substrate-matching, film-thickness, and stress-compensating layers are all used for film-stress reduction in this work. All polycrystalline films are grown on Si substrates with a 1.6 µm SiO_2 stress-compensating layer. 1-2 µm thick films are used, and the PZT has an average tensile stress of around 250 MPa.

2.4 Advances in piezoMEMS reliability

Operation in realistic environments is a key concern for developing and commercializing piezoMEMS-devices[33,66,93,99,100]. In recent years, the impact of the various ambient stressors has, therefore, received increasing attention, with multiple approaches being pursued to study reliability[101–104]. For ferroelectric RAM -and resonator-applications PZT-based devices have demonstrated up to 10^{15} cycles in a lab-scale environment, without significant apparent degradation[105–107]. Under intended "normal usage", this translates to years of continuous operation before failure. In comparison, a typical median-time-to-failure in humid conditions range from a few minutes to a few hours under comparable electrical and mechanical loading conditions[108,109]. Devices used in this thesis, which initially exceeded 10^{11} cycles without significant fatigue nor failure in dry conditions, reduced to $\sim 10^{7}$ cycles before failing in humid conditions.

This section reviews the state-of-the-art within the reliability of piezoMEMS. Based on initial studies on factual thin-film piezoMEMS devices from this work, the various lifetime-limiting stressors are categorized according to its apparent severity; (i) ambient humidity, (ii) (electro)mechanical stress, (iii) DC electrical field reliability and (iv) aging and polarization fatigue[34,103,110–113]. Each point will be discussed in the following.

2.4.1 Ambient humidity

Operation in humid conditions has been shown to significantly decrease the breakdown-strength and median-time-to-failure (MTTF) of PZT-based structures and devices[33,108]. Failure is manifested as an early onset of leakage transients with a duration of µs-ms and amplitude of µA-mA, as illustrated in the lower part of Figure 2.7 (*a*)[99,108]. As a result of large localized current densities and Joule-heating evaporating the stack material, so-called black spots, in this work referred to as electrothermal breakdown-events, forms across the electrode surface. As illustrated in Figure 2.7 (b), holes penetrate the entire stack from top to bottom and are hence irreversible. It has been found that such degradation arise partly from a combination of resistance-degradation[109], cracking[114,115] and conductive filament-formation through the film[116], as shown in Figure 2.7 (c). Dielectric breakdown occurs when a critical filament length is reached, and multiple new conductive pathways will start to form. From an applied perspective, to protect the surfaces is imperative to circumvent humidity-related issues[34,117–120]. However, fabricating adequate humidity-barriers remains a challenge since piezoMEMS-devices utilize complex electromechanically moving structures, are sensitive to increased stiffness, and are prone to mechanical and dielectric breakdown. Attention has therefore been focused on understanding the fundamental mechanisms driving humidity-related degradation to develop additional mitigation strategies. From microelectronics, it is well-known that filament growth from anode to cathode is expected in humid conditions when using electro-migrating electrode-materials, such as Ag or Ni [99,116,121–127]. Such electromigration is exemplified for Ag in the top image of Figure 2.7 (c). Though state-of-the-art piezoMEMS-devices typically employs non-electro-migrating electrode-materials[72], similar degradation and failure are still encountered in humid conditions[33,88]. From the development of FERAM, the effect of hydrogen from the processing environment has been well studied [61,88,128–130]. At elevated processing temperatures, incorporated hydrogen can impede the cubic-tetragonal phase transition[131], change the polarizability[132], reduce the optical band gap[129], decreases fracture-toughness[114,115] and cause severe resistance degradation[133]. This has shed light on the important role of controlling the piezoMEMS processing environment, yet such conditions differ significantly from the realistic operating ambient[108,123]. Recent work on proton-conducting materials suggests that the drift of protonic charge-carriers in surface water may be key to understanding humidity-related degradation during operation[40,62,65,134–138]. It has therefore been proposed that the electrolysis of water is essential

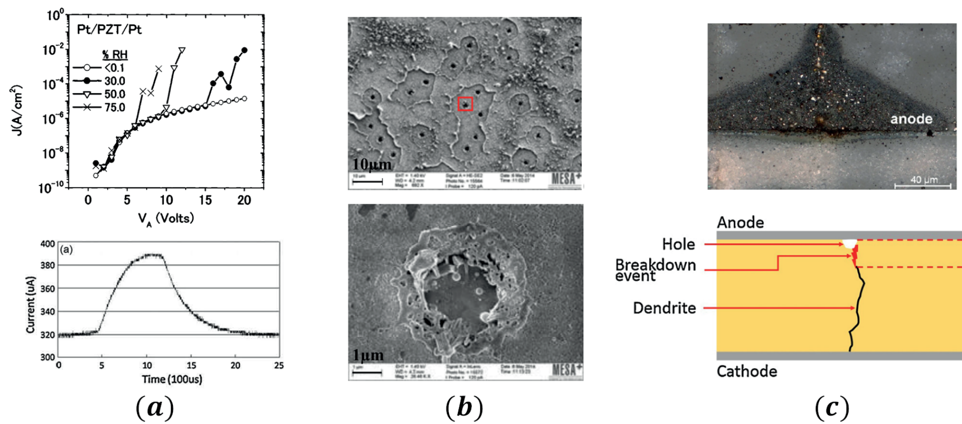

Figure 2.7: Degradation in humid conditions significantly lowers breakdown-strength and lifetime and is manifested as leakage transients and time-dependent dielectric breakdown decades earlier than in dry conditions, as shown in (a)[121,139]. Breakdown is generally associated with cracking and electrothermal breakdown-events, so-called black spots, as shown in (b)[108]. Electro migrating electrode-material from the anode to the cathode, is a commonly reported issue in humid conditions, in particular when using Ag or Ni-based electrodes[116]. A multi-breakdown model has been proposed, incorporating dendrite formation and eventually dielectric breakdown upon reaching a critical thickness as illustrated in (d)[99].

for humidity-related degradation, though this has not been further investigated[63,64,139,140]. Despite that some of the most frequently employed electrodes for piezoMEMS, including $SrRuO_3, IrO_2$ and Pt[141–145] are among the most electrochemically active materials towards water-splitting[125,146–150]. In this regard, it has also been shown that the pyroelectric effect, and polarization-state of PZT also may couple directly to electrochemical water-splitting, which could further accelerate such a process[151,152].

2.4.2 Mechanical limitations

To maximize the achievable electromechanical motion without cracking is an evident benefit for thin-film piezoMEMS devices[153]. PZT is a brittle ceramic, and thin-films are vulnerable to fracture. With application-areas expanding into mechanical energy harvesters[94] and long-stroke actuators[35], attention is given to understanding and improving the mechanical limitations of PZT and other ferroelectrics. Novel approaches, including residual stress-engineering[36,90,93,94,154], Vickers indentation[114,155,156], ball-on-three ball[157,158], Raman spectroscopy[159–162] and vacuum-setups for applying periodic stresses to the film[163,164] are being pursued.

Concerning the ferroelectric properties of thin-films, in-plane compressive stress can induce a partial *a*-to-c domain-reorientation in PZT, while in-plane residual tensile stress can induce a partial c-to-*a* domain-reorientation. This was demonstrated for PZT thin-films by Coleman et. al. by depositing PZT on Ni and Si substrates, as illustrated in Figure 2.8 (*a*). For the Ni substrate, an in-plane residual compressive stress increased c-to-a domain-ratio, and increased the remnant/maximum polarization and the extrinsic response, while decreasing the permittivity [26,165–167]. Conversely, depositing PZT on Si induce an in-plane tensile stress, decreasing the c-to-a domain ratio, and decreasing the remnant/maximum polarization and extrinsic response, while increasing the permittivity[168–170]. This is similar for bulk-materials, in which Webber et al. found that uniaxial mechanical loading decrease the out-of-plane polarizability and piezoelectric response as a result of ferroelastic domain-reorientation[155,171–174].

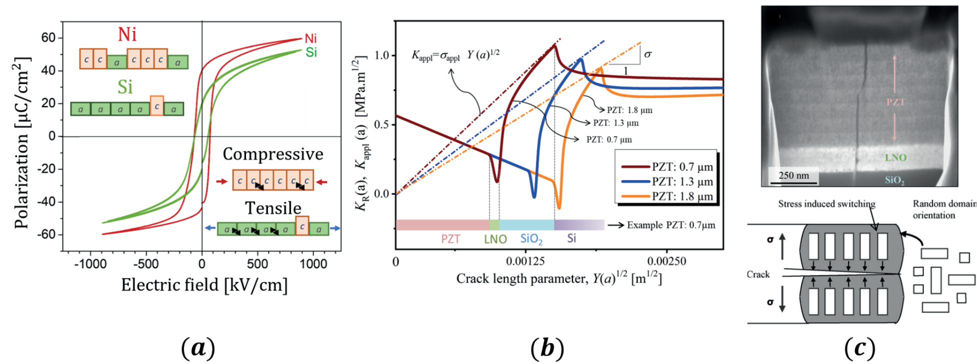

Figure 2.8: Investigation of mechanical limitations of ferroelectrics, adapted from[93,158]. In PZT, excessive in-plane compressive stress results in an a-to-c, while in-plane tensile stress results in a-to-c reorientation of ferroelastic domains, thus altering the ferroelectric properties of the film, (a). The crack initiation stress was found to decrease with increasing PZT film-thickness, while the apparent fracture toughness was found to decrease towards the interfaces of composite piezoelectric stacks, (b). When a crack is initiated, it is found to propagate through the PZT stack, and stop/turn at interfaces, top (c). Ferroelastic domain reorientation at the crack wake of a propagating crack, suppresses the crack propagation, (c).

Mechanical failure through crack initiation and propagation in thin-films has been studied by several authors[93,98,158,170,175,176]. For PZT, the coupled stress-energy criterion[1] has been found to be valid, also for thin-films[177,178]. The energy required to open a crack (increase in surface energy) increases as the film-thickness decrease. Therefore, the stress required for cracks to initiate is lower in thick, than in thin films. For bulk PZT, tensile uniaxial stress perpendicular to propagating cracks decreases the apparent fracture toughness (anti-shielding effect). As shown in Figure 2.8 (b), Coleman et. al. demonstrated that this was also true for a PZT/$LaNiO_3$/SiO_2/Si composite structure, in which the crack-initiation stress (slope of dotted curves) for a PZT thin-film under tensile stress decreases as the film-thickness increased. Furthermore, the apparent fracture toughness of PZT, was found to decrease from the surface towards the interface of the underlying layers. A similar decrease in fracture toughness was found through the $LaNiO_3$-layer, also under tensile stress, while for the compressively stressed thermal oxide, SiO_2, the fracture toughness increased through the layer. The lowest apparent fracture toughness occurred in the $LaNiO_3$-layer. As shown in the top right of Figure 2.8, top (c), propagating cracks were here found to shift direction when crossing the interface to the oxide electrode, and stop at the Si interface.

For bulk ferroelectrics, randomly oriented ferroelastic domains re-orient to alleviate stress. This results in a shielding-effect which impede crack-propagation, and increase the fracture toughness compared to non-ferroelectric brittle ceramics[179–181]. This is illustrated in the lower Figure 2.8 (c). Soft PZT, containing more mobile domain-walls compared to hard PZT, thus displays a larger fracture-toughening effect compared to hard PZT[155,171–174]. For thin-films, cracks can propagate through, and along the surface of the film. The clamped mechanical boundary-conditions and reduced domain-wall mobility compared to bulk, however, is expected to reduce this overall fracture toughening effect.

Lastly, it is mentioned an intimate connection between mechanical cracking and electrical failure of PZT has been reported for thin films, though more research is needed to fully understand the underlying mechanisms[75,108,113]. Also, increasing efforts is being put into understanding the effect of

[1] the energy needed to both initiate and propagate a crack must be exceeded for crack-initiation and propagation to occur

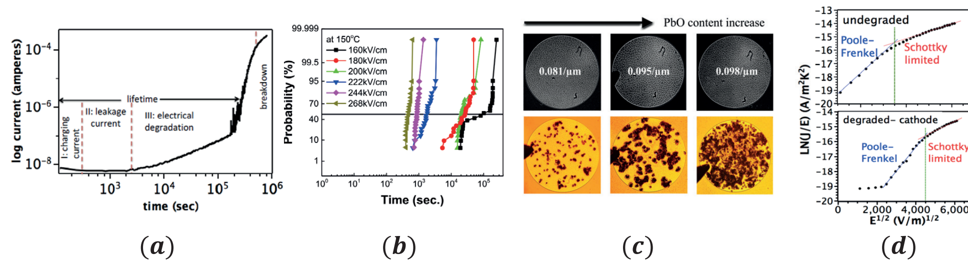

Figure 2.9: Electrical degradation is characterized by a charging current, leakage current, electrical degradation, and breakdown-regime, (a). HALT, employing elevated temperatures and high electrical fields are often used for assessing lifetime and reliability, and analyzed using Weibull statistics, (b). Time-dependent dielectric breakdown and electrical field breakdown are both closely connected to mechanical cracking and electrothermal breakdown, and often depends on the film processing conditions, (c). Here, the crack-density is controlled by varying the PbO content of the precursor solution for chemical solution deposited films. Prolonged exposure to high fields and temperatures, shifts the Poole-Frenkel and Schottky regimes along the V-axis, (d). Adapted from [75,184,201].

cyclic mechanical loading on degrading piezoelectric properties, as well as new routes for improving the fracture toughness of piezoceramics[182,183].

2.4.3 DC electrical field reliability

Prolonged exposure to high electrical fields changes the defect structure of PZT over time[166]. This changes the dominant conduction mechanism and affects the DC electrical field reliability, as illustrated in Figure 2.9 (*a*). Initially, polarization-relaxation, the release of trapped charges and the formation of space-charge regions results in an initial relaxation-regime and a decrease in leakage during time-dependent measurements[58]. A leakage-regime with initially slow kinetics is then encountered before the onset of electrical degradation, eventually leading to rapid kinetics and failure through time-dependent dielectric breakdown occurs. Lifetime and reliability are typically investigated by studying the trapping and release of charged species in PZT as a function of degradation-time. Due to the length of each experiment, lifetimes are extrapolated from highly accelerated lifetime-tests by exposing the samples to elevated temperatures and electrical fields[184,185]. Weibull-distributions, as shown in Figure 2.9 (b), in combination with voltage and temperature acceleration-factors are used to extrapolate device and structure lifetime, typically by adapting existing lifetime models to the relevant sample structure[186–188]. Like humidity and mechanically induced degradation, electrically degraded samples experience cracking and electrothermal breakdown-events during failure, as shown in Figure 2.9 (c). A Schottky-based degradation-model have been proposed to explain the phenomena, though with varying predictability due to a continually changing defect-structure with time[184,189]. To understand the degradation-dynamics, the involved species and conduction mechanisms, thermally stimulated depolarization currents[190], current-voltage[71], and impedance-spectroscopy techniques[191] are conducted. Recent development show that the relaxation-times of relevant defect species can also be utilized for characterizing the involved species[185,192]. It has been found that controlling doping and film stoichiometry, in particular close to the electrode interfaces is of high importance for DC reliability. Degradation, however, contradicts a purely Schottky-based degradation-model, since the dominant conduction mechanisms change with time[70,193,194]. Though donor-doping using e.g. Nb generally decreases the Schottky barrier height of pristine PZT-films, the median time-to-failure has been found to increase. Conversely, while Mn acceptor-doping increases the Schottky-

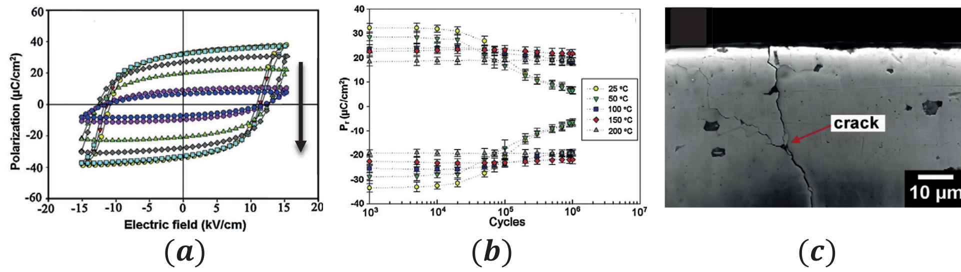

Figure 2.10: Polarization fatigue leads to a gradual loss of ferroelectric and piezoelectric properties with time, such as a diminishing ferroelectric hysteresis, as shown in (a). Fatigue and aging-related behavior is accelerated by field and temperature, as illustrated in (b). Since PZT is a brittle ceramic, cracking is also an integral part of fatigue, as shown in (c). This should be addressed by assessing the issues pointed out in section 2.4.1-2.4.2. Adapted from [180].

barrier height, the median time-to-failure decreases. A similar trend was found by reducing the feature-size of interdigitated electrode structures[195]. Both observations connect with processes promoting or impeding charge trapping within PZT. With time, the dynamics of charge release from various defects shifts the conduction from initially being Schottky-dominated to being Poole-Frenkel-dominated (Figure 2.9 (d)). Acceptor-doped samples show higher resilience since the activation energy for dissociating acceptor-induced defect-dipoles, for instance $Mn_{Ti}'' - V_O^{**}$ or $V_{Pb}'' - V_O^{**}$, are higher than for Nb-doped samples. For structured samples, sidewall-damages and dangling bonds from lateral patterning increase the activation energy needed for defect dipole-dissociation, thus improving DC lifetime.

Since films used for applications are getting ever thinner, the breakdown strength of PZT must also be improved. Atmospheric and solution-control has been pursued as a way to optimize the Pb- and Ti-content and improve the electrode-interface quality[74,75,194]. As illustrated in Figure 2.9 (c), the content of volatile elements, Pb and PbO in particular, determines much of the interface properties. Here the authors showed that the crack density directly correlated with the breakdown-strength and could be controlled by adjusting the amount of PbO in the precursor solution during chemical solution deposition. Again, this highlights the importance of well-processed samples.

2.4.4 Aging and polarization fatigue

If the abovementioned issues are solved, the final realm for improving PZT lifetime is through decreasing polarization-fatigue, i.e. the loss of piezoelectric and ferroelectric properties with time, (Figure 2.10 (*a*), (b)). This is especially relevant for high-frequency-applications, such as RF-switches, resonators and FERAM, which requires a large set of duty-cycles throughout their lifetime. The loss of properties is primarily due to the drift of ionic species, charge-injection, changes in the domain state and cracking resulting in a gradual loss of ferroelectric and dielectric properties over time[51,70,106]. Since thermodynamic processes dominate degradation, aging and polarization-fatigue is directly correlated with the applied field and temperature of the operating ambient[70,174,180,185]. Acceptor-doping, oxide electrodes, and poling improves the aging and fatigue characteristics[51,106,196–198]. In addition, controlling the electrical field-distribution over the piezoMEMS-device during operation show promising results towards decreased polarization-fatigue[193,199,200]. Well-processed samples, however, are expected to endure polarization fatigue-related issues throughout their lifetime.

The pristine properties of fatigued or aged samples can, in general, be regained through sample re-poling. However, in the case of mechanical cracking, the complete recovery by annealing or

re-poling is limited. This is illustrated for a fatigued sample in Figure 2.10 (c). Such effects are addressed by assessing issues pointed out in section 2.4.1-2.4.2.

2.5 Summary

Electromechanical transduction using the piezoelectric effect is attractive for MEMS-devices, and ferroelectric PZT is among the best piezoelectric materials currently available. PZT has a complex defect structure, and is sensitive to electrical fields, mechanical stress, and ferroelastic distortions. Integrating PZT in thin-film device-structures is not straight-forward, and careful considerations in terms of physical properties, chemical compatibility, and long-term stability of the used materials must be taken.

Reliable operation in realistic and harsh environments is a key challenge inhibiting the employment and continued technological development of PZT-based piezoMEMS-devices. Though there are multiple ways in which piezoelectric materials can degrade in real-life conditions, the ambient humidity is perhaps one of the most severe stress factors imposed by the operating ambient. Yet the underlying degradation processes and mechanisms are so far not well understood. Though imperative for improving reliability, encapsulating devices are often impractical and often not enough, and the involved mechanisms require a thorough understanding from both a theoretical and applied perspective. In this thesis, the challenges of humidity-related degradation are addressed from the standpoint of piezoMEMS structures and devices. The goal is to understand the mechanisms governing degradation in humidity, and how they affect real-life thin-film piezoMEMS devices.

Here, piezoMEMS-devices together with simple test-structures was used to study and understand the effects of degradation encountered in humid conditions. This is unique since issues studied on simple test-structures are not always directly transferrable to actual piezoMEMS devices. A retrofittable experimental setup was developed to investigate the dielectric, piezoelectric and ferroelectric properties under controlled ambient conditions. The lifetime-limiting factors from initial tests paved the way for designing simplified test-structures, used to elucidate the degradation-mechanisms. Measures for mitigating and recover samples from humidity-degradation were also investigated. Lastly, it was demonstrated devices with a three orders of magnitude enhanced lifetime compared to pristine devices, and the work suggest approaches for studying and improving reliability further.

References

[1] M. K. Mishra, V. Dubey, P. M. Mishra, I. Khan, *J. Eng. Res. Reports* **2019**, *4*, 1.

[2] C.-B. Eom, S. Trolier-McKinstry, *MRS Bull.* **2012**, *37*, 1007.

[3] P. Muralt, S. Trolier-McKinstry, *J. Electroceramics,* **2004**, *12*, 7.

[4] S. Trolier-McKinstry, S. Zhang, A. J. Bell, X. Tan, *Annu. Rev. Mater. Res.* **2018**, *48*, 191.

[5] D. Damjanovic, *Rep. Prog. Phys* **1998**, *61*, 1267.

[6] A. J. Bell, *J. Appl. Phys.* **2015**, *118*, 224103.

[7] F. Li, D. Lin, Z. Chen, Z. Cheng, J. Wang, C. Li, Z. Xu, Q. Huang, X. Liao, L. Q. Chen, T. R. Shrout, S. Zhang, *Nat. Mater.* **2018**, *17*, 349.

[8] M. Acosta, N. Novak, V. Rojas, S. Patel, R. Vaish, J. Koruza, G. A. Rossetti, J. Rödel, BaTiO3-based piezoelectrics: Fundamentals, current status, and perspectives. *Appl. Phys. Rev.* **2017**, *4*, 041305.

[9] V. Y. Shur, *Nano- and Microdomain Engineering of Lithium Niobate and Lithium Tantalate for Piezoelectric Applications*; 2nd ed.; Elsevier Ltd., 2017.

[10] H. Hojo, K. Oka, K. Shimizu, H. Yamamoto, R. Kawabe, M. Azuma, *Adv. Mater.* **2018**, *30*, 1705665.

[11] R. E. Cohen, *Nature* **1992**, *358*, 136.

[12] J. Fousek, V. Janovec, *J. Appl. Phys.* **1969**, *40*, 135.

[13] T. Rojac, D. Damjanovic, In *Japanese Journal of Applied Physics*; Japan Society of Applied Physics, 2017; Vol. 56.

[14] D. Damjanovic, *J. Am. Ceram. Soc.* **2005**, *88*, 2663.

[15] N. Bassiri-Gharb, I. Fujii, E. Hong, S. Trolier-Mckinstry, D. V Taylor, D. Damjanovic, *J. Electroceramics* **2007**, *19*, 47.

[16] F. Li, S. Zhang, T. Yang, Z. Xu, N. Zhang, G. Liu, J. Wang, J. Wang, Z. Cheng, Z. G. Ye, J. Luo, T. R. Shrout, L. Q. Chen, *Nat. Commun.* **2016**, *7*, 13807.

[17] J. Y. Li, R. C. Rogan, E. Üstündag, K. Bhattacharya, *Nat. Mater.* **2005**, *4*, 776.

[18] J. F. Ihlefeld, D. T. Harris, R. Keech, J. L. Jones, J. P. Maria, S. Trolier-McKinstry, *J. Am. Ceram. Soc.* **2016**, *99*, 2537.

[19] G. A. Rossetti, A. G. Khachaturyan, *Appl. Phys. Lett.* **2007**, *91*, 072909.

[20] I. P. Kaminow, *Proc. IEEE* **2008**, *66*, 1299.

[21] K. A. Schönau, L. A. Schmitt, M. Knapp, H. Fuess, R. A. Eichel, H. Kungl, M. J. Hoffmann, *Phys. Rev. B - Condens. Matter Mater. Phys.* **2007**, *75*.

[22] R. Ahluwalia, T. Lookman, A. Saxena, W. Cao, *Phys. Rev. B - Condens. Matter Mater. Phys.* **2005**, *72*, 014112.

[23] L. M. Denis, G. Esteves, J. Walker, J. L. Jones, S. Trolier-McKinstry, *Acta Mater.* **2018**, *151*, 243.

[24] O. Auciello, R. Waser, North Atlantic Treaty Organization. Scientific Affairs Division., I. NATO Advanced Research Workshop on Science and Technology of Electroceramic Thin Films (1994 : Maratea, *Science and technology of electroceramic thin films*; Kluwer Academic, 1995.

[25] I. N. Shabanova, N. V. Keller, *Surf. Interface Anal.* **2001**, *32*, 27.

[26] C. B. Yeager, Y. Ehara, N. Oshima, H. Funakubo, S. Trolier-Mckinstry, *J. Appl. Phys.* **2014**, *116*, 104907.

[27] N. Ledermann, P. Muralt, J. Baborowski, S. Gentil, K. Mukati, M. Cantoni, A. Seifert, N. Setter, *Sensors Actuators, A Phys.* **2003**, *105*, 162.

[28] R. C. Rogan, E. Üstündag, B. Clausen, M. R. Daymond, *J. Appl. Phys.* **2003**, *93*, 4104.

[29] T. M. Borman, S. W. Ko, P. Mardilovich, S. E. Trolier-McKinstry, *J. Am. Ceram. Soc.* **2017**, *100*, 4476.

[30] B. Noheda, D. E. Cox, G. Shirane, R. Guo, B. Jones, L. E. Cross, *Phys. Rev. B - Condens. Matter Mater. Phys.* **2001**, *63*, 014103.

[31] M. H. Lee, D. J. Kim, J. S. Park, S. W. Kim, T. K. Song, M. H. Kim, W. J. Kim, D. Do, I. K. Jeong, *Adv. Mater.* **2015**, *27*, 6976.

[32] T. Kobayashi, H. Okada, T. Masuda, R. Maeda, T. Itoh, *Smart Mater. Struct.* **2010**, *19*, 105030.

[33] R. P. Dahl-Hansen, T. Tybell, F. Tyholdt, In *2018 IEEE ISAF-FMA-AMF-AMEC-PFM Joint Conference, IFAAP 2018*; IEEE, 2018; pp. 1–4.

[34] P. Rafiee, G. Khatibi, M. Zehetbauer, *Microelectron. Int.* **2017**, *34*, 9.

[35] T. Bakke, A. Vogl, O. Zero, F. Tyholdt, I. R. Johansen, D. Wang, *J. Micromechanics Microengineering* **2010**, *20*, 1.

[36] C. Yeager, PZT Thin Films for Piezoelectric MEMS Mechanical Energy Harvesting, The Pennsylvania State University The, 2015.

[37] Y. He, B. Bahr, M. Si, P. Ye, D. Weinstein, **2019**.

[38] M. Pešić, U. Schroeder, In *Ferroelectricity in Doped Hafnium Oxide: Materials, Properties and Devices*; Woodhead Publishing, 2019; pp. 425–435.

[39] W. Hu, X. Tan, K. Rajan, *J. Eur. Ceram. Soc.* **2011**, *31*, 801.

[40] T. S. Bjørheim, A. Kuwabara, I. Ahmed, R. Haugsrud, S. Stølen, T. Norby, *Solid State Ionics* **2010**, *181*, 130.

[41] L. Eric Cross, In *Ferroelectric Ceramics*; Birkhäuser Basel: Basel, 1993; pp. 1–85.

[42] C. Slouka, T. Kainz, E. Navickas, G. Walch, H. Hutter, K. Reichmann, J. Fleig, *Materials (Basel).* **2016**, *9*.

[43] N. Setter, D. Damjanovic, L. Eng, G. Fox, S. Gevorgian, S. Hong, A. Kingon, H. Kohlstedt, N. Y. Park, G. B. Stephenson, I. Stolitchnov, A. K. Taganstev, D. V. Taylor, T. Yamada, S. Streiffer, Ferroelectric thin films: Review of materials, properties, and applications. *J. Appl. Phys.* **2006**, *100*, 51604–51606.

[44] B. Jaffe, W. R. Cook, H. L. Jaffe, *Piezoelectric ceramics,*; Academic Press: London ;New York, 1971.

[45] G. Arlt, H. Neumann, *Ferroelectrics* **1988**, *87*, 109.

[46] U. Robels, G. Arlt, *J. Appl. Phys.* **1993**, *73*, 3454.

[47] P. V. Lambeck, G. H. Jonker, *Ferroelectrics* **1978**, *22*, 729.

[48] K. Niwa, Y. Kotaka, M. Tomotani, H. Ashida, Y. Goto, S. Otani, *Acta Mater.* **2000**, *48*, 4755.

[49] A. K. Tagantsev, M. Landivar, E. Colla, N. Setter, *J. Appl. Phys.* **1995**, *78*, 2623.

[50] A. Gruverman, In *Multifunctional Oxide Heterostructures*; Oxford University Press, 2012; pp. 157–180.

[51] M. Grossmann, O. Lohse, T. Schneller, D. Bolten, U. Boettger, J. R. Contreras, H. Kohlstedt, R. Waser, In *Integrated Ferroelectrics*; 2001; Vol. 37, pp. 205–214.

[52] L. Extrapolation, I. E. Tool, *4*.

[53] H. Zheng, I. M. Reaney, W. E. Lee, N. Jones, H. Thomas, *J. Am. Ceram. Soc.* **2002**, *85*, 2337.

[54] K. Ramam, M. Lopez, *J. Phys. D. Appl. Phys.* **2006**, *39*, 4466.

[55] B. A. Boukamp, M. T. . Pham, D. H. . Blank, H. J. . Bouwmeester, *Solid State Ionics* **2004**, *170*, 239.

[56] G. Holzlechner, D. Kastner, C. Slouka, H. Hutter, J. Fleig, *Solid State Ionics* **2014**, *262*, 625.

[57] B. Akkopru-akgun, D. Marincel, T. Bayer, K. Tsuji, W. Zhu, C. Randall, M. T. Lanagan, S. Trolier-mckinstry, .

[58] L. M. Garten, M. Hagiwara, S. W. Ko, S. Trolier-McKinstry, *Appl. Phys. Lett.* **2017**, *111*, 122903.

[59] A. Matsutani, Z. Luo, S. Pojprapai, M. Hoffman, G. Pezzotti, *Appl. Phys. Lett.* **2009**, *95*.

[60] J. Robertson, W. L. Warren, B. A. Tuttle, D. Dimos, D. M. Smyth, *Appl. Phys. Lett.* **1993**, *63*, 1519.

[61] C. K. Huang, C. H. Chang, T. B. Wu, *J. Appl. Phys.* **2005**, *98*, 104105.

[62] S. Ø. Stub, E. Vøllestad, T. Norby, *J. Phys. Chem. C* **2017**, *121*, 12817.

[63] F. Messerschmitt, M. Jansen, J. L. M. Rupp, *Adv. Electron. Mater.* **2018**, *4*, 1800282.

[64] J. M. Polfus, T. S. Bjørheim, T. Norby, R. Bredesen, *J. Mater. Chem. A* **2016**, *4*, 7437.

[65] K. D. Kreuer, *Solid State Ionics* **1999**, *125*, 285.

[66] R. P. Dahl-Hansen, B. Akkopru-Akgun, J. M. Polfus, E. Vøllestad, L. M. Denis, K. Coleman, F. Tyholdt, S. Trolier-McKinstry, T. Tybell, *Submitted*.

[67] Yole Développement, **2019**.

[68] C. Prakash, T. C. Goel, **2005**, *369*, 135.
[69] H. N. Al-Shareef, D. Dimos, *J. Am. Ceram. Soc.* **2005**, *80*, 3127.
[70] Y. A. Genenko, J. Glaum, M. J. Hoffmann, K. Albe, Mechanisms of aging and fatigue in ferroelectrics. *Mater. Sci. Eng. B Solid-State Mater. Adv. Technol.* **2015**, *192*, 52–82.
[71] A. Klein, *J. Am. Ceram. Soc.* **2016**, *99*, 369.
[72] H. N. Al-Shareef, K. D. Gifford, S. H. Rou, P. D. Hren, O. Auciello, A. I. Kingon, *Integr. Ferroelectr.* **1993**, *3*, 321.
[73] J. Robertson, C. W. Chen, *Mater. Res. Soc. Symp. - Proc.* **1999**, *541*, 443.
[74] T. M. Borman, W. Zhu, K. Wang, S. W. Ko, P. Mardilovich, S. E. Trolier-McKinstry, *J. Am. Ceram. Soc.* **2017**, *100*, 3558.
[75] W. Zhu, T. Borman, K. DeCesaris, B. Truong, M. M. Lieu, S. W. Ko, P. Mardilovich, S. Trolier-McKinstry, *J. Am. Ceram. Soc.* **2018**, *102*, 1734.
[76] E. Vereshchagina, E. Poppe, K. Schjolberg-Henriksen, M. Wohrmann, S. Moe, In *2018 7th Electronic System-Integration Technology Conference, ESTC 2018 - Proceedings*; IEEE, 2018; pp. 1–9.
[77] G. H. Haertling, *J. Am. Ceram. Soc.* **1999**, *82*, 797.
[78] K. G. Brooks, I. M. Reaney, R. Klissurska, Y. Huang, N. Setter, *J. Mater. Res.* **1994**, *9*, 2540.
[79] X. J. Meng, J. G. Cheng, J. L. Sun, H. J. Ye, S. L. Guo, J. H. Chu, *J. Cryst. Growth* **2000**, *220*, 100.
[80] W. Wu, Y. Wang, G. K. H. Pang, K. H. Wong, C. L. Choy, *Appl. Phys. Lett.* **2004**, *85*, 1583.
[81] K. Aoki, Y. Fukuda, K. Numata, A. Nishimura, *Jpn. J. Appl. Phys.* **1995**, *34*, 192.
[82] P. Muralt, T. Maeder, L. Sagalowicz, S. Hiboux, S. Scalese, D. Naumovic, R. G. Agostino, N. Xanthopoulos, H. J. Mathieu, L. Patthey, E. L. Bullock, *J. Appl. Phys.* **1998**, *83*, 3835.
[83] P. Muralt, *J. Appl. Phys.* **2006**, *100*, 051605.
[84] M. Grossmann, O. Lohse, D. Bolten, U. Boettger, T. Schneller, R. Waser, *J. Appl. Phys.* **2002**, *92*, 2680.
[85] M. Grossmann, O. Lohse, D. Bolten, U. Boettger, T. Schneller, R. Waser, *Appl. Phys. Lett.* **2002**, *80*, 1427.
[86] D. Dimos, W. L. Warren, M. B. Sinclair, B. A. Tuttle, R. W. Schwartz, *J. Appl. Phys.* **1994**, *76*, 4305.
[87] K. B. Lee, S. Tirumala, S. B. Desu, S. Tirumala, *Appl. Phys. Lett.* **1999**, *74*, 1484.
[88] D. C. Kim, W. J. Lee, *Japanese J. Appl. Physics, Part 1 Regul. Pap. Short Notes Rev. Pap.* **2002**, *41*, 1470.
[89] J.-W. Lee, C.-S. Park, M. Kim, H.-E. Kim, *J. Am. Ceram. Soc.* **2007**, *90*, 1077.
[90] H. Nazeer, M. D. Nguyen, G. Rijnders, L. Abelmann, Sardan Sukas, *Microelectron. Eng.* **2016**, *161*, 56.
[91] M. A. Dubois, P. Muralt, *J. Appl. Phys.* **2001**, *89*, 6389.
[92] R. Steenwelle, Strain and composition effects in epitaxial PZT thin film, University of Twente, 2012.
[93] K. Coleman, J. Walker, T. Beechem, S. Trolier-McKinstry, *J. Appl. Phys.* **2019**, *126*, 034101.
[94] H. G. Yeo, Mechanical Energy Harvesters Utilizing {001} Textured PZT Films on Flexible Metal Foils, The Pennsylvania State University, 2017.
[95] H. N. Lee, S. M. Nakhmanson, M. F. Chisholm, H. M. Christen, K. M. Rabe, D. Vanderbilt, *Phys. Rev. Lett.* **2007**, *98*, 45.
[96] M. D. Nguyen, E. Houwman, M. Dekkers, D. Schlom, G. Rijnders, *APL Mater.* **2017**, *5*, 0.
[97] S. Onsorynezhad, F. Wang, *Eur. Phys. J. Spec. Top.* **2019**, *228*, 1475.
[98] A. Mazzalai, D. Balma, N. Chidambaram, P. Muralt, L. Colombo, T. Schmitz-Kempen, In *ISAF/IWATMD/PFM 2014*; IEEE, 2014; pp. 1–4.
[99] D. Zheng, M. Luo, J. Swingler, *Sensors Actuators, A Phys.* **2016**, *241*, 197.
[100] G. W. Kyle, V. Malte, H. K. Neamul, K. Barbara, E. D. John, H. S. Florian, *Smart Mater. Struct.* **2017**, *26*, 63001.
[101] P. I. G. and co. KG, Reliability and Lifetime of Multilayer Piezo Actuators. *PI Ceram. Cat.* **2008**.
[102] P. Pertsch, B. Broich, R. Block, S. Richter, E. Hennig, *Development of highly reliable piezo*

multilayer actuators and lifetime tests under DC and AC operating conditions; 2010.
[103] Z. Fan, J. Koruza, J. Rödel, X. Tan, *Acta Mater.* **2018**, *151*, 253.
[104] M. I. Younis, 2011; pp. 401–442.
[105] R. Q. Rudy, L. M. Sanchez, M. Tellers, R. G. Polcawich, In *2015 Transducers - 2015 18th International Conference on Solid-State Sensors, Actuators and Microsystems*; IEEE, 2015; pp. 1315–1317.
[106] M. Grossmann, D. Bolten, O. Lohse, U. Boettger, R. Waser, S. Tiedke, *Appl. Phys. Lett.* **2000**, *77*, 1894.
[107] M. Dekkers, M. Nguyen, N. Hildenbrand, S. Abel, F. Eltes, J. Fompeyrine, P. Wittendorp, *Adv. Mater. - TechConnect Briefs 2017* **2017**, *4*, 5.
[108] J. Wang, C. Salm, E. Houwman, M. Nguyen, J. Schmitz, *Proc. 2016 IEEE Int. Integr. Reliab. Work. IIRW 2016* **2017**, *0*, 65.
[109] Y. Saito, T. Nakamura, K. Nada, H. Sano, In *Japanese Journal of Applied Physics*; 2018; Vol. 57, p. 11UC04.
[110] A. Arab, Q. Feng, *Int. J. Adv. Manuf. Technol.* **2014**, *74*, 1679.
[111] A. E. Islam, *IEEE Trans. Device Mater. Reliab.* **2016**, *16*, 647.
[112] E. Bouyssou, R. Jérisian, N. Cézac, P. Leduc, G. Guégan, C. Anceau, In *Materials Science and Engineering B: Solid-State Materials for Advanced Technology*; Elsevier, 2005; Vol. 118, pp. 28–33.
[113] J. Munir, Q. Ain, H. J. Lee, Reliability issue related to dielectric charging in capacitive micromachined ultrasonic transducers: A review. *Microelectron. Reliab.* **2019**, *92*, 155–167.
[114] L. W. Li, X. Sun, J. X. Li, L. J. Qiao, Y. J. Su, W. Y. Chu, *Appl. Surf. Sci.* **2009**, *255*, 7841.
[115] P. Bintachitt, P. Suaprasert, P. Aungkavattana, *Integr. Ferroelectr.* **2016**, *175*, 44.
[116] L. Andrejs, H. Oßmer, G. Friedbacher, J. Bernardi, A. Limbeck, J. Fleig, *Solid State Ionics* **2013**, *244*, 5.
[117] Y. C. Han, E. G. Jeong, H. Kim, S. Kwon, H. G. Im, B. S. Bae, K. C. Choi, *RSC Adv.* **2016**, *6*, 40835.
[118] N. Thejo Kalyani, S. J. Dhoble, *Renew. Sustain. Energy Rev.* **2015**, *44*, 319.
[119] D. C. Miller, R. R. Foster, S. H. Jen, J. A. Bertrand, S. J. Cunningham, A. S. Morris, Y. C. Lee, S. M. George, M. L. Dunn, *Sensors Actuators, A Phys.* **2010**, *164*, 58.
[120] H. A. C. Tilmans, J. De Coster, P. Helin, V. Cherman, A. Jourdain, P. De Moor, B. Vandevelde, N. P. Pham, J. Zekry, A. Witvrouw, I. De Wolf, *Microelectron. Reliab.* **2012**, *52*, 2228.
[121] D. Zheng, J. Swingler, P. Weaver, *Sensors Actuators A Phys.* **2010**, *158*, 106.
[122] D. Zheng, J. Swingler, P. M. Weaver, *Sensors Actuators, A Phys.* **2011**, *167*, 19.
[123] I. P. Lipscomb, P. M. Weaver, J. Swingler, J. W. McBride, *J. Electroceramics* **2009**, *23*, 72.
[124] I. P. Lipscomb, P. M. Weaver, J. Swingler, J. W. McBride, *Sensors Actuators, A Phys.* **2009**, *151*, 179.
[125] P. M. Weaver, M. G. Cain, M. Stewart, A. Anson, J. Franks, I. P. Lipscomb, J. W. McBride, D. Zheng, J. Swingler, *Smart Mater. Struct.* **2012**, *21*.
[126] M. Goldman, A. Goldman, J. Gatellet, *Ieee* **1995**, *142*, 11.
[127] Y. Wang, W. Chen, A. E. Pedigo, J. P. Koppes, 1.
[128] W. P. Chen, X. F. Zhu, Z. J. Shen, J. Q. Sun, J. Shi, X. G. Qiu, Y. Wang, H. L. W. Chan, *J. Mater. Sci.* **2007**, *42*, 2524.
[129] H. Y. Huang, W. Y. Chu, Y. J. Su, K. W. Gao, J. X. Li, L. J. Qiao, *J. Am. Ceram. Soc.* **2007**, *90*, 2062.
[130] H.-Y. Huang, Y.-J. Su, L.-J. Qiao, In *Ferroelectrics - Physical Effects*; InTech, 2011.
[131] H. Y. Huang, W. Y. Chu, Y. J. Su, J. X. Li, L. J. Qiao, S. Q. Shi, *Appl. Phys. Lett.* **2006**, *89*, 10.
[132] M. Wu, H. Huang, W. Chu, L. Guo, L. Qiao, J. Xu, **2010**, *3*, 9955.
[133] J. L. Cao, L. T. Li, Y. L. Wang, J. Q. Zhao, Z. L. Gui, *J. Mater. Sci.* **2002**, *37*, 3225.
[134] T. S. Bjørheim, **2012**.
[135] S. Brunauer, P. H. Emmett, E. Teller, *J. Am. Chem. Soc.* **1938**, *60*, 309.
[136] S. Stub, E. Vøllestad, T. Norby, *J. Mater. Chem. A* **2018**, *6*, 8265.
[137] S. Ø. Stub, K. Thorshaug, P. M. Rørvik, T. Norby, E. Vøllestad, *Phys. Chem. Chem. Phys.* **2018**,

20, 15653.
[138] W. P. Chen, Y. Wang, J. Y. Dai, S. G. Lu, X. X. Wang, P. F. Lee, H. L. W. Chan, C. L. Choy, *Appl. Phys. Lett.* **2004**, *84*, 103.
[139] J. D. Baniecki, J. S. Cross, M. Tsukada, J. Watanabe, *Appl. Phys. Lett.* **2002**, *81*, 3837.
[140] F. Messerschmitt, M. Kubicek, J. L. M. Rupp, *Adv. Funct. Mater.* **2015**, *25*, 5117.
[141] N. M. Martin, J. Nilsson, M. Skoglundh, E. C. Adams, X. Wang, G. Smedler, A. Raj, D. Thompsett, G. Agostini, S. Carlson, K. Norén, P.-A. Carlsson, *Catal. Struct. React.* **2017**, *3*, 24.
[142] T. Shinagawa, A. T. Garcia-Esparza, K. Takanabe, *Sci. Rep.* **2015**, *5*, 1.
[143] V. I. Birss, *J. Electrochem. Soc.* **1986**, *133*, 1621.
[144] M. H. Miles, E. A. Klaus, B. P. Gunn, J. R. Locker, W. E. Serafin, S. Srinivasan, *Electrochim. Acta* **1978**, *23*, 521.
[145] M. Suermann, T. Kiupel, T. J. Schmidt, F. N. Büchi, *J. Electrochem. Soc.* **2017**, *164*, F1187.
[146] M. Grossmann, O. Lohse, T. Schneller, D. Bolten, U. Boettger, J. R. Contreras, H. Kohlstedt, R. Waser, *Integr. Ferroelectr.* **2001**, *37*, 205.
[147] C. Yan, Y. Minglei, Z. Qunying, C. Xiaolong, C. Jinkui, G. Le, *Int. J. Polym. Sci.* **2014**, *2014*.
[148] W. P. Chen, H. L. W. Chan, F. C. H. Yiu, K. M. W. Ng, P. C. K. Liu, *Appl. Phys. Lett.* **2002**, *80*, 3587.
[149] H. Fujisawa, S. Hyodo, K. Jitsui, M. Shimizu, H. Niu, H. Okino, T. Shiosaki, *Integr. Ferroelectr.* **2007**, *21*, 107.
[150] K. Hong, I. K. You, Y. S. Yu, S. K. Lee, *Integr. Ferroelectr.* **1998**, *21*, 511.
[151] M. B. Starr, X. Wang, *Nano Energy* **2014**, *14*, 296.
[152] Y. Zhang, S. Kumar, F. Marken, M. Krasny, E. Roake, S. Eslava, S. Dunn, E. Da Como, C. R. Bowen, *Nano Energy* **2019**, *58*, 183.
[153] M. Ohring, *Materials Science of Thin Films*; Academic Press, 2002.
[154] Z. Wu, J. Zhou, W. Chen, J. Shen, C. Lv, *J. Sol-Gel Sci. Technol.* **2015**, *75*, 551.
[155] A. Ayrikyan, O. Prach, N. H. Khansur, S. Keller, S. Yasui, M. Itoh, O. Sakata, K. Durst, K. G. Webber, *Acta Mater.* **2018**, *148*, 432.
[156] Z. Ma, H. Zhao, W. Liu, L. Ren, *Precis. Eng.* **2016**, *46*, 349.
[157] M. Deluca, R. Bermejo, M. Pletz, M. Wießner, P. Supancic, R. Danzer, *J. Eur. Ceram. Soc.* **2012**, *32*, 4371.
[158] K. Coleman, R. Bermejo, D. Leguillon, S. Trolier-McKinstry, *Acta Mater.* **2019**.
[159] M. Deluca, L. Stoleriu, L. P. Curecheriu, N. Horchidan, A. C. Ianculescu, C. Galassi, L. Mitoseriu, *J. Appl. Phys.* **2012**, *111*, 084102.
[160] M. Deluca, T. Sakashita, G. Pezzotti, *Appl. Phys. Lett.* **2007**, *90*, 051919.
[161] M. Deluca, H. Fukumura, N. Tonari, C. Capiani, N. Hasuike, K. Kisoda, C. Galassi, H. Harima, *J. Raman Spectrosc.* **2011**, *42*, 488.
[162] S. Röhrig, C. Krautgasser, R. Bermejo, J. L. Jones, P. Supancic, M. Deluca, *J. Eur. Ceram. Soc.* **2015**, *35*, 4321.
[163] R. H. T. Wilke, P. J. Moses, P. Jousse, C. Yeager, S. Trolier-McKinstry, *Sensors Actuators, A Phys.* **2012**, *173*, 152.
[164] G. Esteves, M. Wallace, R. Johnson-Wilke, C. M. Fancher, R. H. T. Wilke, S. Trolier-Mckinstry, J. L. Jones, *J. Am. Ceram. Soc.* **2016**, *99*, 1802.
[165] H. Elahi, M. Eugeni, P. Gaudenzi, *Energies* **2018**, *11*, 1850.
[166] L. M. Garten, S. Trolier-Mckinstry, *Appl. Phys. Lett.* **2014**, *105*.
[167] Y. Tsujiura, S. Kawabe, F. Kurokawa, H. Hida, I. Kanno, In *Japanese Journal of Applied Physics*; IOP Publishing, 2015; Vol. 54, p. 10NA04.
[168] R. J. Zednik, A. Varatharajan, M. Oliver, N. Valanoor, P. C. McIntyre, *Adv. Funct. Mater.* **2011**, *21*, 3104.
[169] B. A. Tuttle, J. A. Voigt, T. J. Garino, D. C. Goodnow, R. W. Schwartz, D. L. Lamppa, T. J. Headley, M. O. Eatough, In *ISAF '92: Proceedings of the Eighth IEEE International Symposium on Applications of Ferroelectrics*; IEEE, 2003; pp. 344–348.
[170] D. Das, L. Sanchez, J. Martin, B. Power, S. Isaacson, R. G. Polcawich, I. Chasiotis, *Appl. Phys.*

Lett. **2016**, *109*, 131905.
[171] K. G. Webber, E. Aulbach, T. Key, M. Marsilius, T. Granzow, J. Rödel, *Acta Mater.* **2009**, *57*, 4614.
[172] F. H. Schader, M. Morozov, E. T. Wefring, T. Grande, K. G. Webber, *J. Appl. Phys.* **2015**, *117*.
[173] M. I. Morozov, M. A. Einarsrud, J. R. Tolchard, P. T. Geiger, K. G. Webber, D. Damjanovic, T. Grande, *J. Appl. Phys.* **2015**, *118*, 0.
[174] F. H. Schader, D. Isaia, M. Weber, E. Aulbach, K. G. Webber, *J. Mater. Sci.* **2018**, *53*, 3296.
[175] A. Mazzalai, D. Balma, N. Chidambaram, R. Matloub, P. Muralt, *J. Microelectromechanical Syst.* **2015**, *24*, 831.
[176] S. L. Santos e Lucato, D. C. Lupascu, J. Rödel, *J. Am. Ceram. Soc.* **2004**, *83*, 424.
[177] D. Leguillon, E. Martin, *Int. J. Fract.* **2018**, *209*, 187.
[178] D. Leguillon, J. Li, E. Martin, *Eur. J. Mech. A/Solids* **2017**, *63*, 14.
[179] M. Vögler, T. Fett, J. Rödel, *J. Am. Ceram. Soc.* **2018**, *101*, 5304.
[180] M. Promsawat, M. Deluca, S. Kampoosiri, B. Marungsri, S. Pojprapai, *J. Eur. Ceram. Soc.* **2017**, *37*, 2047.
[181] Y. H. Seo, M. Vögler, D. Isaia, E. Aulbach, J. Rödel, K. G. Webber, *Acta Mater.* **2013**, *61*, 6418.
[182] A. S. Verma, D. Kumar, A. K. Dubey, A review of an innovative concept to increase the toughness of the ceramics by piezoelectric secondary phases. *Ceram. Int.* **2018**, *44*, 16119–16127.
[183] S. Cang, J. Chen, C. Lu, *Adv. Mater. Sci. Eng.* **2020**, *2020*, 6975968.
[184] W. Zhu, B. Akkopru-Akgun, S. Trolier-McKinstry, *Appl. Phys. Lett.* **2017**, *111*.
[185] D. Monteiro Diniz Reis, S. Rzepka, K. Hiller, *Microelectron. Reliab.* **2018**, *88–90*, 835.
[186] T. I. Prokopowicz, A. R. Vaskas, *Tech. Rep.* **1969**, *ECOM-90705*.
[187] W. J. Minford, *IEEE Trans. Components, Hybrids, Manuf. Technol.* **1982**, *5*, 297.
[188] B. S. Rawal, N. H. Chan, In *Proceedings - Electronic Components and Technology Conference*; 1984; pp. 184–188.
[189] W. Zhu, J. I. Yang, S. W. Ko, C. Fragkiadakis, P. Mardilovich, B. Akkopru-akgun, T. Bayer, K. Tsuji, C. A. Randall, M. T. Lanagan, S. Trolier-mckinstry, .
[190] T. J. M. Bayer, J. J. Wang, J. J. Carter, A. Moballegh, J. Baker, D. L. Irving, E. C. Dickey, L. Q. Chen, C. A. Randall, *Acta Mater.* **2016**, *117*, 252.
[191] Russell Alan Maier, TRANSIENT DYNAMICS OF OXYGEN VACANCIES AND DEFECT COMPLEXES IN THE PEROVSKITE OXIDE STRUCTURE, The Pennsylvania State University, 2014.
[192] D. Monteiro, D. Reis, R. B. Gmbh, S. Rzepka, K. Hiller, *Int. Symp. Appl. Ferroelectr. 2019 IEEE.* **2019**.
[193] J. I. Yang, RELIABILITY AND AGING IN PATTERNED Pb(Zr0.52Ti0.48)O3 FILMS, The Pennsylvania State University, 2016.
[194] S. W. Ko, W. Zhu, C. Fragkiadakis, T. Borman, K. Wang, P. Mardilovich, S. Trolier-McKinstry, *J. Am. Ceram. Soc.* **2019**, *102*, 1211.
[195] T. M. Ræder, **2015**.
[196] M. Grossmann, O. Lohse, D. Bolten, U. Boettger, T. Schneller, R. Waser, *J. Appl. Phys.* **2002**, *92*, 2680.
[197] M. Grossmann, O. Lohse, D. Bolten, U. Boettger, R. Waser, *J. Appl. Phys.* **2002**, *92*, 2688.
[198] B. Akkopru-Akgun, W. Zhu, M. T. Lanagan, S. Trolier-McKinstry, *J. Am. Ceram. Soc.* **2019**, 1.
[199] C. H. Nguyen, R. Nigon, T. M. Raeder, U. Hanke, E. Halvorsen, P. Muralt, *J. Phys. D. Appl. Phys.* **2018**, *51*, 175303.
[200] R. Nigon, T. M. Raeder, P. Muralt, *J. Appl. Phys.* **2017**, *121*, 204101.
[201] B. Akkopru-Akgun, W. Zhu, C. A. Randall, M. T. Lanagan, S. Trolier-Mckinstry, *APL Mater.* **2019**, *7*, 120901.

Chapter 3

Design, fabrication and characterization of piezoMEMS

This chapter presents the design, fabrication, and characterization of the piezoMEMS structures and devices studied here. First, the general methodology used for fabricating structures and devices is presented. Undoped and Ba-doped PZT deposited on 6" platinized SOI-wafers are chosen as the material systems, and all fabrication-processes have been carried out in the cleanroom-facilities of SINTEF MiNaLab and Penn State University. The developed experimental setup and designed test-structures are then described. Finally, the techniques used for characterizing piezoelectric, ferroelectric, reliability, and lifetime of the test-structures and devices are discussed. The techniques applied have been used and developed in collaboration with the Trolier-McKinstry group at Penn State University, Pennsylvania, USA.

3.1 PiezoMEMS structures and devices

The fabrication-technique controls, to a large extent, the physical and chemical properties of piezoMEMS-devices. High-quality piezoelectric thin-films are fabricated using various physical[1] or chemical[2] deposition techniques, including magnetron sputtering[3], pulsed laser deposition (PLD)[4] and chemical solution deposition (CSD)[5]. Devices consist of structured metal-piezoelectric-metal thin-film stacks grown on silicon-on-insulator (SOI) wafers[6]. (001)-oriented $LaNiO_3$ grown on (111)-oriented Pt is a well-suited bottom electrode system and is therefore chosen as a template for this work. All films are grown by either large-scale PLD[7] or CSD. In this section, fabrication-processes and techniques utilized in this thesis are presented. The reader is otherwise directed to literature for extensive information on MEMS-design and fabrication[8–10].

3.1.1 Fabrication of thin-film piezoMEMS

Silicon is a semiconductor with good electrical, mechanical, and thermal properties, widely adapted for piezoMEMS-devices today[11,12]. Single crystal silicon is cut into thin wafers and polished before proceeding through numerous micromachining processes. Surface-micromachining is the process of depositing layers onto the wafer, while bulk-micromachining is structuring the wafer through etching-techniques. For the latter, a buried oxide (BOX)-layer is used as an etch-stop for defining the thickness of specific parts of the device. Here, this so-called device-thickness is either 5 or 8 µm. Starting from the SOI-wafer, device-fabrication can be roughly divided into four essential processes, as illustrated schematically for the fabrication of the piezoelectric micromirror in Figure 3.1; (i) oxidation, (ii) film deposition, (iii) patterning and (iv) backside etching [13]. These will be discussed in the following.

(i) Oxidation

A $\mathrm{SiO_2}$-layer is grown on a polished Silicon wafer by heating the wafer to $800 - 1200^oC$ in a tube-furnace containing an oxygen atmosphere. The oxide-layer electrically isolate the functional stack from

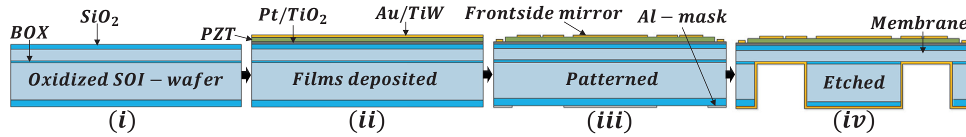

Figure 3.1: Processing steps used to fabricate piezoMEMS-devices and structures, here exemplified for the fabrication of the piezoelectric micromirror for this work. The SOI-wafer is oxidized (i) before surface-micromachining by depositing (ii) and patterning (iii) the metal-piezoelectric-metal stack. Bulk micromachining by etching (iv) the silicon substrate is used for structuring the final device.

the SOI-wafer and controls the total stress of the final structure. In this work, an oxide thickness of 1.6 µm was used.

(ii) Film deposition

A 10 nm Ti or $\mathrm{TiO_2}$ adhesion-layer is sputter-deposited between $\mathrm{SiO_2}$ and the 100 nm (111)-oriented Pt bottom-electrode. A 10 nm (001)-oriented conductive $\mathrm{LaNiO_3}$ layer is deposited as an oxide bottom electrode. PZT is then deposited by either PLD or CSD with a thickness of 1-2 µm. In PLD, a target material is ablated into a plasma plume using a high-power pulsed KrF excimer laser and directed towards the substrate. The neutral and high-energy ad-atoms in the plasma absorbs and diffuses along the substrate surface to deposit a thin-film. The PZT-layer is deposited at $650^{\mathrm{o}}\mathrm{C}$ directly after the $\mathrm{LaNiO_3}$-layer without breaking the vacuum. In CSD, a precursor solution is spun onto the Pt-electrode at 2000-3000 rpm and pyrolyzed on a hot-plate of $200 - 300^{\mathrm{o}}\mathrm{C}$. The PZT is then crystallized using rapid-thermal annealing at $500 - 700^{\mathrm{o}}\mathrm{C}$ to create a 250 nm thick PZT-film. This process is repeated until the desired thickness is achieved. On top of the PZT-layer, an additional adhesion-layer, Ti or Ti with 10 wt% W, is sputtered onto PZT before depositing the 100-250 nm Au or Pt top electrode.

(iii) Patterning

After depositing the piezoelectric stack, the top electrodes are patterned using a lift-off process. Before depositing the final adhesion-layer and top electrode, a photoresist-layer is spun onto the PZT-surface and baked on a hot-plate at $130^{\mathrm{o}}\mathrm{C}$ for 90 s. After curing, the resist is UV-irradiated through a mask and the exposed areas dissolved in a solution. The electrode is deposited over the resist-pattern, and the undesired areas "lifted off" by dissolving the remaining resist in an acetone-bath. Thus, only selected areas on the surface are electroded.

(iv) Backside etching and dicing

After front-side patterning, an aluminum shadow-mask is deposited on the backside of the silicon wafer. The mask is patterned, and the selected areas etched away using a Bosch deep reactive ion etching (DRIE) process. A chamber with a $\mathrm{SF_4}$-atmosphere is used to etch the silicon substrate. An electric field creates a plasma, and ions are accelerated towards the substrate, and selectively etches away silicon. Between each consecutive etching cycle, a $\mathrm{C_4F_8}$ protective layer is added to protect the sidewalls, to avoid sidewall-damage during etching. Due to the directionality of the electric field, silicon is etched anisotropically through the mask, enabling the definition of structures in the bulk of the wafer, i.e. bulk micromachining. As the final step, the processed wafer is placed on a tape and diced using a diamond saw.

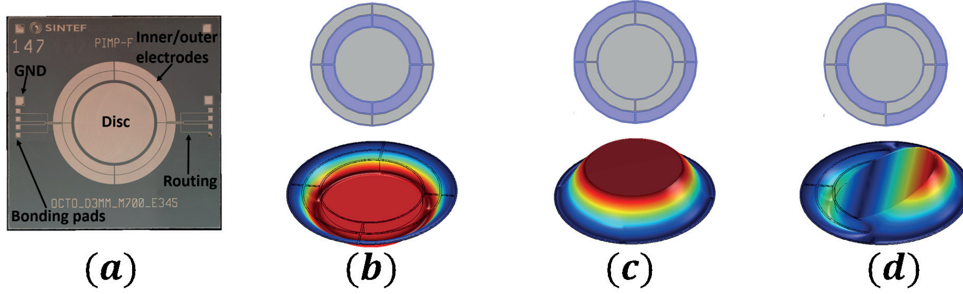

Figure 3.2: Top view microscopy image of the as-fabricated micromirror from Figure (iv) is shown in (a). The bonding pads are placed along the periphery of the die and routed to the membrane-electrodes. The top and bottom electrode are both contacted on the front side of the die. (b)-(d) shows the working principle of the piezoelectric micromirror schematically. Actuating the inner (b) and outer (c) electrode ring pushes the center disc downwards and upwards. A tip-tilt motion (d), is achieved by asymmetric actuation of the inner and outer ring on opposite sides of the center-disc.

3.1.2 Micromirror geometry

A side-view schematic of the as-fabricated piezoelectric micromirror is shown in Figure 3.1 (iv). A top-view micrograph and illustration of its working principles are shown schematically in Figure 3.2 $(a) - (d)$. The device is comprised of a rigid 400 µm thick silicon-disc suspended on an 8 µm thick structured membrane surrounded by eight evenly distributed electrodes. The membrane-electrodes are routed to bonding pads on the periphery of the micromirror frame. When an electric field is applied, the in-plane piezoelectric stress, σ_x (eq. 2.4), bends the membrane structure with a bending moment, M_i, linear to the thickness of the piezoelectric film, t_f, and the distance to the neutral plane of the device, z_P[14]:

$$M_i = -\sigma_x t_f z_P \tag{3.1}$$

As shown in Figure 3.2 (b), applying a field across all the inner electrodes actuates the device by pushing the disc downwards. Applying a field across the outer electrodes pushes the disc upwards as shown in (c), such that a tip-tilt motion can be achieved and accurately controlled through asymmetric actuation of the inner and outer electrodes as shown in (d). In this was various tilt-positions and motions of the mirror plane can be controlled and used to reflect, resonate and guide electromagnetic waves. This allows for applications within gas-detection and optical communication, as demonstrated by the Norwegian company, Tunable[15]. For the micromirrors fabricated in this work, a maximum angular deflection of $\pm 0.6^o$ was achieved by simultaneously actuating the two inner and two outer electrodes on opposite sides of the device. This corresponds to a maximum bending of about 15 µm from the neutral axis. The maximum deflection condition was used throughout the reliability and lifetime-testing of the device in this work.

3.2 Experimental setup and test structure design

In real-life operating conditions, piezoMEMS-devices experience a combination of additional electrical, chemical, mechanical, and thermal stressors. The dominating failure-mechanism is often unique to each device-design and requires customized experimental-setups for investigating the impact of the various stress-factors on performance[16–19]. High accuracy equipment for characterizing

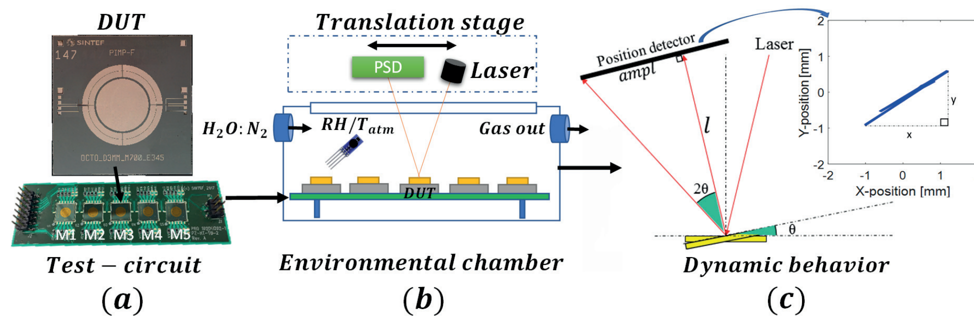

Figure 3.3: Schematic of the developed experimental design for reliability and lifetime testing. The device is wire-bonded to a MEMS test-circuit with an integrated heater, (*a*), which is then placed inside a 3D-printable environmental chamber with ambient control, (b). The humidity and temperature are controlled using k-type thermocouples and humidity-sensors, and all electronics are kept outside the chamber on a micrometer-stage allowing for characterizing multiple devices in each experimental condition. An optical window on top of the chamber allows for electromechanical characterization by reflecting a laser of each chip onto a position sensitive device (PSD), as illustrated in (c).

piezoelectric[20–23], dielectric[24,25], electromechanical[18,20,26,27] and ferroelectric[28] properties have already been developed. In this section, the development of the experimental setup, its integration into high accuracy characterization-equipment, and design of test-structures will be presented.

3.2.1 Experimental setup

The chosen strategy was to develop an experimental set-up that allowed for utilizing already available instrumentation for characterizing structures and devices as they operated in controlled ambient conditions. The setup was designed as a versatile “ad on” module, since standards, sample-mounting, contacting, etc. varies between types of equipment. To this purpose, a compact 3D-printable environmental chamber was designed so that it could be easily retrofitted to available characterization-equipment. A schematic of the basic design is shown in Figure 3.3. A polyimide MEMS test-circuit card with five $8\text{x}8\ \text{mm}^2$ slots and an integrated heater going up to 200°C, was designed and fabricated. Each slot was gold-plated to increase thermal conduction to the device-under-test (DUT). The circuit was designed for contacting using either needle-probing, wire-bonding, or surface-mounted connectors. Wire-bonding to bonding pads along the periphery of the die was most frequently used for parallel-testing of devices. The test-circuit containing up to five individual dies was locked in place by magnets inside the environmental chamber as shown in Figure 3.3 (b). The temperature of the test device and ambient, was measured using a k-type thermocouple integrated into the test circuit. Controlled ambient humidity was enabled by bubbling N_2 through a DI-water container and flowing the $H_2O: N_2$-mixture through the chamber and measured using a high-precision HYT271 humidity-sensor[29]. The test-conditions were stabilized through an external feedback loop, regulated by external PID -and flow-controllers. Temperature and humidity-conditions were controlled and recorded using a combined Raspberry Pi 3B+ and LabView based platform based on a sbRIO9627 single-board computers. An optical window on top of the chamber allowed for reflecting a laser off the structure or device onto a position sensitive detector for electromechanical characterization during the experiment, as shown in Figure 3.3 (c). Both the laser and a position-detector were mounted onto

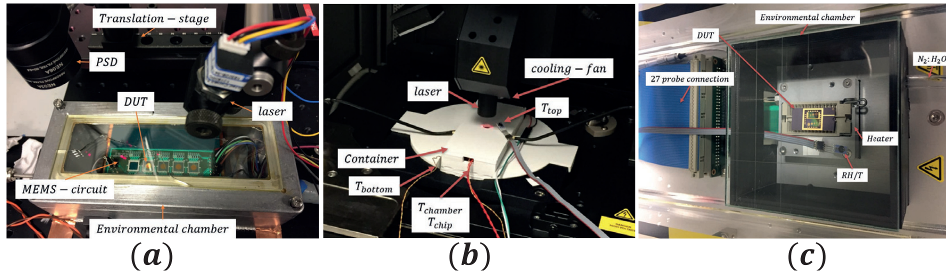

Figure 3.4: Examples of retrofitted experimental setups enabling electromechanical characterization, (*a*), double beam laser interferometry, (b) and accelerated lifetime-measurements, (c), with ambient control.

an external micrometer-stage and scanned across all devices throughout the experiments. This allowed for individual characterization of each device in controlled ambient and temperature conditions. Keeping all electronic components outside the environmental chamber allowed for simple retrofitting of the set-up to the relevant test-equipment. Examples of retrofitted experimental-setups for electromechanical characterization, double-beam laser interferometry (DBLI), and accelerated lifetime testing are shown in Figure 3.4 (a), (b) and (c) respectively.

3.2.2 Design of PZT-based test-structures

A set of initial lifetime-measurements in air and 90 % relative humidity (RH) at $25 - 175^{\mathrm{o}}\mathrm{C}$ were conducted on as-made piezoelectric micromirrors to identify the critical flaws and dominating causes of failure of devices under simulated realistic and harsh operating conditions. The initial temperature-humidity-bias characteristics are discussed in Manuscript (I) in which the ambient humidity was found to have the largest impact on device-performance. The electrode-routings and bonding-pads were the critical flaws of the system and therefore used as a basis for designing simple test-structures for humidity-related studies. The mask-layouts for the device and test-structures are shown in Figure 3.5 (*a*)-(c) and backside wafer-view and fabricated structures in (d). A structure-purpose summary is provided in Table 3.1. Each mask-set contained 186 dies, each with up to 12 test-structures. For each set of 6" wafers, a 1 µm and 2 µm thick undoped or Ba-doped PZT films were deposited by CSD and PLD respectively. 10-100 µm wide lines simulated the effect of varying routing-widths and circular and square pads with an area of 0.002-3.14 mm^2 simulated the effect of pad-size. The lines and pads were utilized for the studies conducted in Manuscript (II)-(II). Pads, clamped, released and suspended on

Table 3.1: Purpose of fabricated structures relevant for piezoMEMS-reliability

Purpose	Device	Lines	Diaphragms	Pads/islands	Cantilevers
Identify/study failure type	X	X			
Electromechanical response	X		X		
Thin-film encapsulation strategies	X				
Effects of film stress and stress-alleviation			X	X	X
Investigate diaphragm-dynamics			X		
Aging and low-field operation			X	X	
Piezoelectric properties of film			X	X	X
Electrochemically driven degradation	X	X		X	
Size and declamping effects				X	
Surface-currents		X		X	

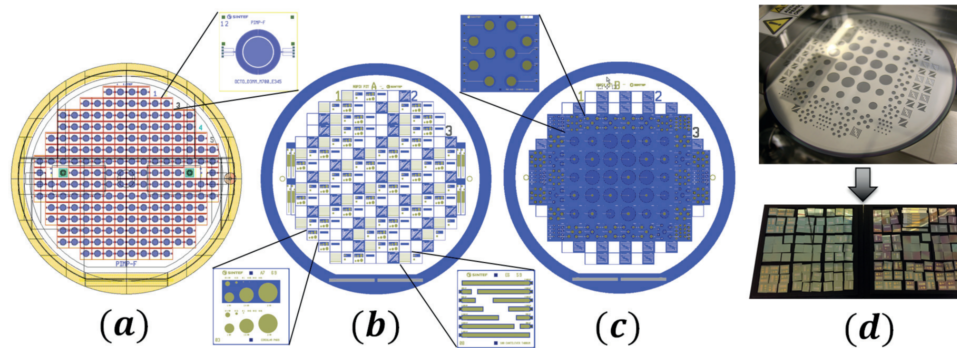

Figure 3.5: Final mask-layout for piezoelectric micromirrors (a), cantilevers, lines and pads (b), and diaphragm-structures (c). Close up of devices and structures are shown in the insets. An example-wafer under backside DRIE and finished structures after dicing is shown in (d).

diaphragms were fabricated with the intention of studying self-heating effects, stress-alleviation and piezoelectric nonlinearities (Rayleigh-dynamics). The electrode covered from 10-100% of the diaphragm to examine the effect of stress-alleviation on the functionality. The cantilevers had a width of 100 µm, a length of 400-8400 µm and a thickness of 5 and 400 µm, designed to satisfy the Kanno[22,30] and Mazzalai[21] equations for comparability with similar literature-reports[1]. The 1D-geometry also simplifies the study of crack initiation and propagation for stress-related studies[26,31–34]. All structures were routed to bonding-pads along the sides of each die, for compatibility with the developed experimental setup.

One wafer of micromirror-devices using 1 µm thick PLD – deposited PZT-films were fabricated for assessing the use of humidity barrier-layers. Atomic layer deposition (ALD) has beneficial attributes in terms of homogeneity over complex structured surfaces for thin coatings[35–37], and were therefore pursued in this work. The devices were encapsulated using 40 nm $\mathrm{Al_2O_3}$ which improved the median time-to-failure (MTTF) as reported in Manuscript (IV).

3.3 Thin-film and device characterization

Ambient stressors will affect both the macroscopic and microscopic properties of thin-films. The nature and origin of the mechanisms governing degradation can be analyzed by comparing the physical, chemical, and functional properties of pristine and degraded samples[38–41]. In this section, the characterization-techniques and methods used in this work will be presented. The reader is directed to literature for more comprehensive reviews of the used methods and instrumentation.

3.3.1 Texture and microstructure

Film orientation was analysed by X-ray diffraction (XRD)[42]. This was done using a Bruker D8 Discovery diffractometer with $\mathrm{CuK\alpha_1}$ radiation of 1.54 Å. An example-scan of a $\theta - 2\theta$ scan showing a 90 % / 10% mixed (001) / (110)-orientation of a 1 µm thick PZT-film is shown in Figure 3.6 (a).

Scanning electron microscopy (SEM) was used to analyse the film's composition, topography, and microstructure[39]. In this technique, a beam of high-energy electrons is scanned across the sample surface and scattered onto a detector. The energy of forward and back-scattered electrons is used to gain topographical information. A SEM cross-section image of a degraded micromirror is shown in Figure 3.6 (b). The energy transferred from the beam into the samples will also excite electrons in the lattice of the sample. As the excited electrons resign to the ground-state, X-rays characteristic for the excited atoms are emitted and can be used for elemental mapping. This is called energy-dispersive X-ray spectroscopy (EDX) and is demonstrated for a humidity-degraded sample in Figure 3.6 (c). The

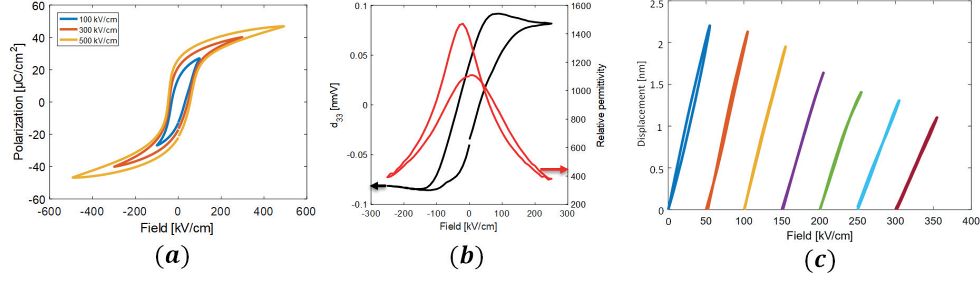

Figure 3.6: The development of a ferroelectric hysteresis with increasing fields is shown in (a). A measurement of the piezoelectric coefficient (black) and permittivity (red) are shown in (b). The corresponding displacement of the structure with an increasing DC offset is shown in (c).

morphology at a sub-µm scale was probed using Atomic force microscopy (AFM) [43,44]. In this technique, topographical information is gained by scanning an atomically sharp tip across the sample surface while measuring the tip-sample interactions. As illustrated in Figure 3.6 (d), sub-µm topographical information was obtained using AFM.

3.3.2 Polarization, permittivity and dielectric loss

The piezoelectric response of MPB-PZT depends on the polarization and permittivity of the PZT film[45,46]. The total leakage through the sample is the sum of the resistive, i_R, capacitive, i_C and the ferroelectric switching, i_F currents: $i_{tot} = i_R + i_C + i_F$. i_F is extracted using dynamic leakage current compensation[47]. The polarization is then found by integrating i_F from t_0 to t_1, i.e. the time for the applied field to completely switch the polarization:

$$P = \frac{1}{A}\int_{t_0}^{t_1} i_F \, dt \left[\frac{C}{m^2}\right] \tag{3.2}$$

where A is the electrode-area. In this work, the P-E curves were measured with a frequency ranging from 10^{-2} to 10^6 Hz, with a typical large-signal amplitude of 50 V. Typical values for a PLD-deposited PZT with an Au/TiW top electrode were $P_R = 24.9 \pm 3.2$ C/m², $P_S = 50.3 \pm 3.6$ C/m² and $E_C = 49.5 \pm 4.2$ kV/cm. P-E loops measured at increasing fields are shown for a 1 µm PLD-deposited Ba-doped $PbZr_{0.4}Ti_{0.6}O_3$ film in Figure 3.6 (a).

The permittivity, ε, provides information about the material's ability to polarize in response to an electric field, and the charged species involved; space-charge, dipolar, ionic, and electronic species[48]. It is found by measuring the sample's capacitance, C:

$$\varepsilon = \frac{C t_f}{\varepsilon_0 A} \tag{3.3}$$

t_f is the film-thickness, and $\varepsilon_0 = 8.85\, x\, 10^{-12}$ the vacuum permittivity. The magnitude of ε depend on the signal amplitude and frequency. In this work, PZT had a permittivity from $1000 - 1500$, as exemplified for Ba-doped $PbZr_{0.4}Ti_{0.6}O_3$ in the red curve of Figure 3.7 (b). Though PZT is a good electrical insulator ($R \sim 10^{12}\ \Omega$), stored charge will never be recovered entirely during the discharging of real materials. The dielectric loss-tangent, $\tan(\delta)$, gives the resulting energy-loss of the capacitor:

$$\tan(\delta) = \frac{G}{2\pi f C} \tag{3.4}$$

where G is the conductance in Siemens, and f is the frequency. The functional stacks used in this work had a typical loss of 0.044 ± 0.009. In the present work a TF ANALYZER 2000 ferroelectric analyzer

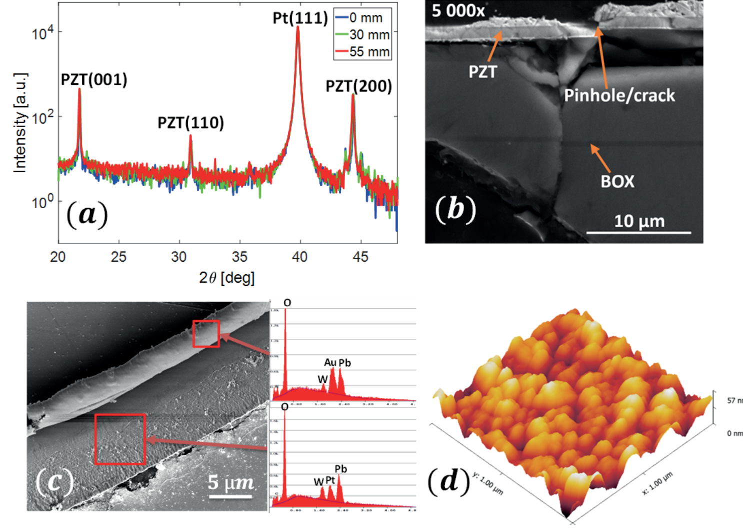

Figure 3.7: Examples of microstructural data. The XRD-scans, (a) show a 1 µm PZT-film with a mixed (001) / (110)-orientation at 0, 30 and 55 mm from the centre of a 6 " wafer. A SEM cross-section is exemplified in (b), and elemental mapping in (c). While SEM-images of post-degraded samples show macroscopic cracks, material droplets and pinholes little sub-µm difference in the topography between pristine and degraded samples was found by AFM, (d).

(AixACCT Systems), was used for dielectric, ferroelectric, leakage, loss and time-dependent property-measurements[28].

3.3.3 Piezoelectric properties

The piezoelectric properties can be calculated from phenomenology using the polarization, permittivity, and electrostrictive coefficients, as exemplified for the tetragonal phase in eq. 2.11. However, the mechanical boundary conditions of structures and devices cause the actual piezoelectric coefficients to deviate from the phenomenological values[49,50]. Hence, the functional properties of the film, e.g. $d_{33,f}$ and $e_{31,f}$, should be measured directly. In this work, $d_{33,f}$ was measured using an AixACCT double-beam laser-interferometer[51,52]. The operation principle is based on the Michelson interferometer, in which a coherent laser beam is reflected from the sample-surface to interfere with a reference beam. Small changes in the beams travel-distance induce large shifts in the resulting interference-pattern, such that deflection-resolution in the order of Å can be measured. The out-of-plane expansion of the piezoelectric layer in response to the field is separated out by reflecting an extra beam from the backside of the sample, such that only the change in sample thickness, Δt_f, is measured[53]. $d_{33,f}$ is thereafter calculated using:

$$d_{33,f} = \frac{\Delta U_D \lambda}{2\pi(U_{max} - U_{min})} \left[\frac{m}{V}\right] \tag{3.5}$$

Here λ is the wavelength of the incident beam, and the photodetector-voltages, $\Delta \mathrm{U_D}$, $\mathrm{U_{max}}$ and $\mathrm{U_{min}}$ are proportional to the beam-intensity at the photodiode. A $d_{33,f}$-measurement of a clamped $\mathrm{A} = 0.8\ \mathrm{mm}^2$ circular pad with 1 µm Ba-doped $PbZr_{0.4}Ti_{0.6}O_3$ is shown in the black curve of Figure 3.7 (b). The corresponding displacement as a function of DC offset is shown in Figure 3.7 (f). As the polarization saturates with increasing, so does d_{33f} and the achieved displacement. For the current film, $\mathrm{d_{33,f}} = 90\ [\mathrm{pm/V}]$.

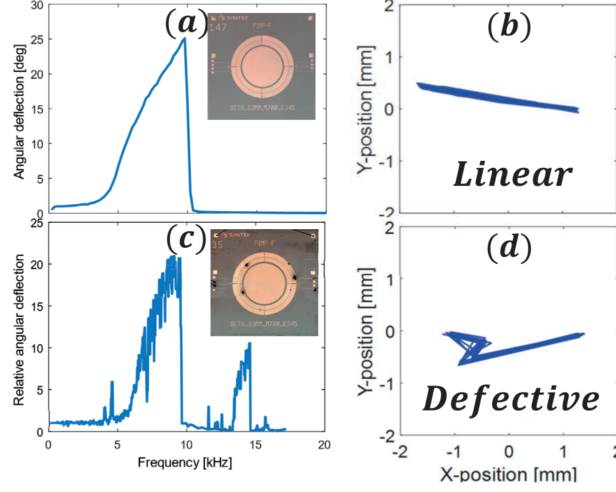

Figure 3.8: Frequency-scan and laser-trace examples of a functional, (a)-(b), and humidity-degraded, (c)-(d) micro-mirror. Electrothermal breakdown-events typically resulted in distorted

Measuring the in-plane converse coefficient, $e_{31,f}$, often requires the design of special test-structures or measurement-setups[21,22]. In this work, $e_{31,f}$, was found using wafer-bending and bonded strain-gauges to measure the charge generated in response to an applied strain:

$$e_{31,f} = \frac{Q}{A(x_1 + x_2)} \left[\frac{N}{Vm}\right] \tag{3.6}$$

Here Q is the charge and x_i the in-plane strain in direction i. Each sample was periodically strained with a sinusoidal signal with a frequency of 4 Hz, and the collected charge per period averaged over three hours. This was done using a setup reported elsewhere[20]. The obtained $e_{31,f}$-values for the films used in this work ranged from 12-14 [N/Vm].

3.3.4 Residual film stress

Information regarding the stress-state of the deposited film is essential for the operating range and measured electromechanical response of the structures and devices. As discussed in section 2.3.2, the film will experience residual stress opposite to the substrate and cause a bending. When stress-transfer is from the film to the substrate, the film is under tension if the substrate bends upwards, and under compression if the substrate bends downwards. When the substrate is much thicker than the film, the residual stress can be approximated using the Stoney's equation, knowing the substrate thickness, t_S, Youngs moduli, E_S and Poisson's ratio, ν_S [39]:

$$\sigma_R = \frac{E_S t_S^2}{6(1 - \nu_S)t_f} \left(\frac{1}{R} - \frac{1}{R_0}\right) \tag{3.7}$$

Here R_0 is the radius of curvature of the wafer before the film was deposited and R is the radius of curvature after depositing the film. t_f is the film thickness. R was here obtained by measuring the radius of curvature of wafers containing the entire film stack using white light interferometry[54,55]. R_0 was then obtained by wet-etching away the top thin-film, and re-measure the radius of curvature. This was repeated for each consecutive layer, to yield the associated film stress. More details can be found in the supplementary information of manuscript (IV). In this work, the average post-deposition stress was ~250 MPa for the PLD-deposited films and ~150 MPa for the CSD-deposited films.

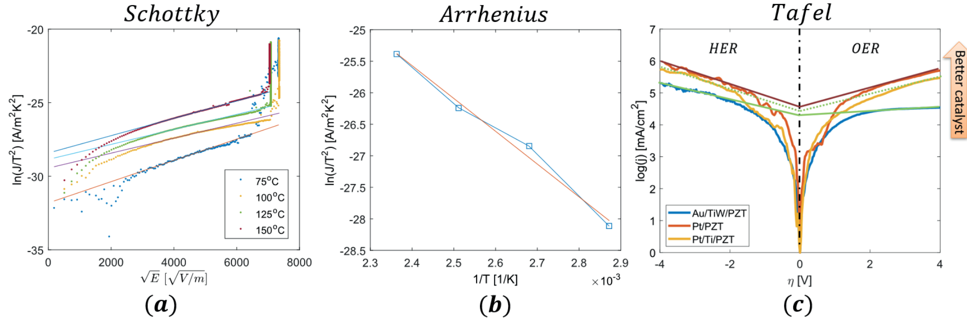

Figure 3.9: Characterization of electrode-properties relevant for thin-film reliability in realistic environments. The conduction-mechanisms and interface barrier-properties can be found by fitting I-V data taken at different temperatures to the relevant conduction-equation, (a), and the Arrhenius equation, (b). The electrochemical activity can be found by evaluating the Tafel-curves, (c).

3.3.5 Electromechanical response

The electromechanical response of the devices was characterized by reflecting a laser off the micromirrors centre disc, through the integrated optical window and onto a position sensitive device (PSD), as illustrated in Figure 3.3 (c). Since the angular deflection was always below 1°, the small-angle approximation, $tan(\theta) \approx \theta$, was used to calculate the angular deflection, θ, based on the recorded x and y laser-trace positions:

$$\theta \approx \tan(\theta) = \sqrt{\frac{x^2 + y^2}{2l}}[rad] \tag{3.8}$$

$l = 100$ mm is the distance from the device to the PSD. The laser trace and the angular deflection was further used for describing the effect of degradation on the device's electromechanical response. Characteristic frequency-scans of a micromirror in the pristine state and after degradation in humid conditions for $1x10^7$ unipolar cycles are shown in Figure 3.8 (a), (c). The insets show images of the devices, and laser-traces of the pristine and degraded state are provided in Figure 3.8 (b), (d). Degradation imposed significant changes in the dynamical behavior of the device during the experiment, not necessarily reflected in the amplitude vs time or current vs time measurements. Both the laser-trace and angular deflection were therefore recorded throughout the experiments. This is further discussed in manuscript (IV).

3.3.6 Electrode interfaces

Generally, the Schottky-barrier prevents charge-carriers from being injected from the electrode into the samples when a field is applied, and the conduction can be Schottky-emission, Poole-Frenkel emission, Ohmic, or Space-charge limited.[56–58] The conduction mechanism can be determined by measuring the I-V-characteristics at different temperatures and refit the measured data to the conduction -and Arrhenius ($k = Ke^{\frac{E_A}{k_B T}}$) equations. This is exemplified for Schottky and Arrhenius equations from this work in Figure 3.9 (a), (b). For thin-film PZT, Schottky and Poole-Frenkel emission are the most common conduction mechanisms and can be calculated by:

$$\ln\left(\frac{J_{Sch}}{T^2}\right) = \ln(A^{**}) - \frac{q\Phi_B}{k_B T} + \frac{q\sqrt{\frac{qE}{4\varepsilon_0 \varepsilon_r \pi}}}{k_B T} \tag{3.9}$$

$$\ln\left(\frac{J_{PF}}{E}\right) = \ln(C_T) - \frac{q\Phi_B}{k_B T} + \frac{q\sqrt{\frac{qE}{\varepsilon_0 \varepsilon_r \pi}}}{k_B T} \tag{3.10}$$

Here J is the current density, E the electric field, T the temperature, q the elementary charge, k_B the Boltzmann-constant, Φ_B the barrier height, A^{**} the Richardson's constant, C_T a constant, ε_0 the vacuum and ε_r the relative permittivity. A^{**}, C_T and Φ_B is found by linear fitting of $\ln\left(\frac{J}{T^2}\right)$ vs. $\frac{1}{T}$ and $\ln\left(\frac{J}{E}\right)$ vs. $\sqrt{E}$, using either the slope of the curves or the intersect with the y-axis. Cases exist in which good fits are obtained simultaneously for multiple equations. An additional equation relating the parameters from eq. (1) and (2) to the refractive-index, n_{PZT}, of PZT is therefore needed to determine the dominant conduction-mechanism:

$$n_{PZT} \approx \frac{0.88}{A^{**}T} \tag{3.11}$$

Reported refractive-index values for PZT are from 2.1-2.5.[59,60] Fits to eq. (3) giving refractive-indexes within this interval indicates the dominating type of conduction. For the present work, I-V measurements were carried out at temperatures from 25 to $150^{\circ}\mathrm{C}$ with a step-size of $0.5\ V$ and a dwell-time (to remove the contributions from capacitive transient currents) at each step of 30 s.

The barrier height can differ significantly at the top and bottom electrode interface, and therefore depends on the polarity of the applied electrical field. It is debated on the main electronic charge-carrier (electrons or holes) being injected across the Schottky-barrier. Hence, only the aggregated effect of both interfaces in response to the applied field is determined from the I-V-measurements. Examples of measured barrier heights in the present work are $\Phi_{Pt}^{+} = 1.02 \pm 0.22$ eV and $\Phi_{Pt}^{-} = 0.77 \pm 0.06$ eV for field up (positive top electrode) and field down (negative top electrode) respectively in undoped PZT deposited by CSD using symmetric Pt top and bottom electrode. A refractive index of $n_{Sch} = 2.41 \pm 0.15$ for the Schottky-fit and $n_{PF} = 4.95 \pm 0.21$ for the Poole-Frenkel fit indicates that the conduction is Schottky-limited. In comparison, barriers of $\Phi_{Au/TiW}^{+} = 0.65 \pm 0.09$ eV and $\Phi_{LNO/Pt}^{-} = 0.25 \pm 0.06$ eV was found for asymmetric $\mathrm{Au/TiW}$ top and $\mathrm{LaNiO_3/Pt}$ bottom electrodes, also Schottky-limited. Pt having the largest Schottky barrier height is consistent with the difference between work-function and affinity, yet the values differ significantly from the theoretical predictions: $\Phi_{Pt} = 1.45$, $\Phi_{Ti} = 1.16$ and $\Phi_{Au} = 1.39$ eV[61–63].

3.3.7 Lifetime measurements

Reliability -and lifetime-testing of structures and devices intended to sustain up to 25 years of continuous operation can be challenging. Means of accelerating lifetime measurements and the use of statistical analysis are therefore necessary to study different degradation-factors "within the lifetime of a Ph.D.-student." Acceleration can, in general, be achieved by increasing the force of the degrading stress factor to be studied under the assumption that the added stress will lead to the same degradation-mechanisms and failure as will be encountered in long term regular operation. Temperature, electrical fields, or the ambient relative humidity are examples of parameters that can be used to accelerate measurements and extrapolate device lifetimes and information related to the

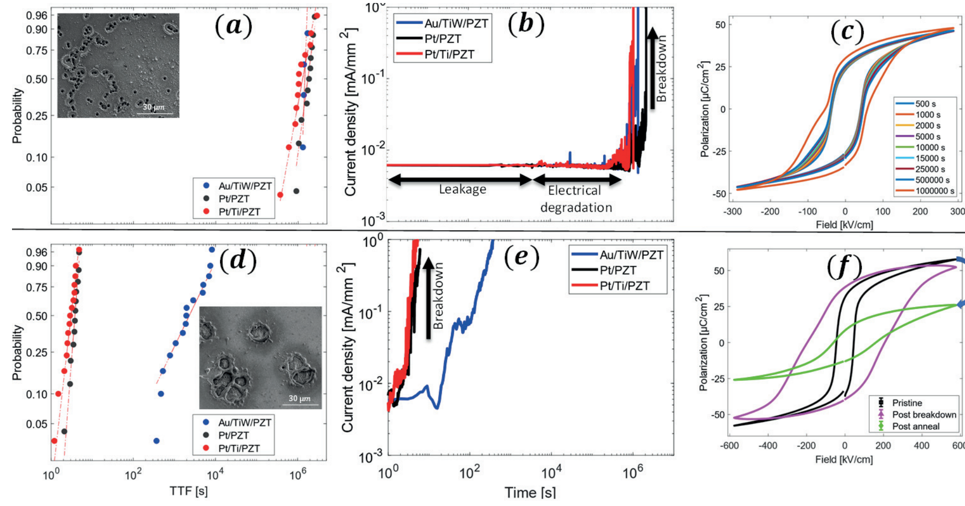

Figure 3.10: Compared measurements for the Au/TiW/PZT, Pt/PZT and Pt/Ti/PZT electrode systems in dry (upper) and humid (lower) ambient conditions. Failure probability is shown in $(a), (d)$, characteristic leakage vs time measurements in $(b), (e)$ and the characteristic evolution of the P-E hysteresis loop during degradation in $(c), (f)$.

governing degradation mechanisms. In this work, humidity and field-acceleration have been used and will be briefly discussed here.

(i) Statistical analysis

The failure probability for a film or device operating under various conditions is described in terms of Weibull-distribution functions[24,27,64]. The cumulative probability-distribution is given by:

$$F(x; \lambda, \beta) = 1 - e^{-\left(\frac{x}{\lambda}\right)^{\beta}} \tag{3.12}$$

Here $F(x; \lambda, \beta)$ is the failure probability, x the measured variable, e.g. time or voltage and λ the reported MTTF known as the scale-parameter. The shape-parameter, β, describes the confidence of the measurement and can be used to address the type of failure-mechanism in the device[65,66]. An example from this work of a cumulative distribution for the Au/TiW/PZT, Pt/PZT, and Pt/Ti/PZT electrode systems operated at 40 VDC in dry (upper) and humid (lower) ambient conditions are shown in Figure 3.10 (a) and (d). In this example, a comparable MTTF was found for all tested electrodes in dry conditions, yet a considerably larger resilience towards degradation in humid condition was found for the Au-based system. Irreversible electrothermal breakdown-events characteristic for time-dependent dielectric breakdown in dry and humid conditions are shown in the insets of Figure 3.10 (a) and (d).

(ii) Voltage acceleration

The electrical field strength accelerates thermodynamically driven processes, including charge injection, movement of ionic species and chemical reaction-rates. Voltage acceleration-factor, N, can be calculated using extended lifetime-models, in which the Eyring/Prokopowicz-Vaskas is often adapted[65,67,68]:

$$\frac{t_1}{t_2} = \left(\frac{V_2}{V_1}\right)^N e^{\frac{E_A}{k_B}\left(\frac{1}{T_1}-\frac{1}{T_2}\right)} \quad (3.13)$$

Here t_i are the characteristic failure times, T_i the temperatures and V_i the applied voltages. The dynamics of degradation in dry and humid conditions for which this model was utilized is exemplified in Figure 3.10, and further discussed in Manuscript (II). Time-dependent dielectric breakdown and evolution of the P-E loops over the course of degradation at 40 V_{DC} are shown for dry conditions in (b), (c), and for humid conditions in (e), (f). Here, the electrode-dependent voltage-acceleration in humid conditions; $N_{Au} = 0.53, N_{Pt} = 2.39$ and $N_{Pt} = 2.01$ were all found to differ significantly from that predicted by a Schottky-based model; $N_{Sch} \sim 1.2$, which indicates a different dominating degradation mechanism than dry conditions. While in dry ambient, degradation is manifested through a leakage, electrical degradation, and breakdown-regime, spontaneous failure is encountered at the same voltage in humid conditions. Apparent differences are also found in the characteristic developments of the P-E loops during degradation, as shown in Figure 3.10 (c) and (f).

(iii) Humidity-acceleration

Accelerating humidity-related degradation is done both by increasing the ambient relative humidity (RH) and the applied electrical field[69,70]. When exceeding 60 % RH adsorbed water molecules from the ambient forms a continuous surface water-layer[71–78]. This accelerated degradation, as shown in manuscript (II)-(IV). To accelerate degradation the samples were exposed to ambient humidity ranging from 60 to 100 % RH or immersed in water. In previous humidity-related studies it has been inferred that electrolysis of water is important for humidity-related degradation[73,78,79]. The current-density, j, is a direct measure of the reaction-rate of a reduction-oxidation electrochemical reaction. If the reaction is controlled by the charge-transfer rather than the mass-transport at the electrode, j is then described in terms of the Volmer-Butler equation[80,81]:

$$j = j_0\left(e^{\frac{(1-\alpha_A)F\eta}{RT}} - e^{\frac{-\alpha_C F\eta}{RT}}\right)\left[\frac{A}{m^2}\right] \quad (3.14)$$

where j_0 is the equilibrium current-density at the electrode-potential required for water electrolysis. F is is the Faraday-constant, $\eta = E - E_{eq}$, the overpotential, R the universal gas-constant, α a symmetry-factor and T the temperature. When either the oxidation or reduction-reaction is dominating (at large overpotentials), the anodic and cathodic current densities can be re-written using the Tafel-notation[82]:

$$\ln|j_{anode}| = \ln|j_0| + \frac{(1-\alpha_A)F\eta}{RT} \quad (3.15)$$

$$\ln|j_{cathode}| = \ln|j_0| - \frac{\alpha_C F\eta}{RT} \quad (3.16)$$

The linear slope in a plot of $\ln|j|$ vs η is used to characterize the electrochemical activity of the used electrode. A Tafel-plot for Au/TiW/PZT, Pt/PZT and Pt/Ti/PZT immersed in water is exemplified in Figure 3.9 (c). Here $j_{0,Pt} = 0.86 \pm 0.32\ mA/mm^2$, $j_{0,Pt/Ti} = 1.03 \pm 0.43\ mA/mm^2$ and $j_{0,Au/TiW} = 0.34 \pm 0.21\ mA/mm^2$ with slopes of $\alpha_{A,Pt} = 285 \pm 16\ mV/dec$, $\alpha_{A,Pt/Ti} = 259 \pm 5\ mV/dec$ and $\alpha_{A,Au/TiW} = 376 \pm 33\ mV/dec$ indicate that the electrochemical activity is larger for the Pt-based electrodes compared to the Au-based electrodes in high humidity, consistent with previous literature-reports[83].

References

[1] H. Nazeer, M. D. Nguyen, G. Rijnders, L. Abelmann, Sardan Sukas, *Microelectron. Eng.* **2016**, *161*, 56.

[2] T. Schneller, R. Waser, M. Kosec, D. Payne, *Chemical solution deposition of functional oxide thin films*; Schneller, T.; Waser, R.; Kosec, M.; Payne, D., Eds.; Springer Vienna: Vienna, 2013; Vol. 9783211993.

[3] G. D. Shilpa, K. Sreelakshmi, M. G. Ananthaprasad, In *IOP Conference Series: Materials Science and Engineering*; IOP Publishing, 2016; Vol. 149, p. 012190.

[4] R. Eason, *Pulsed laser deposition of thin films : applications-led growth of functional materials*; Wiley-Interscience, 2007.

[5] T. Schneller, R. Waser, M. Kosec, D. Payne, *Chemical solution deposition of functional oxide thin films*; 2013; Vol. 9783211993.

[6] C.-B. Eom, S. Trolier-McKinstry, *MRS Bull.* **2012**, *37*, 1007.

[7] H. Ræder, F. Tyholdt, W. Booij, F. Calame, N. P. Østbø, R. Bredesen, K. Prume, G. Rijnders, P. Muralt, *J. Electroceramics* **2007**, *19*, 357.

[8] S. D. Senturia, *Microsystem Design*; Kluwer Academic Publishers, 2005.

[9] M. Elwenspoek, R. Wiegerink, *Mechanical Microsensors*; Springer Berlin Heidelberg, 2001.

[10] J. J. Shea, *IEEE Electr. Insul. Mag.* **2004**, *20*, 65.

[11] R. Bogue, Recent developments in MEMS sensors: A review of applications, markets and technologies. *Sens. Rev.* **2013**, *33*, 300–304.

[12] M. I. Younis, 2011; pp. 1–12.

[13] F. Laermer, S. Franssila, L. Sainiemi, K. Kolari, In *Handbook of Silicon Based MEMS Materials and Technologies: Second Edition*; William Andrew/Elsevier, 2015; pp. 444–469.

[14] T. Bakke, A. Vogl, O. Zero, F. Tyholdt, I. R. Johansen, D. Wang, *J. Micromechanics Microengineering* **2010**, *20*, 1.

[15] Making the world's most versatile gas analyzer.

[16] B. Jiang, P. Muralt, T. Maeder, *Sensors Actuators, B Chem.* **2015**, *221*, 823.

[17] P. Rafiee, G. Khatibi, M. Zehetbauer, *Microelectron. Int.* **2017**, *34*, 9.

[18] M. Gunda, P. Kumar, M. Katiyar, *Crit. Rev. Solid State Mater. Sci.* **2017**, *42*, 129.

[19] M. Shoaib, N. H. Hamid, A. F. Malik, N. B. Zain Ali, M. Tariq Jan, *J. Sensors* **2016**, *2016*, 1.

[20] R. H. T. Wilke, P. J. Moses, P. Jousse, C. Yeager, S. Trolier-McKinstry, *Sensors Actuators, A Phys.* **2012**, *173*, 152.

[21] A. Mazzalai, D. Balma, N. Chidambaram, R. Matloub, P. Muralt, *J. Microelectromechanical Syst.* **2015**, *24*, 831.

[22] D. M. Chun, M. Sato, I. Kanno, *J. Appl. Phys.* **2013**, *113*.

[23] 1.

[24] W. Zhu, B. Akkopru-Akgun, S. Trolier-McKinstry, *Appl. Phys. Lett.* **2017**, *111*.

[25] R. Q. Rudy, L. M. Sanchez, M. Tellers, R. G. Polcawich, In *2015 Transducers - 2015 18th International Conference on Solid-State Sensors, Actuators and Microsystems*; IEEE, 2015; pp. 1315–1317.

[26] G. W. Kyle, V. Malte, H. K. Neamul, K. Barbara, E. D. John, H. S. Florian, *Smart Mater. Struct.* **2017**, *26*, 63001.

[27] J. B. Quinn, G. D. Quinn, *Dent. Mater.* **2010**, *26*, 135.

[28] T. F. Analyzer, *aixACT Syst. GmbH* Version 3.0.20.0 M1.

[29] D. Humidity, T. Module, 70.

[30] Y. Tsujiura, S. Kawabe, F. Kurokawa, H. Hida, I. Kanno, In *Japanese Journal of Applied Physics*; IOP Publishing, 2015; Vol. 54, p. 10NA04.

[31] K. Coleman, J. Walker, T. Beechem, S. Trolier-McKinstry, *J. Appl. Phys.* **2019**, *126*, 034101.

[32] A. Ayrikyan, O. Prach, N. H. Khansur, S. Keller, S. Yasui, M. Itoh, O. Sakata, K. Durst, K. G. Webber, *Acta Mater.* **2018**, *148*, 432.

[33] F. H. Schader, D. Isaia, M. Weber, E. Aulbach, K. G. Webber, *J. Mater. Sci.* **2018**, *53*, 3296.

[34] E. Martin, D. Leguillon, O. Sevecek, R. Bermejo, *Eng. Fract. Mech.* **2018**, *201*, 167.
[35] Y. C. Han, E. G. Jeong, H. Kim, S. Kwon, H. G. Im, B. S. Bae, K. C. Choi, *RSC Adv.* **2016**, *6*, 40835.
[36] N. Thejo Kalyani, S. J. Dhoble, *Renew. Sustain. Energy Rev.* **2015**, *44*, 319.
[37] Y. C. Han, E. Kim, W. Kim, H. G. Im, B. S. Bae, K. C. Choi, *Org. Electron. physics, Mater. Appl.* **2013**, *14*, 1435.
[38] K. B. Lee, S. Tirumala, S. B. Desu, S. Tirumala, *Appl. Phys. Lett.* **1999**, *74*, 1484.
[39] M. Ohring, *Materials Science of Thin Films*; Academic Press, 2002.
[40] L. M. Denis, G. Esteves, J. Walker, J. L. Jones, S. Trolier-McKinstry, *Acta Mater.* **2018**, *151*, 243.
[41] N. Bassiri-Gharb, I. Fujii, E. Hong, S. Trolier-Mckinstry, D. V Taylor, D. Damjanovic, *J. Electroceramics* **2007**, *19*, 47.
[42] M. Birkholz, *Thin Film Analysis by X-Ray Scattering*; Wiley, 2006.
[43] S. (Seizo) Morita, R. (Roland) Wiesendanger, E. (Ernst) Meyer, F. J. Giessibl, *Noncontact atomic force microscopy*; Springer, 2002.
[44] P. J. Eaton, P. West, *Atomic force microscopy*; Oxford University Press, 2010.
[45] Z. Jiang, R. Zhang, F. Li, L. Jin, N. Zhang, D. Wang, C. L. Jia, *AIP Adv.* **2016**, *6*, 065122.
[46] E. A. Pecherskaya, *Meas. Tech.* **2007**, *50*, 1101.
[47] R. Meyer, R. Waser, K. Prume, T. Schmitz, S. Tiedke, *Appl. Phys. Lett.* **2005**, *86*, 1.
[48] S. Trolier-McKinstry, R. E. Newnham, In *Materials Engineering*; Cambridge University Press, 2018; pp. 516–540.
[49] P. Muralt, S. Trolier-McKinstry, *J. Electroceramics,* **2004**, *12*, 7.
[50] D. Damjanovic, *Rep. Prog. Phys* **1998**, *61*, 1267.
[51] P. Gerber, A. Roelofs, O. Lohse, C. Kügeler, S. Tiedke, U. Böttger, R. Waser, *Rev. Sci. Instrum.* **2003**, *74*, 2613.
[52] S. Sivaramakrishnan, P. Mardilovich, A. Mason, A. Roelofs, T. Schmitz-Kempen, S. Tiedke, *Appl. Phys. Lett.* **2013**, *103*, 132904.
[53] P. Hariharan, *Choice Rev. Online* **2013**, *30*, 30.
[54] J. C. Wyant, In *Holography: A Tribute to Yuri Denisyuk and Emmett Leith*; Caulfield, H. J., Ed.; SPIE, 2002; Vol. 4737, pp. 98–107.
[55] P. Hariharan, *Choice Rev. Online* **2013**, *30*, 30.
[56] F. Chiu, *Adv. Mater. Sci. Eng.* **2014**, *2014*, 578168.
[57] H. N. Al-Shareef, K. D. Gifford, S. H. Rou, P. D. Hren, O. Auciello, A. I. Kingon, *Integr. Ferroelectr.* **1993**, *3*, 321.
[58] G. W. Dietz, W. Antpöhler, M. Klee, R. Waser, *J. Appl. Phys.* **1995**, *78*, 6113.
[59] A. Okada, *J. Appl. Phys.* **1977**, *48*, 2905.
[60] P. D. Thacher, *Appl. Opt.* **1977**, *16*, 3210.
[61] J. Robertson, C. W. Chen, *Mater. Res. Soc. Symp. - Proc.* **1999**, *541*, 443.
[62] F. Chen, R. Schafranek, W. Wu, A. Klein, *J. Phys. D. Appl. Phys.* **2009**, *42*, 215302.
[63] S. K. Dey, J. J. Lee, P. Alluri, *Jpn. J. Appl. Phys.* **1995**, *34*, 3142.
[64] R. Bermejo, P. Supancic, R. Danzer, *J. Eur. Ceram. Soc.* **2012**, *32*, 251.
[65] L. M. Garten, M. Hagiwara, S. W. Ko, S. Trolier-McKinstry, *Appl. Phys. Lett.* **2017**, *111*, 122903.
[66] D. Monteiro Diniz Reis, S. Rzepka, K. Hiller, *Microelectron. Reliab.* **2018**, *88–90*, 835.
[67] T. I. Prokopowicz, A. R. Vaskas, *Tech. Rep.* **1969**, *ECOM-90705*.
[68] W. J. Minford, *IEEE Trans. Components, Hybrids, Manuf. Technol.* **1982**, *5*, 297.
[69] Brunauer Stephen, Emmett Paul H, Teller Edward, *J. Am. Chem. Soc.* **1938**, *60*, 309.
[70] D. Y. He, L. J. Qiao, A. A. Volinsky, Y. Bai, M. Wu, W. Y. Chu, *Appl. Phys. Lett.* **2011**, *98*, 98.
[71] D. Zheng, J. Swingler, P. Weaver, *Sensors Actuators A Phys.* **2010**, *158*, 106.
[72] D. Zheng, M. Luo, J. Swingler, *Sensors Actuators, A Phys.* **2016**, *241*, 197.
[73] J. Wang, C. Salm, E. Houwman, M. Nguyen, J. Schmitz, *Proc. 2016 IEEE Int. Integr. Reliab. Work. IIRW 2016* **2017**, *0*, 65.
[74] S. Stub, E. Vøllestad, T. Norby, *J. Mater. Chem. A* **2018**, *6*, 8265.
[75] S. Ø. Stub, E. Vøllestad, T. Norby, *J. Phys. Chem. C* **2017**, *121*, 12817.
[76] F. Messerschmitt, M. Jansen, J. L. M. Rupp, *Adv. Electron. Mater.* **2018**, *4*, 1800282.

[77] F. Messerschmitt, M. Kubicek, J. L. M. Rupp, *Adv. Funct. Mater.* **2015**, *25*, 5117.

[78] J. D. Baniecki, J. S. Cross, M. Tsukada, J. Watanabe, *Appl. Phys. Lett.* **2002**, *81*, 3837.

[79] W. P. Chen, Y. Wang, J. Y. Dai, S. G. Lu, X. X. Wang, P. F. Lee, H. L. W. Chan, C. L. Choy, *Appl. Phys. Lett.* **2004**, *84*, 103.

[80] C. Coutanceau, S. Baranton, T. Audichon, In *Hydrogen Electrochemical Production*; 2017; pp. 17–62.

[81] M. Carmo, D. L. Fritz, J. Mergel, D. Stolten, A comprehensive review on PEM water electrolysis. *Int. J. Hydrogen Energy* **2013**, *38*, 4901–4934.

[82] T. Shinagawa, A. T. Garcia-Esparza, K. Takanabe, *Sci. Rep.* **2015**, *5*, 1.

[83] Z. Chen, D. Cummins, B. N. Reinecke, E. Clark, M. K. Sunkara, T. F. Jaramillo, *Nano Lett.* **2011**, *11*, 4168.

Chapter 4

Author's contribution

In this thesis the degradation-mechanisms encountered in humid ambient and its effect on the reliability and lifetime of thin-film $\mathrm{Pb(Zr,Ti)O_3}$-based piezoMEMS have been studied. The results are summarized as Manuscripts in the following chapter. In Manuscript (I) the effects of temperature and humidity on PZT-based micro-mirrors was studied from a device-perspective. Manuscript (II)-(IV) addresses the mechanisms governing humidity-related degradation of thin-film piezoMEMS in detail. Thin-film encapsulation as a measure to mitigate the effect of humidity-related effects is discussed in Manuscript V. The authors contributions the manuscripts are outlined below.

Manuscript (I)

In *Performance and reliability of PZT-based piezoelectric micromirrors operated in realistic environments* temperature-humidity-bias tests were conducted on a $\mathrm{PbZr_{0.52}Ti_{0.48}O_3}$-based thin-film piezoelectric micro-mirrors. A retrofittable experimental setup dedicated for characterizing the ferroelectric properties and electromechanical response in simulated harsh operating conditions was designed and fabricated for this purpose. Device failure from humidity-related degradation preceded those driven by temperature and was manifested as electrothermal breakdown-events concentrated along the edges of the electrodes. As a result of decreased physisorption of water molecules, a device temperature higher than the operating ambient mitigated the degradation imposed by humidity. The author developed the experimental setup and conducted the experiments. The data-analysis and writing of the manuscript was done in close collaboration with the co-authors.

R. P. Dahl-Hansen, T. Tybell and F. Tyholdt
Published in 2018 IEEE ISAF-FMAAMF-AMEC-PFM Conference Proceedings

Manuscript (II)

In *Electrochemically Driven Degradation of Ferroelectric Thin-Films in Humid Ambient* the connection between the electrode's activity towards water-electrolysis and humidity-related degradation of PZT-based structures was investigated. By evaluating Pt -and Au-based top electrode-material on undoped $\mathrm{PbZr_{0.52}Ti_{0.48}O_3}$-films, based on their electrochemical activity, it was shown that degradation in humid conditions is driven by water-electrolysis. As a result of hydrogen and oxygen gas evolving at the anode and cathode and compressing at the electrode-PZT interfaces, cracking, electrode delamination, leakage-transients and electrothermal breakdown-events dominate degradation. This occurs when the exerted pressure from the evolved gas on the thin-film exceeds the critical stress of PZT and differs from a Schottky-based degradation model, which dominates in dry conditions. Due to a lower electrochemical activity, the median time-to-failure was significantly higher for the Au-based electrodes compared to Pt-based electrodes. The author retrofitted the experimental setup from manuscript (I) to characterization-equipment available in the STM-group at Penn State University and

conducted the experiments. Brainstorming, design and fabrication of test-structures, data analysis, and writing of the manuscript were done in close collaboration with all co-authors.

R. P. Dahl-Hansen, B. Akkopru-Akgun, J. Polfus, E. Vøllestad, L. Denis, K. Coleman, F. Tyholdt, S. Trolier-McKinstry, and T. Tybell
Submitted

Manuscript (III)

In *Links between humidity-induced resistance-degradation and recovery of PZT-based piezoMEMS* the combined effect of ambient humidity, electrode-size, and surface currents on resistance-degradation of PZT thin-films were studied. The transport of protons between the anode and cathode in surface water was found to be important for humidity-related degradation of PZT. In ambient exceeding 50 % relative humidity, the surface-currents dominate over the leakage through PZT. The median time to failure decreased with increasing electrode-area, consistent with an increase in electrochemically active surface-area and proton formation rate. When flushed with dry $N_2(g)$, the degrading effects disappeared with the removal of surface-water. However, since degradation is partially irreversible, the pristine state was not completely recovered by flushing, and due to expulsion of evaporated water, in some cases worsened by post-degradation annealing. The author retrofitted the experimental setup from manuscript (I) to characterization-equipment available in the STM-group at Penn State University and at SINTEF MiNaLab. The author conducted the experiments, designed and fabricated test-structures, analyzed the data, and wrote the manuscript in close collaboration with all co-authors.

R. P. Dahl-Hansen, E. Vøllestad, F. Tyholdt, S. Trolier-McKinstry, and T. Tybell
To be submitted

Manuscript (IV)

In *On the effects of water-induced degradation on thin-film piezoelectric microelectromechanical systems* the dynamical behavior and encapsulation of thin-film piezoelectric micro-mirrors operated in humid conditions are investigated. Thin-film encapsulation using 40 nm Al_2O_3 deposited by atomic layer deposition improved device-lifetime by two orders of magnitude of time relative to the bare devices, however at the cost of considerably decreased piezoelectric and ferroelectric compliances. Significant distortions in the device's dynamic behavior was measured as degradation proceeded. The electrode routings were identified as the critical flaw. The author developed the experimental setup, conducted the experiments, analyzed the data and wrote the manuscript in close collaboration with the co-authors.

R. P. Dahl-Hansen, F. Tyholdt, J. Gjessing, A. VogI, J. Vedum, P. Wittendorp and T. Tybell
To be submitted

The author has also presented the research on the following national and international conferences:

- PIEZO2017, Electroceramics for End Users IX, Madrid, 2017
- NanoNetwork, Norway, 2017
- IEEE ISAF-FMA-AMF-AMEC-PFM Joint Conference, IFAAP 2018
- NanoNetwork, Norway, 2018
- NanoNetwork, Norway, 2019
- IEEE International Symposium on Applications of Ferroelectrics (ISAF), 2019

Manuscript (I)

Performance and reliability of PZT-based piezoelectric micromirrors operated in realistic environments

R. P. Dahl-Hansen, F. Tyholdt and T. Tybell

Published in 2018 IEEE ISAF-FMA-AMF-AMEC-PFM Joint Conference Proceedings

Performance and reliability of PZT-based piezoelectric micromirrors operated in realistic environments

R. P. Dahl-Hansen[1,2*], T. Tybell[1]
[1]Norwegian University of Science and Technology
Department of Electronic Systems,
7491, Trondheim, Norway

F. Tyholdt[2]
[2]SINTEF Digital, MiNaLab,
Gaustadalleen 23C, 0373, Oslo, Norway
*runarplu@ntnu.no

***Abstract*—The number of application areas for piezoelectric microelectromechanical systems based on PZT have increased rapidly over the years. Thus, to continue the development towards commercial deployment, characterizing lifetime and reliability during operation in realistic and harsh environments is important. Such environments are demanding for piezoMEMS devices since they often involve high humidity levels and elevated temperatures which gives rise to complex degradation. To address how such conditions affects device performance we combined optical and electrical measurements to elucidate the degradation of a PZT-based thin-film piezoelectric MEMS micromirror during temperature-humidity-cycling tests. As a test structure, 1 μm $PbZr_{0.40}Ti_{0.60}O_3$ on a 10 nm $LaNiO_3$ buffer-layer, were deposited by pulsed laser deposition on platinized Silicon-on-Insulator wafers. A 250 nm Au/TiW top electrode was deposited by DC-sputtering before structuring the final device. The micromirrors were unipolarly actuated with 20 V peak-to-peak at a frequency of 1.5 kHz in absolute humidity of 22 g/m^3 for device temperatures between 25 ^oC and 175 ^oC. Humidity-related degradation was manifested as local breakdown events and pinholes on top of and along the edges of the used electrodes. This had a strong effect on device performance and preceded failure due to polarization-fatigue at all temperatures. Both the initial piezoelectric response and number of cycles to device failure increased with increasing substrate temperature in humid ambient.**

Keywords: PiezoMEMS reliability, lifetime, fatigue, temperature, humidity

I. Introduction

Due to its large piezoelectric response, $PbZr_xTi_{1-x}O_3$ (PZT) is commonly used for piezoelectric microelectromechanical systems (piezoMEMS). This includes RF-switches, ultrasonic transducers, gas sensors and micromirrors [1], [2]. Prior to commercialization, temperature-humidity-bias testing is important to assess the reliability of piezoMEMS-devices operated in realistic and harsh environments. Device operation in high humidity is associated with the early onset of irreversible degradation, including electromigration, cracking and local breakdown events [3]. Degradation is primarily observed in close vicinity to the used electrodes and originates from electrical, mechanical and electrochemical processes occurring both within PZT and on the PZT and electrode surfaces during operation. Elevated temperatures affect both reversible and irreversible degradation mechanisms due to ionic migration within the film. This changes the dielectric and piezoelectric properties and thereby the stress-strain relations of the structure [4]–[6]. Since thin-film piezoMEMS-devices rely heavily on the stress-transfer between the film and substrate, in-plane changes caused by any such degradation may have major implications on the electromechanical response and device performance. Hence it is important to assess how the piezoelectric response, lifetime and reliability of each piezoMEMS-device is affected by elevated temperature and ambient humidity.

In the current work we investigated the degradation and electromechanical response of bimorph PZT-based thin film

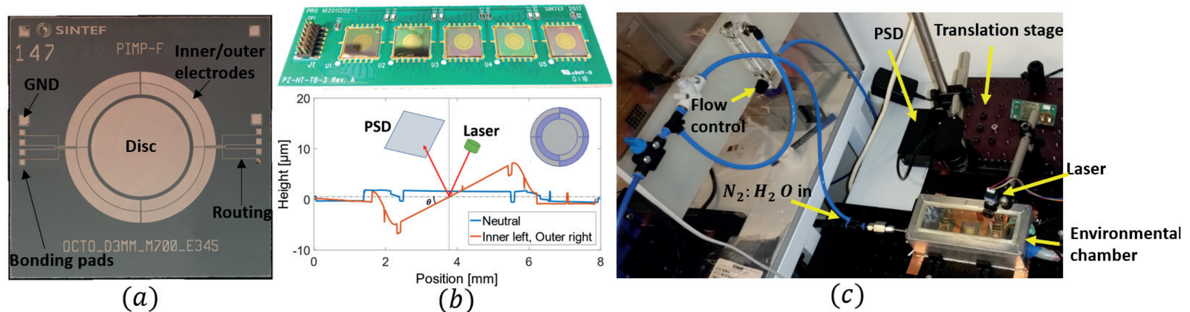

Figure 1: Device and experimental setup. (a): structure of the tested micromirror, (b): MEMS test-circuit for simultaneous testing of five micromirrors and actuation giving the maximum 2D tilt of $\pm 0.5^o$ The laser was reflected of the mirror onto a position sensitive device (PSD). (c): environmental chamber and experimental setup. The ambient was kept constant with an absolute humidity of 22 g/m^2 and the micromirrors were heated from below by a hot plate.

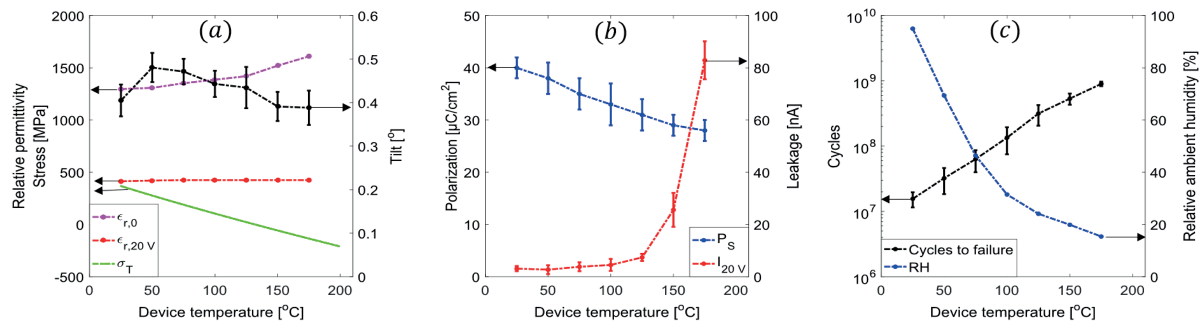

Figure 2: (a): Measured relative permittivity at 0 V, $\varepsilon_{r,0}$, and 20 V, $\varepsilon_{r,20\,V}$, calculated thermal stress, σ_T, and deflection tilt as a function of device temperature. (b): average polarization and leakage as a function of device temperature. (c): Average cycles to failure, and relative humidity due to heated ambient as a function of device temperature.

micromirrors during operation in humid ambient and elevated temperatures.

II. Methods

Piezoelectric micromirrors, see *Fig. 1* (a), were fabricated according to literature [1] using 1 µm pulsed laser-deposited Ba-doped $PbZr_{0.40}Ti_{0.60}O_3$. The mirror consisted of a rigid Silicon disc $3\,mm$ in diameter, suspended on a flexible membrane surrounded by eight integrated PZT-actuators. Out-of-plane and tip-tilt momotion was enabled by actuating the inner and outer electrodes according to *Fig. 1* (b). For the micromirrors used in this work, a maximum angular deflection of $\pm 0.5^o$ was achieved by simultaneously actuating the two inner and two outer electrodes on opposite sides of the center disc. Five micromirrors were wire-bonded to a test-circuit and actuated in parallel inside the environmental chamber for each test condition. The ambient vapor concentration was kept constant at $22\,g/m^3$ by bubbling N_2 through a DI-water container and introducing the mixture into the chamber as shown in *Fig. 1* (c). Humidity and ambient temperature (T_{atm}) was measured using a HYT271 humidity-sensor and the micromirrors heated from below by a hotplate. The micromirror temperature (T_{sub}) was measured using a k-type thermocouple attached to the surface of one of the tested devices.

After ambient stabilization, the micromirrors were unipolarly actuated with a peak-to-peak voltage (V_{PP}) of $20\,V$ at $1.5\,kHz$ while T_{sub} was varied in steps of $25\,^oC$ from $25\,^oC$ to $175\,^oC$. A laser was reflected of the micromirror through an optical window onto a position sensitive device (PSD) for electromechanical characterization. The recorded x -and y-positions of the laser trace were then used to approximate the deflection tilt according to:

$$tan(2\theta) \approx 2\theta = \frac{\sqrt{x^2 + y^2}}{l}\;[rad] \qquad (1)$$

where θ is the achieved angular deflection of the micromirror according to the neutral plane, see *Fig. 1* (b), and l the length from the device to the PSD. Ferroelectric characterization was done by retrofitting an aixACCT TF2000 Analyzer to the experimental setup. Ferroelectric hysteresis was measured at $10\,Hz$ with a large-signal of $-25\,V$ to $25\,V$, the capacitance-measurements with a small-signal amplitude of $200\,mV$ at $1\,kHz$ and the leakage with steps of $2\,V$ and $2\,sec$ dwell from $-20\;to\;20\,V$.

III. Results and discussion

A. Electromechanical response

Fig. 2 (a) show the measured average angular tilt, relative permittivity at 0 V ($\varepsilon_{r,0\,V}$) and 20 V ($\varepsilon_{r,20\,V}$) and calculated total thermal stress in the device stack (σ_T) plotted as a function of T_{sub}. The measured average saturation polarization (P_S) and leakage at $20\,V$ ($I_{20,V}$) are shown in *Fig. 2* (b) and the values summarized in *TABLE I*. $\varepsilon_{r,0}$, $\varepsilon_{r,20\,V}$ and $I_{20\,V}$ increases, while P_S decreases with increasing T_{sub} and is consistent with literature on ferroelectrics [5]. As shown in *Fig. 2* (a) the measured average tilt increases with T_{sub} and peaks at 50^oC before it decreases for $T_{sub} > 50\,^oC$. Similar electromechanical behavior has been reported for similar PZT-based ceramics in literature [7]. Thin-film devices such as the present micromirror, are particularly sensitive to the in-plane circumstances. Hence in-plane stress, excitation field and device geometry are important for the final electromechanical response. The bending moment moving the current device structure originates from the total in-

Table I: Average measured values

$Device$	$T_{sub}\,[^oC]$	$T_{atm}\,[^oC]$	$Tilt\,[deg]$	$Cycles\;to\;failure$	$\varepsilon_{r,0}$	$\varepsilon_{r,20}$	$P_R\,[\frac{\mu C}{cm^2}]$	$P_S\,[\frac{\mu C}{cm^2}]$	$I^+\,[nA]$	$\sigma_T\,[MPa]$	RH [%]
$1-5$	25	25.0	0.40 ± 0.04	$1.6x10^7 \pm 0.4x10^7$	1297	414	10.3	40 ± 2	3.1 ± 1.0	*368*	95.0
$6-10$	50	30.8	0.48 ± 0.03	$3.2x10^7 \pm 1.4x10^7$	1308	420	10.3	38 ± 3	2.7 ± 1.7	*284*	69.4
$11-15$	75	38.5	0.47 ± 0.03	$6.3x10^7 \pm 2.3x10^7$	1353	424	9.3	35 ± 3	3.8 ± 1.7	*196*	46.4
$16-20$	100	46.4	0.44 ± 0.03	$13.5x10^7 \pm 6.0x10^7$	1387	425	8.3	33 ± 4	4.5 ± 2.3	*111*	31.5
$21-25$	125	52.1	0.43 ± 0.04	$31.6x10^7 \pm 10.9x10^7$	1420	425	7.9	31 ± 3	7.4 ± 1.4	*29*	24.1
$26-30$	150	56.4	0.40 ± 0.03	$53.5x10^7 \pm 10.4x10^7$	1521	425	8.0	29 ± 2	25.6 ± 6.5	*-51*	19.9
$31-35$	175	62.3	0.39 ± 0.04	$90.0x10^7 \pm 7.2x10^7$	1610	425	8.0	28 ± 2	82.9 ± 7.3	*-129*	15.4

TABLE II: VALUES FOR THERMAL STRESS CALCULATION

Material	$E\,[GPa]$	ν	$\alpha x10^{-6}\,[K^{-1}]$	$T_{dep}\,[^oC]$	*Ref.*
Au	*78*	*0.44*	*14.2*	*25*	*[5]*
PZT	*161*	*0.31*	*6*	*620*	*[5]*
Pt	*168*	*0.38*	*9*	*450*	*[5]*
SiO_2	*70*	*0.3*	*0.6*	1050	*[5]*
Si	*170*	*0.28*	$-15.2459 + 3.43026lnT$	*N/A*	*[8]*

plane stress (σ_{tot}) and has three main contributions: the residual stress (σ_R) applied stress (σ_A) and piezoelectric stress (σ_P). The latter being the controllable stress, relates to the transverse electric field, E_z, and the effective in-plane piezocoefficient, $e_{31,f}$ by $\sigma_P = -e_{31,f}E_z$. $e_{31,f}$ is proportional to P_S and ε_r measured out-of-plane (along the 3-direction), i.e. $e_{31,f} \propto -2\varepsilon_{33}P_3$ [5]. Since the relative decrease in P_S appears larger than the relative increase in $\varepsilon_{r,0}$ and $\varepsilon_{r,20}$, the net σ_P (and total deflection) decreases with increasing temperature. From the measured values of P_S and ε_r, this should correspond to a net decrease of the total in-plane stress by 4.2 % at 50^oC. On the contrary, the measured initial deflection is indeed increasing by 20 % from 25 ^oC to 50 ^oC, and remains larger than the room-temperature deflection up to $T_{sub} = 175\,^oC$. In addition to increased domain wall mobility, it is suggested that this is partly due to stress changes in the stack where $\sigma_{tot} = \sigma_R + \sigma_A + \sigma_P$. A large portion of the residual stress is the thermal stress between the film and substrate given by:

$$\sigma_T = \frac{E_{film}\,(\alpha_{film} - \alpha_{sub})\Delta T}{(1 - \nu_{film})}\;[MPa] \qquad (2)$$

where α is the thermal expansion coefficients of the used materials, E_{film} is the Young's modulus, ν_{film} is the Poisson ratio and ΔT is the difference between the deposition and T_{sub}. Here a positive sign corresponds to a tensile stress and a negative sign to a compressive stress. As a simple first order approximation, σ_T was calculated for the adjacent films and added together for the entire stack[1]. The linear thermal expansion coefficient was used for all materials except Si which displays the largest nonlinearities in the relevant temperature range [8]. *TABLE II* summarizes the used thermal expansion values and the calculated σ_T at the different T_{sub} can be found in *Fig. 2* (a) and *TABLE I*. Despite the simplicity of the used model the calculated stresses correlate well with measured values from previous wafer bending experiments.

PLD-deposited PZT typically holds a substantial amount of residual stresses post processing which may reduce devices piezoelectric response. As T_{sub} increases, the thermal contribution to this stress| is gradually relaxed, which will move the operation point away from the saturation point in the piezoelectric hysteresis. Due to increased linearity, any such stress-relaxation is expected to increase the piezoelectric response which is indeed observed here. Also, the highly nonlinear α of Silicon will in the current temperature range cause the largest thermal stress-relaxation of the stack to occur between 25^oC and 100^oC and may therefore be an additional contribution. Also, other mechanisms such as increased domain wall mobility with temperature will have a positive effect on the unipolar strain [6] and the net result of the competing mechanisms is an increased piezoelectric response.

B. *Humidity-related degradation*

Micrographs of the bonding pads after device failure is shown in *Fig. 3* (a). Humidity-related degradation was primarily manifested as local breakdown-events and pinhole-formation along the edges and on top of all utilized top electrodes. The ground pads and unused electrodes, however, remained unaffected. As shown in *Fig. 3* (a), the relative pinhole concentration appeared to be considerably larger along the electrode edges than on top of the electrode surfaces. Also, the total number and relative portion of pinholes along the edges compared to the electrode surface was significantly larger at lower T_{sub} than at higher T_{sub}. Since for the present experiments the applied voltage was above the standard potential for catalytic water-splitting of $1.23\,V$, we speculate that water-splitting catalysis can facilitate the observed degradation. During testing, the Ti/W-layer used as an adhesion-layer between Au and PZT is exposed to the ambient along the electrode edges and can hence form catalytically active oxides such as TiO_2 and WO_3 in the presence of humidity. If water-splitting is indeed occurring, hydrogen will evolve on the top electrode and may quickly diffuse into PZT along the electrode edges. If e.g. hydrogen-induced hardening reduces the critical stress - the maximum stress the PZT-films can accommodate before cracking - so that the application of σ_P results in cracks, the edges should be the first area to be affected by such degradation. The fact that the unused and bottom electrodes remains unaffected may indeed further support this claim and similar observations have been reported for PZT under DC-bias [9], [10] and in the FERAM-literature [11].

For water splitting to occur on the electrode surface, PZT should either be exposed through the top electrode or catalysis should occur on Au. The former can be true in the presence of pinholes, large local defects such as sputtered particles or cracks appearing during operation. The latter have recently caught interest in literature due to the catalytic activity of gold [12]. To understand the connection of the observed degradation to

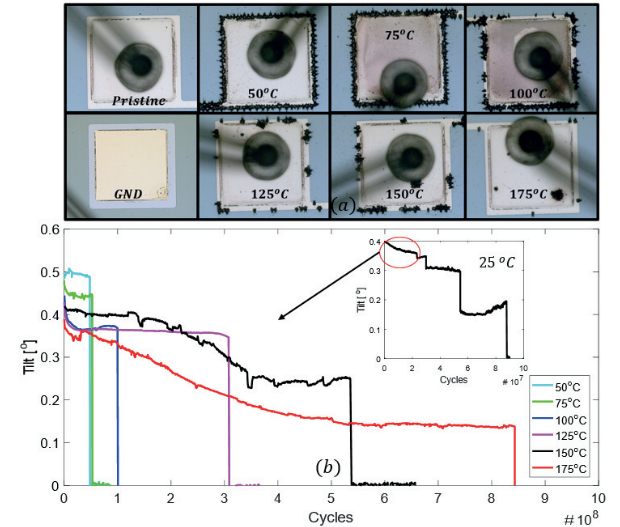

Figure 3: (a): micrographs of bonding pads after failure at $25 - 175^oC$ in humid ambient and (b): measured deflection as a function of cycles.

[1] The thickness and device geometry must also be considered for exact stress-calculations of multi-layered stacks.

elevated temperatures, the adsorption of water on the device surface must be discussed. In humid ambient, the surface of perovskite oxides, including PZT, will quickly saturate with a thermally stable layer of chemisorbed hydroxide species and PZT is therefore by itself not severely affected by humidity in the absence of applied voltages, e.g. far away from the used electrodes [13]. Gold on the other hand, is chemically inert and will facilitate molecular adsorption of water [14]. The number of adsorbed molecules depend on the heat of adsorption and desorption of water at a given relative humidity (RH) and T_{atm}. For $RH < 60\%$ the water adsorbed on gold can be approximated by the Brunauer–Emmett–Teller (BET) theory:

$$M_W = \frac{cRH}{(1-RH)(1+RH(c-1))}\ [\frac{\mu\boldsymbol{g}}{\boldsymbol{cm^2}}] \qquad (3)$$

Here M_W is the number of adsorbed monolayers, $c = e^{\frac{Q_i - Q_v}{RT_i}}$ a material-related constant, Q_i and Q_v the heat of water adsorption and desorption, R the universal gas constant and T_i the temperature at the interface between the electrode and the ambient. For gold surfaces up to $T_i = 60\ ^oC$, the net heat of adsorption is small, i.e. $Q_i \approx Q_v$. In this temperature range M_W primarily depends on the relative humidity; $M_W \approx \frac{RH}{1-RH}$ [14]. Since increasing T_{atm} reduces the ambient RH, as shown in $Fig. 2\ (c)$, the number of adsorbed monolayers will decrease. Additionally, heating the device from below increases T_i compared to T_{atm}, and decreases M_W. Here, as T_{sub} approaches $175\ ^oC$, T_{atm} will approach $62\ ^oC$. Since c decreases exponentially with T_i, M_W causing the humidity-induced degradation rate, to decrease as seen here. Heating the ambient and cooling the device-temperature, will therefore, due to surface-adsorption, increase the degradation rate. Below $60\ ^oC$, as RH increases, the adsorbed water will, due to horizontal interactions form, a continuous film on the surface as RH exceeds about 60 % RH, which will further increase degradation. It can also be mentioned that the amount of adsorbed water molecules will be lower if the surface is clean [14].

The above discussion correlate well with the increasing cycles to failure with increasing T_{sub} (see *Fig. 2* (c) and *TABLE I*). Yet, since at elevated temperatures, devices still degrade at low RH, additional factors such as the absolute humidity rather than the relative humidity, the relation between the device temperature and the ambient temperature as well as the cleanliness of the device being tested, should be taken into account in humidity-based lifetime and reliability testing. It is noted, in this regard, that no local breakdown-events was observed for devices operated in $RH = 35\ \%$ at $T_{sub} = 25\ ^oC$, and $T_{atm} = 25\ ^oC$ for up to $1.5x10^{11}$ cycles. At $T_{sub} = 175\ ^oC, T_{atm} = 62.3\ ^oC$ and $RH = 15.4\ \%$ on the other hand, failure occurred after $9x10^8$ cycles.

The measured amplitude degradation in high humidity was typically characterized by four sudden drops during operation, as shown in the inset of *Fig. 3* (b). Each drop was associated with the breach of an electrode routing connecting the wire-bonding pads to the actuating membrane. Hence, device failure was defined as the breach of the first electrode. The tilt relative to the tilt at $25\ ^oC$ as a function cycles until the first routing breach is plotted vs T_{sub} in the main graph of *Fig. 3* (b). As seen, the deflection amplitude declines by cycling for all devices. But, even though the rate of decline was significantly higher at elevated temperatures, as to be expected [5], the lifetime was indeed longer. However, the electromechanical degradation by cycling was found to exceed the expected contribution from pure ferroelectric fatigue. E.g. at $175\ ^oC$ the average decrease in tilt was $65\ \%$ opposed to a $10\ \%$ decrease in P_S after $5x10^8$ cycles (not shown here). ε_r remained approximately constant throughout the experiments. Again, this points towards the in-plane sensitivity to film-substrate stress transfer and other factors of such devices. Lastly it can be mentioned that no short-circuiting was detected prior to the shown routing breaches.

IV. Summary and Conclusions

Unipolar temperature-humidity-cycling tests with a constant absolute humidity of $22\ g/m^3$ and substrate temperatures from 25^oC to $175\ ^oC$ were carried out to assess the lifetime and reliability of PZT-based piezoelectric micromirrors. For all temperatures, humidity related degradation by local breakdown-events was more pronounced and preceded that related to polarization fatigue. Also, the average initial piezoelectric response and number of cycles to device failure were both found to increase with increasing substrate temperatures.

Acknowledgments

The authors wish to thank A. Vogl, P. Wittendorp and J. Gjessing for their excellent scientific and technical support. The present research was kindly supported by the Research Council of Norway under contract number 247781/O30.

References

[1] C.-B. Eom and S. Trolier-McKinstry, “Thin-film piezoelectric MEMS,” *MRS Bull.*, vol. 37, no. 11, pp. 1007–1017, 2012.

[2] T. Bakke et al., “A novel ultra-planar, long-stroke and low-voltage piezoelectric micromirror,” *J. Micromechanics Microengineering*, vol. 20, p. 064010, 2010.

[3] I. P. Lipscomb et al., “The effect of relative humidity, temperature and electrical field on leakage currents in piezo-ceramic actuators under dc bias,” *Sensors Actuators, A Phys.*, vol. 151, no. 2, pp. 179–186, 2009.

[4] H. Nazeer et al., “Residual stress and Young’s modulus of pulsed laser deposited PZT thin films: Effect of thin film composition and crystal direction of Si cantilevers,” *Microelectron. Eng.*, vol. 161, pp. 56–62, 2016.

[5] D. Damjanovic, “Ferroelectric, dielectric and piezoelectric properties of ferroelectric thin films and ceramics,” *Reports Prog. Phys.*, vol. 61, no. 9, pp. 1267–1324, 1998.

[6] Y. A. Genenko et al., “Mechanisms of aging and fatigue in ferroelectrics,” *Mater. Sci. Eng. B Solid-State Mater. Adv. Technol.*, vol. 192, no. C, pp. 52–82, 2015.

[7] M. W. Hooker, “Properties of PZT-Based Piezoelectric Ceramics Between -150 and 250 C,” *Lockheed Martin Eng. Sci. Co.*, no. September, p. 28, 1998.

[8] V. M. Glazov and A. S. Pashinkin, “The Thermophysical Properties (Heat Capacity and Thermal Expansion) of Single-Crystal Silicon,” *High Temp.*, vol. 39, no. 3, pp. 413–419, 2001.

[9] D. Zheng et al., “Multi-breakdown model for explaining the formation and growth of black spots in PZT capacitor under DC bias,” *Sensors Actuators, A Phys.*, vol. 241, pp. 197–202, 2016.

[10] D. Zheng et al., “Current leakage and transients in ferroelectric ceramics under high humidity conditions,” vol. 158, pp. 106–111, 2010.

[11] C. Huang et al., “Effect of hydrogen on Pb(Zr,Ti)O3-based ferroelectric capacitors,” *J Appl Phys*, vol. 98, no. 98, p. 104105, 2005.

[12] G. M. Mullen et al., “The effects of adsorbed water on gold catalysis and surface chemistry,” *Top. Catal.*, vol. 56, no. 15–17, pp. 1499–1511, 2013.

[13] J. M. Polfus et al., “Surface defect chemistry of Y-substituted and hydrated BaZrO 3 with subsurface space-charge regions,” *J. Mater. Chem. A*, vol. 4, no. 19, pp. 7437–7444, 2016.

[14] S. Sharma and J. Thomas III, “Adsorption of water vapor on thin gold electroplated on copper,” *J. Vac. Sci. Technol.*, vol. 825, pp. 3–5, 1977.

Manuscript (II)

Electrochemically Driven Degradation of Ferroelectric Thin-Films in Humid Ambient

R. P. Dahl-Hansen, J. M. Polfus, E. Vøllestad, B. Akkopru-Akgun, L. Denis, K. Coleman, F. Tyholdt, S. Trolier-McKinstry and T. Tybell

Submitted

This paper is awaiting publication and is not included

Manuscript (III)

Links between resistance-degradation and recovery of PZT operated in humid conditions

R. P. Dahl-Hansen, E. Vøllestad, F. Tyholdt, S. Trolier-McKinstry and T. Tybell

To be submitted

This paper is awaiting publication and is not included

Manuscript (IV)

On the effects of water-induced degradation on thin-film piezoelectric microelectromechanical systems

R. P. Dahl-Hansen, F. Tyholdt, J. Gjessing, A. Vogl, J. Vedum. P. Wittendorp, and T. Tybell

To be submitted

This paper is awaiting publication and is not included

Chapter 5

Conclusions and outlook

Though the reliability has improved considerably over the years, reliability and lifetime in realistic environments remains as the key challenges for the widespread adaption of thin-film piezoMEMS. Degradation in humid conditions is particularly severe, and understanding the underlying mechanisms is imperative for developing mitigation-strategies and improve reliability. The presented manuscripts forming the major part of this thesis addresses humidity-related issues from an applied perspective. By developing and understanding the underlying mechanisms, the work in this thesis contributes to the continued improvement of piezoMEMS reliability, operated in humid conditions. This chapter highlights the results of this thesis and provides concluding remarks and an outlook for further studies.

5.1 Conclusions

Humidity-related degradation mechanisms and their effect on thin-film PZT-based micro-mirrors and test-structures were studied. The main findings are as follows:

- When operated in high humidity, degradation manifests itself as leakage transients, Joule-heating, and local evaporation of the stack-material on top of the surface and along the electrode edges. This affects the dynamic behavior of PZT-based micro-mirrors and precedes degradation from other related degradation mechanisms. Decreasing the relative humidity at the surface, for example, by increasing the surface temperature, reduces the degradation-rate, yet accelerated degradation proceeds at elevated temperatures down to 15 % relative humidity. At room temperature in 35 % RH on the other hand, no apparent degradation was detected after $> 10^6$ s, suggesting that the absolute, rather than the relative humidity, accounts for the observed degradation.
- Degradation in humid conditions couples to the electrode's electrochemical activity for water electrolysis. Protonic charge-carriers transported between the anode and cathode via bulk and in surface water forms an electrochemical cell and drives degradation. When the onset potential for electrolysis of water is exceeded, the generation of oxygen gas at the anode and hydrogen gas at the cathode exerts and increasing pressure on the film and electrode interfaces. When the internal pressure exceeds the critical stress of the stack components, the evolved gas leads to electrode delamination, cracking, and eventually leakage-transients and electrothermal breakdown-events. Time-dependent dielectric breakdown evolves over three-stages; (i) Initial leakage transients, (ii) macro-cracking and minor electrothermal leakage transients and (iii) short circuit, cascadic electrothermal breakdown and dielectric breakdown.
- Humidity-induced degradation is sensitive to the surface-water following the Brunauer-Emmet-Teller theory. Above 60 % relative humidity, surface-water increases the proton-conductivity and dominates leakage. Degradation is further accelerated upon cracking since additional conduction pathways from anode to cathode is opened. High-conductive states of water in microchannels and along surfaces are expected to contribute to degradation.

- Degradation in humidity occurs as an aggregated result of proton-incorporation, surface-currents, and electrochemical currents. Since the major current-contribution stems from surface currents, leakage decreases upon annealing or flushing with dry $N_2(g)$ as the surface water is removed. An additional post-annealing step can be used for sample-recovery, though further degradation in the form of cracking and delamination is expected as a result of water being expulsed from the sample during heating. While flushing and annealing remove physisorbed water-molecules and the electrochemical contribution to leakage, incorporated protons, chemisorbed species, and irreversible degradation remain. Complete sample-recovery can, therefore, not be achieved.
- Encapsulation and piezoMEMS-reliability are an undividable couple, but challenging due to the thin-film structure's sensitivity to the in-plane stress-transfer between the film and substrate. As such, while using a humidity-barrier of atomic-layer-deposited Al_2O_3 improves device lifetime, the additional processing step may decrease the ferroelectric and piezoelectric properties of the piezoMEMS-device. Breeches in the barrier-layer can arise from various defects in the coating or PZT film, and humidity-degradation can spread from the defective site.
- Since the operation of piezoelectric micro-mirrors rely heavily on the film-substrate stress-transfer, the electrothermal breakdown-events changes the dynamic behavior. Such distortions are here manifested through nonlinear phenomena and displaced tip-tilt motions.

This work has shed light on possible next steps for improving piezoMEMS devices operated in humid conditions. From the above findings, some mitigation-strategies for reducing the impact of humidity, are proposed:

(i) Decreasing the overall electrochemical activity of the stack will reduce the amount of water-electrolysis, and thereby the degradation-rate.

(ii) Since, within the framework of water-electrolysis, protons generated on the anode-side move towards the cathode-side of the stack, the bottom electrode should be chosen as the positrode. This, to reduce the area of the electrochemically active materials being exposed to the ambient during operation, thereby reducing the proton-transport through the piezoelectric layer.

(iii) The electrochemical activity can be reduced by impeding the proton mobility in PZT and along exposed surfaces, e.g. by reducing the physisorption of water-molecules on the exposed surfaces.

(iv) Reducing the number of electrode-defects, such as grain-grooves, sputtered particles, cracks or pinholes will reduce the diffusion of protons and hydrogen through the electrode. This can be done by e.g. increasing the electrode thickness when possible.

(v) Since the electrolysis of water is essentially a DC-phenomena involving the transport of protons in the form of hydronium or hydroxide-ions, the electrochemical activity will further be reduced by using high-frequency (>100 Hz) bipolar actuation, when such operation is relevant (e.g. for FRAM-applications).

(vi) It is imperative to encapsulate piezoMEMS-devices. Therefore, improved electromechanical durability, improved coverage over complex structured surfaces, and reduced water-vapor transmission rate of the humidity barrier-layer will reduce the impact of water. Multi-layered coatings deposited by atomic layer deposition show promising results in this regard.

5.2 Outlook and future work

As a last note, ideas and suggestions for future work are presented here.

Little is known about the formation and transport of protonic defects in PZT related ferroelectric and piezoelectric materials, such as KNN, PMN-PT or AlN. The correlation between protonic defect formation, charge-transport mechanisms, the effect of doping, and piezoelectric and dielectric properties should, therefore, be studied in detail. For the case of PZT, oxygen vacancies contribute to the formation and transport of protonic charge-carriers, and much insight can be gained from conductivity-measurements as a function of water-vapour and oxygen partial pressures. Impedance, and thermally stimulated depolarization-current-measurements of pristine and degraded samples may also prove useful for studying the governing charge-transport mechanisms.

The control of interfaces, surface termination, and reconstructions in heterostructured thin-films are potential tools for studying the electrochemical factors. From density functional theory calculations, a fundamental understanding of the interactions between polar surfaces and humidity, adsorption-geometries, energetics, and activation energies can be attained. This can be used to evaluate and control the electrochemical interactions and possible migration paths of protonic species within the bulk, surface, and grain-boundary regions of the film.

From an applied perspective, the continued development of humidity-barriers and its integration in piezoMEMS should be pursued. Properties such as the mechanical robustness, self-healing effects, water-vapor penetration, and adsorption/transport of water-molecules on surfaces, should be further investigated. Developing thin, multi-layered barriers is a promising approach.

Devices such as PZT-based energy harvesters rely on the maximum piezoelectric strain and endurance during stress-cycling under repetitive mechanical loadings. Since humidity-related degradation couples to the mechanical properties of the stack, studying the evolution of the mechanical properties of piezoelectric thin-films during degradation in humid conditions may prove useful. Relating the electro-mechanical mechanisms such as electromechanical fatigue, criteria for crack-initiation and propagation, domain-wall mobility and microstructure to various humidity-induced effects, e.g. gas-evolution or chemical expansion from incorporated protonic defects, may provide valuable insight. Raman spectroscopy, Rayleigh analysis or wafer-bending are all valuable tools for providing connections between humidity and the mechanical limitations of ferroelectrics.

Considering that lead-free piezoelectric materials are increasing their momentum, the studies suggested above should also be adapted at an early stage on promising material-candidates, such as $(K, Na)NbO_3$, $(Ba, Ca)(Ti, Zr)O_3$ or $AlScN$-based compounds.

Studying the evolution of the dynamic behavior of piezoMEMS-devices upon degradation can provide valuable diagnostic and characterization-tools from an applied perspective. Using the spring-mass system as a basis, and combining it with machine-learning can provide a powerful arena for sensitivity-analyses, and studying the connection between nonlinear-dynamics and degradation.

Thin-film piezoMEMS is a technology with much unexplored potential. PZT and related compositions, are essential for existing and for future key enabling technologies, which can be utilized by improving reliability -and lifetime in realistic conditions, and should inspire to continued research within piezoMEMS reliability and lifetime.